ADVANCED ELECTROMAGNETIC SYSTEM ANALYSIS FOR MICROWAVE INVERSE AND DESIGN PROBLEMS

ADVANCED ELECTROMAGNETIC SYSTEM ANALYSIS FOR MICROWAVE INVERSE AND DESIGN PROBLEMS

By
YUNPENG SONG, M.SC.

A Thesis
Submitted to the School of Graduate Studies
in Partial Fulfillment of the Requirements
for the Degree
Doctor of Philosophy

McMaster University

DOCTOR OF PHILOSOPHY (2010) McMASTER UNIVERSITY
(Electrical and Computer Engineering) Hamilton, Ontario

TITLE: **Advanced Electromagnetic System Analysis for Microwave Inverse and Design Problems**

AUTHOR: Yunpeng Song
M. Sc.
Department of Electrical and Computer Engineering
(Concordia University)

SUPERVISOR: N. K. Nikolova, Professor
Ph. D. (University of Electro-Communications)
P. Eng. (Ontario)
Canada Research Chair (in High Frequency Electromagnetics)

NUMBER OF PAGES: XXI, 161

ABSTRACT

This thesis contributes significantly to the advancement of the response sensitivity analysis with time-domain electromagnetic (EM) solvers. The proposed self-adjoint sensitivity approaches achieve unprecedented computational efficiency. The response Jacobians are computed as a simple post-process of the field solution and the approaches can be applied with any commercial time-domain solver. The proposed sensitivity solvers are a breakthrough in the sensitivity analysis of high-frequency structures since they can be implemented as standalone software or plug-in for EM simulators. The goal is to aid the solution of microwave design and inverse problems.

The sensitivity information is crucial in engineering problems such as gradient-based optimization, yield and tolerance analyses. However, due to the lack of robust algorithms, commercial EM simulators provide only specific engineering responses not their sensitivities (or derivatives with respect to certain system parameters). The sensitivities are typically obtained by response-level finite difference (FD) approximations or parameter sweeps. For each design parameter of

interest, at least one additional full-wave analysis is performed. Such approaches can easily become prohibitively slow when the number of design parameters is large.

However, no extra system analysis is needed with the self-adjoint sensitivity analysis methods. Both the responses and their Jacobian are obtained through a single system analysis. In this thesis, two self-adjoint sensitivity solvers are introduced. They are based on a self-adjoint formulation which eliminates the need to perform adjoint system analysis. The first sensitivity solver is based on a self-adjoint formula which operates on the time waveforms of the field solution. Three different approaches associated with this sensitivity solver have been presented. The first approach adopts the staggered grid of the finite-difference time-domain (FDTD) simulation. We refer it as the original self-adjoint approach. The second approach is the efficient coarse-grid approach. It uses a coarse independent FD grid whose step size can be many times larger than that of the FDTD simulation. The third approach is the accurate central-node approach. It uses a central-node grid whose field components are collocated in the center of the traditional Yee cell.

The second self-adjoint sensitivity solver is based on a spectral sensitivity formula which operates on the spectral components of the **E**-field instead of its time waveforms. This is a memory efficient wideband sensitivity solver. It overcomes the drawback associated with our first sensitivity solver whose memory requirements may become excessive when the number of the perturbation grid points is very large. The spectral approach reduces the memory requirements roughly from Gigabytes to

Megabytes. The focus of this approach is on microwave imaging applications where our first sensitivity solver is inapplicable due to the excessive memory requirements. The proposed sensitivity solver is also well suited for microwave design problems.

The proposed self-adjoint sensitivity solvers in this thesis are verified by numerous examples. They are milestones in sensitivity analysis because they have finally made EM simulation-based optimization feasible.

ACKNOWLEDGEMENTS

This thesis would not have been possible without the help of many people. First and foremost, I would like to thank my supervisor Dr. Natalia K. Nikolova for her guidance, continued support and encouragement throughout my doctoral program. She has been a significant presence in my life. Her ability in research is a true gift, and her ideas and insights have strengthened this study significantly. I will always be thankful for her wisdom and knowledge. It has been an honor to work with her.

Next, I would like to thank my supervisory committee meeting members, Dr. Mohamed H. Bakr and Dr. Hubert deBruin, for their precious time and valuable suggestions for the work done in this thesis.

I was very lucky to have my wonderful colleagues and friends since they not only gave me a lot of support but also made my long journey much more cheerful. My thanks go to all my friends of the Computational Electromagnetics Research Lab at McMaster University, including Li Liu, Xiaying Zhu, Reza Amineh, Arshad Hasib, Aastha Trehan, Mohamed Swillam, Jie Meng and Qingsha Chen (Shasha).

I wish to thank my parents in law for their understanding and support during these years that I have pursued my doctorate.

I would like to thank my family members whom I love so much. I thank my mother for her love and endless support not only throughout the few years of my doctoral program but throughout my entire life. I also thank my sisters and brother for their love and support. Finally, I would like to thank my dearest wife Chunli for always standing by me, encouraging me and believing in me. Thanks Chunli for giving me the courage and motivation to keep going! Jiajia, my baby girl, I love you.

Contents

List of Figures

List of Tables

List of Abbreviations

RF	Radio Frequency
EM	Electromagnetic
AVM	Adjoint Variable Method
SASA	Self-Adjoint Sensitivity Analysis
CN-SASA	Central-Node Self-Adjoint Sensitivity Analysis
FD	Finite Difference
FFD	Forward Finite Difference
BFD	Backward Finite Difference
CFD	Central Finite Difference
TD	Time Domain
FDTD	Finite-Difference Time-Domain
TLM	Transmission Line Modeling
1-D	One Dimensional
2-D	Two Dimensional
3-D	Three Dimensional
TM	Transverse Magnetic mode
TEM	Transverse Electromagnetic mode
ABC	Absorbing Boundary Condition

PML	Perfect Matching Layer boundary condition
dB	Decibel

Chapter 1

INTRODUCTION

1.1 MOTIVATION

For the last five decades, RF/microwave engineers have been mainly relying on equivalent-circuit models for the design of optimal structures. However, as operating frequencies increase into the microwave band, the conventional equivalent-circuit models are no longer adequate to account for the actual electromagnetic (EM) effects of the physical layout. Nowadays, we need to consider full-wave EM effects into the design flow from the very beginning. EM simulations are necessary throughout the design process rather than being used only for final verification before prototyping. The merging of full-wave EM simulations and optimization techniques, which is usually referred to as simulation-based optimization, opens a new way for RF/microwave engineers to design high-frequency structures. Simulation-based optimization is also widely employed in solving microwave inverse problems. In comparison with microwave design problems, they are often more challenging due to the large number of the optimizable parameters. In this thesis, we address one key challenge of simulation-based optimization, namely, sensitivity analysis.

Sensitivity analysis yields the response gradients or the Jacobians with respect to the optimizable shape and material parameters. Sensitivity information is widely used in engineering problems such as optimization, modeling, tolerance and yield analysis, etc. For example, Jacobians are crucial in gradient-based optimization, which is one of the most powerful optimization approaches due to its fast convergence. However, Jacobians are not provided by current commercial EM solvers due to the lack of robust and feasible algorithms. Response Jacobians are usually estimated using response-level finite differences (FDs) or parameter sweeps. For a problem with N optimizable parameters, these approaches require at least N+1 system full-wave analyses, thus, can easily become prohibitively slow due to the excessive computational demand of the full-wave simulations. Beside their computational inefficiency, it is also known that the FD approaches are unreliable and prone to numerical errors [1].

Approaches based on the adjoint-variable method, on the other hand, are efficient and reliable. Response Jacobians are computed with at most two system analyses regardless of the number of the optimizable parameters [2]-[7]. Moreover, with the self-adjoint approaches, only one system analysis is needed to compute both the response and the response Jacobian [8]-[13]. The adjoint-problem solution is computed directly from the original field solution via simple mathematical transformations. Thus, the self-adjoint approach reduces in half the computational cost in comparison with the existing adjoint methods. The adjoint computation itself

has very small overhead, which in general varies from several seconds to a few minutes, and is always negligible compared with the time required by the simulation.

The need for adjoint-variable sensitivity analysis with full-wave EM solvers is becoming more and more imperative. However, to our knowledge, commercial full-wave EM solvers have not yet adopted adjoint-based techniques for response gradient computation due to the lack of generic and feasible adjoint-variable algorithms. Only recently, at the 2009 IEEE International Microwave Symposium, Ansoft Corporation (now part of Ansys) has announced that its High-Frequency Structure Simulator (HFSS) ver. 12, to be released by the end of 2009, will be equipped with *S*-parameter sensitivities.

This thesis addresses the above need in the case of time-domain simulations. A family of generic self-adjoint methods for sensitivity analysis with time-domain EM solvers is developed. These approaches feature both computational efficiency and high accuracy. The only requirement is to access the field solution at the so-called perturbation grid points. The Jacobian computation is done as an independent post-process of EM field solution. This makes our approaches very versatile and easy to implement. In other words, our approaches are applicable with commercial EM solvers, and can be implemented as standalone sensitivity solvers being plugged into commercial simulators for aiding the solution of microwave design and solving inverse problems.

1.2 CONTRIBUTIONS

The author has contributed substantially to a number of original developments presented in this thesis. These are briefly described next.

1.2.1 Theoretical contributions

(1) A self-adjoint algorithm for the computation of response derivatives in lossy inhomogeneous structures with time domain EM solvers.

(2) A spectral self-adjoint sensitivity method operating on the spectral components of the **E**-field.

(3) A central-node approach employing a novel independent central-node finite-difference grid for accurate self-adjoint sensitivity computation.

(4) An efficient coarse-grid approach to the adjoint sensitivity analysis with full-wave EM time-domain simulations.

(5) Implementation of self-adjoint sensitivity analysis for shape parameters of 3-D metallic structures for both time and frequency domain simulators.

1.2.2 Publications

The work presented in this thesis has been published in four refereed journal papers and nine refereed conference papers. These are cited throughout the thesis.

1.3 OUTLINE OF THE THESIS

This thesis presents novel approaches to self-adjoint sensitivity analysis (SASA) with full-wave time-domain EM solvers and their applications in microwave inverse and design problems.

In Chapter 2 we start with a brief review of the time-domain discrete adjoint sensitivity expression. We then introduce the field-mapping technique. Through field mapping, N perturbed adjoint solutions can be approximated with only one adjoint system analysis. The adjoint excitation and how to solve adjoint problem are briefly addressed in the end of Chapter. The limitations of adjoint sensitivity analyses are also discussed.

Chapter 3 addresses the SASA with EM time-domain solvers. We start with an introduction to the time-domain SASA for dielectric structures. The details of the implementation and the de-embedding technique are also described. Later, we introduce the time-domain SASA for metallic structures. The formulations and implementations are described in details. Our approaches are verified through various examples using time-domain field solutions with commercial EM solvers, which are based on the finite-difference time-domain (FDTD) and the transmission line modeling (TLM) method [14]-[15].

We address an efficient coarse-grid approach to the sensitivity analysis with full-wave EM time-domain simulations in Chapter 4. The use of coarse grids can

reduce the memory requirements and can improve the computational efficiency of the sensitivity analysis while maintaining good accuracy. We start with introducing the implementation of the coarse grid in inhomogeneous structures containing lossy dielectric objects. Then, the accuracy of the proposed coarse-grid approach is investigated through examples. We show that the sensitivity solver grid can be many times coarser than that used in the FDTD simulation. Recommendations are also given for a proper choice of the step size of the sensitivity-solver grid.

In chapter 5, we present the central-node approach for accurate self-adjoint sensitivity analysis of dielectric structures. The technique aims at lossy dielectric structures arising in biomedical applications of microwave imaging, where the dielectric losses are usually significant. By utilizing the central-node grid, the least accurate field values at the dielectric interfaces are avoided and replaced in the Jacobian computation by more accurate values at the neighboring grid points. Consequently, the achieved accuracy of the central-node approach is much better than that of the original approach in the case of dielectric structures. The Chapter describes the central-node approach for inhomogeneous structures containing lossy dielectric objects. Then, we verify our approach through various examples implemented with FDTD-based simulators [14], [16].

In Chapter 6, we present a spectral self-adjoint method for wideband sensitivity analysis. The technique reduces the memory requirements drastically by implementing a novel spectral formula, which operates on the spectral components

of the **E**-field rather than on its time waveforms. The proposed method is particularly well suited for wideband response Jacobian computation both in microwave imaging and in microwave design. In this chapter, the spectral sensitivity formula is first derived. Then, we verify the spectral approach through 1-D and 3-D examples. As an application, we show Jacobian maps utilizing the spectral approach in a realistic 3-D imaging problem. The Chapter concludes with discussions of the memory and time requirements of the spectral approach compared with those of our original time-domain approach.

The thesis concludes with Chapter 7 where suggestions for future research are outlined.

REFERENCES

[1] Y. Song and N. K. Nikolova, "Sensitivity analysis of electrically small objects in lossy inhomogeneous structures," 2007 *IEEE AP-S Int. Symp.*, pp. 4453–4456, Jun. 2006.

[2] Y. Chung, C. Cheon, I. Park, and S. Hann, "Optimal shape design of microwave device using FDTD and design sensitivity analysis," *IEEE Trans. Microwave Theory Tech.*, vol. 48, no. 12, pp. 2289–2296, Dec. 2000.

[3] Y. Chung, J. Ryu, C. Cheon, I. Park, and S. Hahn, "Optimal design method for microwave device using time domain method and design sensitivity analysis—Part I: FETD case," *IEEE Trans. Magn.*, vol. 37, no. 9, pp. 3289–3293, Sep. 2001.

[4] Y. Chung, J. Ryu, C. Cheon, I. Park, and S. Hahn, "Optimal design method for microwave device using time domain method and design sensitivity analysis—Part II: FDTD case," *IEEE Trans. Magn.*, vol. 37, no. 9, pp. 3255–3259, Sep. 2001.

[5] N. K. Nikolova, J. W. Bandler, and M. H. Bakr, "Adjoint techniques for sensitivity analysis in high-frequency structure CAD," *IEEE Trans. Microwave Theory Tech.*, vol. 52, no. 1, pp. 403–419, Jan. 2004.

[6] N. K. Nikolova, H. W. Tam, and M. H. Bakr, "Sensitivity analysis with the FDTD method on structured grids," *IEEE Trans. Microwave Theory Tech.*, vol. 52, no. 4, pp. 1207–1216, Apr. 2004.

[7] M. H. Bakr and N. K. Nikolova, "An adjoint variable method for time domain TLM with fixed structured grids," *IEEE Trans. Microwave Theory Tech.*, vol. 52, no. 2, pp. 554–559, Feb. 2004.

[8] H. Akel and J. P. Webb, "Design sensitivities for scattering-matrix calculation with tetrahedral edge elements," *IEEE Trans. Magn.*, vol. 36, no. 4, pp. 1043–1046, Jul. 2000.

[9] Q. Fang, P. M. Meaney, S. D. Geimer, K. D. Paulsen, and A. V. Streltsov, "Microwave image reconstruction from 3-D fields coupled to 2-D parameter estimation," *IEEE Trans. Med. Imag.*, vol. 23, no.4, pp. 475–484, Apr. 2004.

[10] N. K. Nikolova, Ying Li, Yan Li and M. H. Bakr, "Sensitivity analysis of scattering parameters with electromagnetic time-domain simulators," *IEEE Trans. Microwave Theory Tech.*, vol. 54, no.4, pp. 1589–1610, Apr. 2006.

[11] Y. Song, Ying Li, N. K. Nikolova, and M. H. Bakr, "Self-adjoint sensitivity analysis of lossy dielectric structures with electromagnetic time-domain simulators," *Int. J. of Numerical Modeling: Electronic Networks, Devices and Fields*, vol. 21, no. 1–2, pp. 117–132, Jan.–Apr. 2008.

[12] N. K. Nikolova, J. Zhu, D. Li, M. H. Bakr, and J. W. Bandler, "Sensitivity analysis of network parameters with electromagnetic frequency-domain simulators," *IEEE Trans. Microwave Theory Tech.*, vol. 54, no. 2, pp. 670–681, Feb. 2006.

[13] T. Rubaek, P. M. Meaney, P. Meincke, and K. D. Paulsen, "Nonlinear microwave imaging for breast-cancer screening using Gauss-Newton's method and the CGLS inversion algorithm," *IEEE Trans. Antennas Propagat.*, vol. 55, no.8, pp. 2320–2331, Aug. 2007.

[14] XFDTD v. 6.2, *Reference Manual*, Remcom, 2004, http://www.recom.com/xfdtd6/.

[15] MEFiSTo-3D® Pro v. 4, *User Guide and Operating Manual*, 6th ed., Faustus Scientific, Jan. 2003, http://www.faustcorp.com/products/mefisto3dpro/.

[16] QuickWave-3D v. 6.0, *Reference Manual*, QWED, 2006, http://www.qwed.com.pl/.

Chapter 2

ADJOINT SENSITIVITY ANALYSIS WITH TIME-DOMAIN EM SOLVERS

2.1 INTRODUCTION

The goal of sensitivity analysis is to compute the sensitivity of a given response of a structure to variations of its design parameters. Mathematically, it is represented by the gradient of the response with respect to changes in a set of design parameters as follow:

$$\nabla_{\boldsymbol{p}} F = \left[\frac{\partial F}{\partial p_1} \cdots \frac{\partial F}{\partial p_n} \right] \tag{2.1}$$

where the vector $\boldsymbol{p} = [p_1 \cdots p_n]^T$ denotes the design parameters. The EM response F is a scalar function. In time-domain sensitivity analysis, F is defined in general as [1]

$$F(\mathbf{E}, \boldsymbol{p}) = \int_0^{T_{\max}} \iiint_{\Omega} f(\mathbf{E}, \boldsymbol{p}) d\Omega dt \,. \tag{2.2}$$

Here, $T_{\max}$ denotes the simulation time and Ω is the computational volume. We refer to $f(\mathbf{E}, p)$ as the local response. It has an implicit dependence on $\boldsymbol{p}$ through the electric field $\mathbf{E}$, and may also have an explicit dependence on $\boldsymbol{p}$.

There are two major sensitivity-analysis techniques for computing (2.1): the response-level finite-difference (FD) method and the adjoint-variable method (AVM). Approaches based on the FD method are computationally inefficient. They require at least one additional analysis for each design parameter. For example, if we have n design parameters, then, n+1 full-wave simulations are required for a first-order sensitivity estimate, and $2n$+1 simulations are required for a more accurate second-order estimate. These approaches can easily become impractical if n is large due to the heavy computational cost of full-wave EM simulations.

In contrast, approaches based on the AVM offer superior efficiency since they yield response gradients with only one additional system analysis – the adjoint system analysis – regardless of the number of the design parameters. In addition, the adjoint-sensitivity technique offers high accuracy and reliability.

The adjoint sensitivity analysis with full-wave EM solvers gains growing interest in recent time, and significant progress has been made. First, exact adjoint-variable expressions with analytical system matrix derivatives are proposed for high-frequency problems with various numerical techniques on unstructured grids [2]-[5]. Analytical system matrix derivatives are only available when the coefficients of the system matrix are differentiable with respect to the grid node coordinates. Therefore, the exact approach is only applicable with EM methods on unstructured grids, such as the finite-element method. Later, second-order discrete sensitivity expressions are derived with the TLM and the FDTD method on structured grids [6]-[7]. The

discrete sensitivity approach does not require analytical system-matrix derivatives. It is more versatile compared to the exact approach. However, there is one common limitation for both the exact and the discrete adjoint-sensitivity approaches – they are only applicable with in-house codes. This is because the excitation distribution in the adjoint simulation is difficult to set up in a commercial EM solver due to its response dependent nature.

In this Chapter, we review the basics of the discrete adjoint-variable approach to sensitivity analysis with full-wave time-domain solvers. The discrete adjoint-variable approach is a milestone of our research in sensitivity analysis with EM time-domain solvers. A family of self-adjoint approaches, which are applicable to commercial EM solvers, has been successfully developed based on it. The self-adjoint approaches will be addressed in the following chapters.

2.2 GENERALIZED TIME-DOMAIN DISCRETE ADJOINT-SENSITIVITY EXPRESSION

In this section, we summarize the second-order discrete sensitivity analysis with time-domain EM solvers utilizing the principles of the adjoint-variable method [7] - [8]. The discrete sensitivity formula does not require analytical system-matrix derivatives and allows for sensitivity computations in a discrete parameter space, i.e. on structured grids. It is derived by utilizing the principle of adjoint-variable

analysis. We consider the dispersion-free, linear, isotropic, heterogeneous medium. The method, however, is also applicable to an anisotropic medium.

An EM problem in a linear medium can be described by the second-order **E**-field vector wave equation as

$$\nabla\times\mu^{-1}\nabla\times\mathbf{E}+\varepsilon\frac{\partial^2\mathbf{E}}{\partial t^2}+\sigma\frac{\partial\mathbf{E}}{\partial t}=-\frac{\partial\mathbf{J}}{\partial t} \tag{2.3}$$

where ε, μ, and σ are the tensors of the medium permittivity, permeability, and conductivity, respectively. **J** is the source current density. Wave equation (2.3) can be rewritten in a linear matrix equation after discretization as

$$\boldsymbol{M}\ddot{\boldsymbol{E}}+\boldsymbol{N}\dot{\boldsymbol{E}}+\boldsymbol{K}\boldsymbol{E}=\boldsymbol{G} \tag{2.4}$$

Hereafter, italicized vector $\boldsymbol{E}$ as well as $\hat{\boldsymbol{E}}_n$ in all formulas, to emphasize that it is a column-vector of numerical values and not a field vector in 3-D space. In (2.4), $\dot{\boldsymbol{E}}$ and $\ddot{\boldsymbol{E}}$ denote the first- and second-order derivatives of $\boldsymbol{E}$ with respect to time, respectively. Zero initial conditions are assumed, i.e., $\boldsymbol{E}(0)=0$ and $\dot{\boldsymbol{E}}(0)=0$ at $t=0$.

If the nth design parameter p_n is perturbed to $p_n+\Delta p_n$, equation (2.4) is written as follows:

$$\begin{aligned}(\boldsymbol{M}+\Delta_n\boldsymbol{M})(\ddot{\boldsymbol{E}}+\Delta_n\ddot{\boldsymbol{E}})+(\boldsymbol{N}+\Delta_n\boldsymbol{N})(\dot{\boldsymbol{E}}+\Delta_n\dot{\boldsymbol{E}})\\ +(\boldsymbol{K}+\Delta_n\boldsymbol{K})(\boldsymbol{E}+\Delta_n\boldsymbol{E})=\boldsymbol{G}+\Delta_n\boldsymbol{G}\end{aligned} \tag{2.5}$$

Taking into account (2.4) in (2.5), we get

$$\tilde{\boldsymbol{M}}_n \Delta_n \ddot{\boldsymbol{E}} + \tilde{\boldsymbol{N}}_n \Delta_n \dot{\boldsymbol{E}} + \tilde{\boldsymbol{K}}_n \Delta_n \boldsymbol{E} + \Delta_n \boldsymbol{R} = 0 \tag{2.6}$$

where

$$\tilde{\boldsymbol{M}}_n = \boldsymbol{M} + \Delta_n \boldsymbol{M}$$

$$\tilde{\boldsymbol{N}}_n = \boldsymbol{N} + \Delta_n \boldsymbol{N}$$

$$\tilde{\boldsymbol{K}}_n = \boldsymbol{K} + \Delta_n \boldsymbol{K}$$

$$\Delta_n \boldsymbol{R} = \Delta_n \boldsymbol{M} \cdot \ddot{\boldsymbol{E}} + \Delta_n \boldsymbol{N} \cdot \dot{\boldsymbol{E}} + \Delta_n \boldsymbol{K} \cdot \boldsymbol{E} - \Delta_n \boldsymbol{G}$$

Now, we multiply (2.6) with an arbitrary auxiliary vector-row $\hat{\boldsymbol{E}}_n^T$, which has the same size as $\boldsymbol{E}$; then integrate in time as follows:

$$\int_0^{T_{\max}} \hat{\boldsymbol{E}}_n^T \cdot \left(\tilde{\boldsymbol{M}}_n \Delta_n \ddot{\boldsymbol{E}} + \tilde{\boldsymbol{N}}_n \Delta_n \dot{\boldsymbol{E}} + \tilde{\boldsymbol{K}}_n \Delta_n \boldsymbol{E} \right) dt = - \int_0^{T_{\max}} \left(\hat{\boldsymbol{E}}_n^T \cdot \Delta_n \boldsymbol{R} \right) dt . \tag{2.7}$$

Integration by parts transforms (2.7) as [7]

$$\begin{aligned} &\hat{\boldsymbol{E}}_n^T \cdot \left(\tilde{\boldsymbol{M}}_n \Delta_n \dot{\boldsymbol{E}} + \tilde{\boldsymbol{N}}_n \Delta_n \boldsymbol{E} \right) \Big|_0^{T_{\max}} - \dot{\hat{\boldsymbol{E}}}_n^T \cdot \tilde{\boldsymbol{M}}_n \Delta_n \boldsymbol{E} \Big|_0^{T_{\max}} \\ &\quad + \int_0^{T_{\max}} \left(\ddot{\hat{\boldsymbol{E}}}_n^T \tilde{\boldsymbol{M}}_n + \dot{\hat{\boldsymbol{E}}}_n^T \tilde{\boldsymbol{N}}_n + \hat{\boldsymbol{E}}_n^T \tilde{\boldsymbol{K}}_n \right) \cdot \Delta_n \boldsymbol{E} \; dt = - \int_0^{T_{\max}} \left(\hat{\boldsymbol{E}}_n^T \cdot \Delta_n \boldsymbol{R} \right) dt \end{aligned} \tag{2.8}$$

where $\dot{\hat{\boldsymbol{E}}}_n$ and $\ddot{\hat{\boldsymbol{E}}}_n$ denote the first- and the second-order derivatives of $\hat{\boldsymbol{E}}_n$ with respect to time, respectively. If we assume zero terminal conditions, i.e., $\hat{\boldsymbol{E}}_n(T_{\max}) = 0$ and $\dot{\hat{\boldsymbol{E}}}_n(T_{\max}) = 0$, at $t = T_{\max}$, (2.8) becomes

$$\int_0^{T_{\max}} \left(\ddot{\hat{\boldsymbol{E}}}_n^T \tilde{\boldsymbol{M}}_n + \dot{\hat{\boldsymbol{E}}}_n^T \tilde{\boldsymbol{N}}_n + \hat{\boldsymbol{E}}_n^T \tilde{\boldsymbol{K}}_n \right) \cdot \Delta_n \boldsymbol{E} \, dt = - \int_0^{T_{\max}} \left(\hat{\boldsymbol{E}}_n^T \cdot \Delta_n \boldsymbol{R} \right) dt \tag{2.9}$$

Since the auxiliary vector $\hat{\boldsymbol{E}}_n$ is an arbitrary vector, we have the freedom to define it by setting

$$\ddot{\hat{\boldsymbol{E}}}_n^T \tilde{\boldsymbol{M}}_n - \dot{\hat{\boldsymbol{E}}}_n^T \tilde{\boldsymbol{N}}_n + \hat{\boldsymbol{E}}_n^T \tilde{\boldsymbol{K}}_n = \nabla_E f \, . \tag{2.10}$$

Now $\hat{\boldsymbol{E}}_n$ is uniquely defined by (2.10) when the boundary conditions are set to be the same as those for $\boldsymbol{E}$. Substituting (2.10) into (2.9) results in

$$\int_0^{T_{\max}} \left(\nabla_E f \cdot \Delta_n \boldsymbol{E} \right) dt = - \int_0^{T_{\max}} \left(\hat{\boldsymbol{E}}_n^T \cdot \Delta_n \boldsymbol{R} \right) dt \, . \tag{2.11}$$

From (2.2), we can compute the variation of the response function F due to a perturbation of the nth design parameter p_n. It can be expressed in terms of $\boldsymbol{E}$ as follows

$$\Delta_n F = \Delta_n^e F + \int_0^{T_{\max}} \left(\nabla_E f \cdot \Delta_n \boldsymbol{E} \right) dt \, . \tag{2.12}$$

Here, the superscript e in Δ_n^e denotes the variation related to the explicit dependence on p_n. The integration over the volume Ω in (2.2) is implicitly represented by the dot product in (2.12). We rewrite (2.12) as follows

$$\int_0^{T_{\max}} \left(\nabla_E f \cdot \Delta_n \boldsymbol{E} \right) dt = \Delta_n F - \Delta_n^e F \, . \tag{2.13}$$

Equating (2.11) and (2.13), an expression for the variation of the EM response F due to the perturbed n*th* design parameter p_n is derived as follows:

$$\Delta_n F = \Delta_n^e F - \int_0^{T_{\max}} \left(\hat{\boldsymbol{E}}_n^T \cdot \Delta_n \boldsymbol{R} \right) dt . \tag{2.14}$$

In order to compute $\Delta_n F$, we need both $\Delta_n \boldsymbol{R}$ and $\hat{\boldsymbol{E}}_n$. $\Delta_n \boldsymbol{R}$ can be calculated from (2.6) using the field solution $\boldsymbol{E}$ of the original problem (2.4) at the current design iterate. $\hat{\boldsymbol{E}}_n$ is a solution of (2.10) with zero terminal conditions. Equation (2.10) can be transformed into

$$\tilde{\boldsymbol{M}}_n^T \ddot{\hat{\boldsymbol{E}}}_n - \tilde{\boldsymbol{N}}_n^T \dot{\hat{\boldsymbol{E}}}_n + \tilde{\boldsymbol{K}}_n^T \hat{\boldsymbol{E}}_n = \left[\nabla_E f \right]^T , \tag{2.15}$$

which defines the adjoint problem. Its solution $\hat{\boldsymbol{E}}_n$ is the adjoint-variable vector.

Finally, the derivative of F with respect to p_n can be approximated by dividing both sides of (2.14) with Δp_n as follows [7]:

$$\frac{\partial F}{\partial p_n} \approx \frac{\partial^e F}{\partial p_n} - \int_0^{T_{\max}} \hat{\boldsymbol{E}}_n^T \cdot \frac{\Delta_n \boldsymbol{R}}{\Delta p_n} dt . \tag{2.16}$$

The expression in (2.16) is the discrete adjoint-sensitivity expression. The gradient of F, i.e., $\nabla_p F$, can be easily computed using (2.16) and (2.1).

We summarize the features of the sensitivity expression (2.16) below.

1) The sensitivity expression (2.16) does not assume that the elements of the difference matrices are small compared to the coefficients of the respective

system matrices. Thus, the difference matrix coefficients, which are $\Delta_n \boldsymbol{M} / \Delta \boldsymbol{p}_n$, $\Delta_n \boldsymbol{N} / \Delta \boldsymbol{p}_n$, $\Delta_n \boldsymbol{K} / \Delta \boldsymbol{p}_n$ and $\Delta_n \boldsymbol{G} / \Delta \boldsymbol{p}_n$, do not need to represent the system-matrix derivatives accurately. This is because the second-order terms $\Delta_n \boldsymbol{M} \Delta_n \ddot{\boldsymbol{E}}$, $\Delta_n \boldsymbol{N} \Delta_n \dot{\boldsymbol{E}}$, and $\Delta_n \boldsymbol{K} \Delta_n \boldsymbol{E}$ are taken into account in the sensitivity formula (2.16).

2) N perturbed adjoint system solutions $\hat{\boldsymbol{E}}_n \left(n = 1, \cdots, N\right)$ are needed. Thus, N additional adjoint-system analyses are required. This drawback is overcome with a simple mapping technique, which is discussed in Section 2.4.1. By using one-to-one field mapping, the N adjoint-field solutions $\hat{\boldsymbol{E}}_n \left(n = 1, \cdots, N\right)$ are obtained from a single adjoint-field solution $\hat{\boldsymbol{E}}$, the adjoint solution of the nominal structure.

2.3 TIME-DOMAIN DISCRETE SENSITIVITY FORMULA IN TERM OF E-FIELD

Note that the sensitivity expression (2.16) requires the difference matrices of the system. Here, we first briefly summarize how they are computed [7]-[8]. Then, the sensitivity expression is presented in terms of the original and adjoint **E**-field solutions rather than their respective vectors.

Applying central FDs [9] to the **E**-field vector wave equation (2.3), we obtain

$$\mathcal{C}^2\mathbf{E} - \alpha \cdot D_{tt}\mathbf{E} - s \cdot D_{t2}\mathbf{E} = \mathbf{G} \tag{2.17}$$

where $\mathbf{G} = \beta \cdot D_t \mathbf{J}$, and $\mathbf{J}$ is the excitation current density. The system coefficients α, β and s are as follows:

$$\alpha = \varepsilon_r \left(\frac{\Delta h}{c\Delta t} \right)^2, \ \beta = \mu_0 \frac{\Delta h^2}{\Delta t}, \ s = \frac{\sigma \mu_0 \Delta h^2}{2\Delta t}. \tag{2.18}$$

Here, ε_r is the relative permittivity, μ_0 is the permeability of vacuum, c is the speed of light in vacuum, Δt is the discretization step in time, and $\Delta h = \min(\Delta x, \Delta y, \Delta z)$ is the smallest cell size. In (2.17), $\mathcal{C}^2$ is the FD double-curl operator, D_{tt} is a second-order FD operator in time, D_{t2} and D_t are first-order FD operators in time. They are as follows:

$$D_t \mathbf{J}(t_0) = \mathbf{J}(t_0 + \Delta t/2) - \mathbf{J}(t_0 - \Delta t/2) \tag{2.19}$$

$$D_{t2}\mathbf{E}(t_0) = \mathbf{E}(t_0 + \Delta t) - \mathbf{E}(t_0 - \Delta t) \tag{2.20}$$

$$D_{tt}\mathbf{E}(t_0) = \mathbf{E}(t_0 + \Delta t) + \mathbf{E}(t_0 - \Delta t) - 2 \cdot \mathbf{E}(t_0). \tag{2.21}$$

The FD double-curl operator $\mathcal{C}^2$ produces three vector components. In rectangular coordinates, its x-component is

$$(\mathcal{C}^2\mathbf{E})_x = h_y^2 D_{yy}^{\mu} E_x + h_z^2 D_{zz}^{\mu} E_x - h_y h_x D_{yx}^{\mu} E_y - h_z h_x D_{zx}^{\mu} E_z \tag{2.22}$$

where

$$h_x = \frac{\Delta h}{\Delta x}, \ h_y = \frac{\Delta h}{\Delta y}, \ h_z = \frac{\Delta h}{\Delta z}. \tag{2.23}$$

The second-order operators in space use central differences as follows

$$D^{\mu}_{yy}E_{x(x_0,y_0,z_0)} = \frac{E_{x(x_0,y_0+\Delta y,z_0)}}{\mu_{r(x_0,y_0+\Delta y/2,z_0)}} + \frac{E_{x(x_0,y_0-\Delta y,z_0)}}{\mu_{r(x_0,y_0-\Delta y/2,z_0)}} - \left[\frac{1}{\mu_{r(x_0,y_0+\Delta y/2,z_0)}} + \frac{1}{\mu_{r(x_0,y_0-\Delta y/2,z_0)}}\right]\cdot E_{x(x_0,y_0,z_0)} \tag{2.24}$$

and

$$D^{\mu}_{yx}E_{y(x_0,y_0,z_0)} = \frac{E_{y(x_0+\Delta x/2,y_0+\Delta y/2,z_0)} - E_{y(x_0-\Delta x/2,y_0+\Delta y/2,z_0)}}{\mu_{r(x_0,y_0+\Delta y/2,z_0)}} - \frac{E_{y(x_0+\Delta x/2,y_0-\Delta y/2,z_0)} - E_{y(x_0-\Delta x/2,y_0-\Delta y/2,z_0)}}{\mu_{r(x_0,y_0-\Delta y/2,z_0)}}. \tag{2.25}$$

Here, μ_r is the relative permeability. The y and z components of $\mathcal{C}^2\mathbf{E}$ can be obtained from $(\mathcal{C}^2\mathbf{E})_x$ using the cyclic substitution $x \to y \to z \to x$.

In the case when the design parameter is a local permittivity or conductivity, the analytical derivatives of the system coefficients can be computed directly from (2.18) as follows:

$$\frac{d\alpha}{d\varepsilon_r} = \left(\frac{\Delta h}{c\Delta t}\right)^2, \quad \frac{ds}{d\sigma} = \frac{\mu_0 \Delta h^2}{2\Delta t}. \tag{2.26}$$

The derivatives of the system coefficients with respect to the shape parameters cannot be computed analytically. Instead, FD estimates are adopted. The shape parameters belong to a discrete parameter space and thus their change is always a multiple of the cell size. We assume the smallest change of one-cell size, e.g., $\Delta p_n = \pm\Delta h$ on a uniform grid. In the nth perturbed state, p_n is changed and all

other parameters are kept at their nominal values. With the change of p_n, the coefficients of (2.17) experience a stepwise change at the grid points surrounding the changing object. We refer to these points as perturbation grid points. The system coefficient α is affected only by a change in the shape of a dielectric object, which affects the permittivity at a perturbation grid point. The system coefficient s is affected by a change in the shape of a dielectric object, which affects the conductivity at a perturbation grid point. The system coefficient $\mathcal{C}^2$ can be affected by a change in the shape of a magnetic object, which changes the permeability at the perturbation grid point. $\mathcal{C}^2$ can also be affected by a change in the shape of a metallic object.

The mathematical derivation of the discrete adjoint-sensitivity expression (2.16) makes no assumption about how small the change in the system coefficient is. It takes all second-order terms in the perturbation equation into account. The resulting sensitivity formula (2.16) can be written directly in terms of the original and adjoint field solutions as [7]-[8]

$$\frac{\partial F}{\partial p_n} \approx \frac{\partial^e F}{\partial p_n} - \int_0^{T_{\max}} \iiint_{\Omega} (\hat{\mathbf{E}})_n \cdot \frac{\Delta_n R(\bar{\mathbf{E}})}{\Delta p_n} \, d\Omega \, dt, \; n = 1, \ldots, N \tag{2.27}$$

where

$$\frac{\Delta_n R(\bar{\mathbf{E}})}{\Delta p_n} = \frac{\Delta_n \mathcal{C}^2}{\Delta p_n} \cdot \bar{\mathbf{E}} - \frac{\Delta_n \alpha}{\Delta p_n} \cdot D_{tt} \bar{\mathbf{E}} - \frac{\Delta_n s}{\Delta p_n} \cdot D_{t2} \bar{\mathbf{E}} - \frac{\Delta_n \mathbf{G}}{\Delta p_n}. \tag{2.28}$$

In (2.28), $\partial^e F / \partial p_n$ denotes the explicit derivative, $\bar{\mathbf{E}}$ is the solution of (2.17) in the nominal state, and $(\hat{\mathbf{E}})_n$ is the solution of the adjoint problem in the nth perturbed state. In the nth perturbed state, p_n is changed and all other parameters are kept at their nominal values. Note that (2.27) requires the field solution $(\hat{\mathbf{E}})_n$ of N adjoint problems. In the next section, we will show a mapping technique, which can be used to obtain the field solutions of N adjoint problems using only one adjoint system analysis [10].

For the cases where the system coefficients have analytical derivatives, the adjoint-sensitivity formula in (2.27) becomes

$$\frac{\partial F}{\partial p_n} = \frac{\partial^e F}{\partial p_n} - \int_0^{T_{\max}} \iiint_{\Omega} \hat{\mathbf{E}} \cdot \frac{\partial R(\bar{\mathbf{E}})}{\partial p_n} \, d\Omega \, dt, \; n = 1, \ldots, N, \tag{2.29}$$

where

$$\frac{\partial R(\bar{\mathbf{E}})}{\partial p_n} = \frac{\partial \mathcal{C}^e}{\partial p_n} \cdot \bar{\mathbf{E}} - \frac{\partial \alpha}{\partial p_n} \cdot D_{t1} \bar{\mathbf{E}} - \frac{\partial s}{\partial p_n} \cdot D_{t2} \bar{\mathbf{E}} - \frac{\partial \mathbf{G}}{\partial p_n}. \tag{2.30}$$

Note that with analytical derivatives of the system coefficients, the adjoint solution must correspond to the unperturbed structure, i.e., $(\hat{\mathbf{E}})_n$ is replaced simply by $\hat{\mathbf{E}}$, which is the solution of the unperturbed adjoint problem. In this case, field mapping is not needed.

2.4 ADJOINT PROBLEM SOLUTION

2.4.1 Adjoint Field Mapping

The discrete sensitivity expression (2.27) requires the solutions of N adjoint problems, which means in general that we need to perform N adjoint simulations for the N perturbed states. This would eliminate the computational advantages of the adjoint-variable approach. In order to preserve the computational efficiency of the adjoint approach, a one-to-one mapping technique is adopted to approximate the solutions of the N adjoint problems [10]. This approximation is based on the perturbation theory, which states that the EM field of the structure with a small shape perturbation is not much different from that of the unperturbed structure. With this technique, we perform only one adjoint simulation for the unperturbed structure. All N perturbed-structure solutions are obtained from it. The nth perturbed adjoint field solution $(\hat{\mathbf{E}})_n$ is approximated by a simple shift in space of the unperturbed adjoint solution $\hat{\mathbf{E}}$ in the direction of the assumed perturbation. The mapping technique is only necessary for shape design parameters. In the case of material parameters, the sensitivity expression (2.29) only requires $\hat{\mathbf{E}}$, which is the solution of the adjoint problem in the nominal state.

Figure 2.1 illustrates a 2-D FD grid for a lossy dielectric rectangular object. The FD grid is shown with dot lines, and the object is denoted with a dark-grey rectangle. Let the shape parameter p_n represent the length L of the object. If we

assume an increase of L of $\Delta p_n = \Delta x$, the perturbation grid points where the system coefficients α and s experience changes are marked with red dots. We emphasize that the perturbation grid points are the only points that have contributions to the nth sensitivity of (2.27). They belong to the immediate vicinity of the perturbation boundary, where we need both the original and adjoint field solutions. Note that weighted averaging of the medium constitutive parameters is usually applied at the interface points of the FDTD grid.

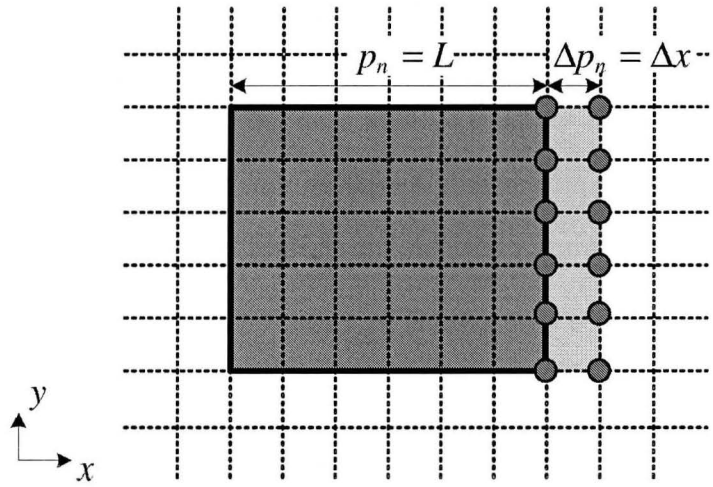

Fig. 2.1 Illustration of assumed shape change involving a length increase to the right of the dielectric object. The perturbed area is shown with light-blue cells. Red dots denote the so-called perturbation grid points where the system coefficients change.

The mapping procedure is illustrated in Figure 2.2. It shows that the adjoint solution $(\hat{E}_z)_n$ of the nth perturbed state is approximated from the nominal state solution $\hat{E}_z$ through a simple one-cell shift in the direction of the perturbation. In this case, we only record the adjoint field solution $\hat{E}_z$ of the nominal structure at the grid points marked with blue dots. The adjoint solutions $(\hat{E}_z)_n$ at perturbation grid points, which are marked with squares, are approximated by $\hat{E}_z$ at points marked with blue dots through the simple one-to-one shift, which is illustrated using arrows.

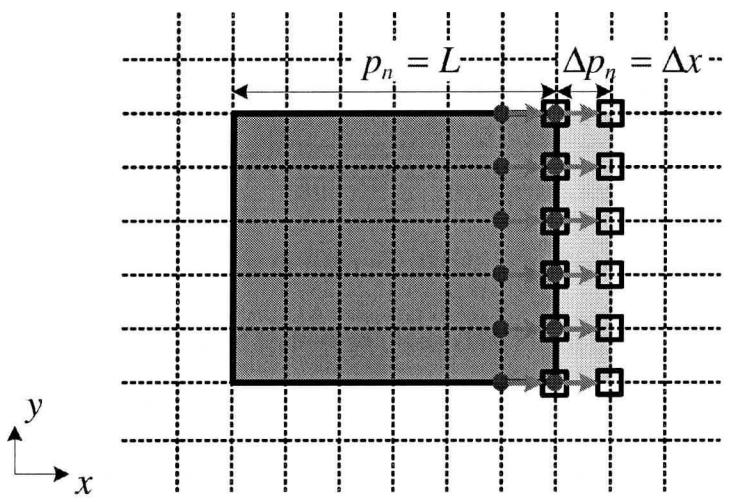

Fig. 2.2 The locations in a 2-D FDTD grid where the adjoint solution $(\hat{E}_z)_n$ is needed are marked with squares. The locations where the solution $\hat{E}_z$ of the nominal adjoint problem is actually recorded are marked with dots. Arrows illustrate the one-to-one field mapping from $\hat{E}_z$ to $(\hat{E}_z)_n$.

2.4.2 Solving the Adjoint Problem

The adjoint problem, whose solution $\hat{\mathbf{E}}$ we seek, is a quasi-EM problem governed by the vector wave equation [7]

$$\nabla\times\left[\mu^{-1}\right]^{T}\nabla\times\hat{\mathbf{E}}+\varepsilon^{T}\frac{\partial^{2}\hat{\mathbf{E}}}{\partial\tau^{2}}+\sigma^{T}\frac{\partial\hat{\mathbf{E}}}{\partial\tau}=\frac{\partial\hat{\mathbf{J}}}{\partial\tau}. \tag{2.31}$$

Equation (2.31) is complemented by the same boundary conditions as in the original problem (2.17), and by zero terminal conditions. Here, τ is the inverse-time variable, $\tau=T_{\max}-t$. The adjoint current density $\hat{\mathbf{J}}$ is response dependent. It exists only in the region where the local response f in (2.2) depends on the field solution. $\hat{\mathbf{J}}$ is defined as follows [7]

$$\beta D_{i}\hat{\mathbf{J}}=\hat{\mathbf{x}}\frac{\partial f}{\partial E_{x}}+\hat{\mathbf{y}}\frac{\partial f}{\partial E_{y}}+\hat{\mathbf{z}}\frac{\partial f}{\partial E_{z}} \tag{2.32}$$

where β is defined in (2.18). In order to solve (2.31) in τ time, the time sequence of $\hat{\mathbf{J}}$ obtained from (2.32) has to be applied backwards.

If we write (2.31) in term of ($-\hat{\mathbf{E}}$) instead of $\hat{\mathbf{E}}$, the adjoint equation becomes identical to the original EM equations. Thus, in principle, the same EM solver can be used to obtain the original and the adjoint solutions. Note that the adjoint problem is solved in inverse τ time. We emphasize that the adjoint problem excitation (adjoint current density $\hat{\mathbf{J}}$) is determined by the local response f, therefore, it is very difficult to set up in commercial EM solvers. This is why the adjoint based sensitivity

approaches have been applied only with in-house codes. This is also one of the major reasons why commercial solvers have not yet adopted adjoint-based approaches for sensitivity computation. In the rest of the thesis, we will present a class of self-adjoint approaches to overcome this limitation.

2.5 SUMMARY

In this Chapter, we reviewed the time-domain discrete adjoint technique for the sensitivity analysis using structured discretization grids. First, we summarized the derivation of the discrete adjoint-sensitivity expression using the principles of adjoint-variable analysis. The discrete expression takes into account the second-order terms, and, thus, allows for coarse difference approximations of the derivatives of the system coefficients.

Second, we discussed the field mapping technique, which is considered a breakthrough in the discrete sensitivity analysis. Through field mapping, N perturbed adjoint solutions can be obtained with only one adjoint system analysis.

We also briefly addressed how to solve the adjoint problem. Adjoint problem is a quasi-EM problem and can be solved in a very similar fashion as the original problem. The adjoint excitation is local-response dependent, which makes the adjoint sensitivity only applicable to in-house codes.

REFERENCES

[1] E. J. Haug, K. K. Choi, and V. Komkov, *Design Sensitivity Analysis of Structural Systems*. Orlando, FL: Academic, 1986.

[2] H. Akel and J. P. Webb, "Design sensitivities of scattering-matrix calculation with tetrahedral edge elements," *IEEE Trans. Magn.*, vol. 36, no.4, pp. 1043–1046, July 2000.

[3] Y. Chung, C. Cheon, I. Park, and S. Hann, "Optimal shape design of microwave device using FDTD and design sensitivity analysis," *IEEE Trans. Microwave Theory Tech.*, vol. 48, no. 12, pp. 2289–2296, Dec. 2000.

[4] Y. Chung, J. Ryu, C. Cheon, I. Park and S. Hahn, "Optimal design method for microwave device using time domain method and design sensitivity analysis – part I: FETD case," *IEEE Trans. Magnetics*, vol. 37, no. 9, pp. 3289–3293, Sep. 2001.

[5] Y. Chung, J. Ryu, C. Cheon, I. Park and S. Hahn, "Optimal design method for microwave device using time domain method and design sensitivity analysis – part II: FDTD case," *IEEE Trans. Magnetics*, vol. 37, no. 9, pp. 3255–3259, Sep. 2001.

[6] M. H. Bakr and N. K. Nikolova, "An adjoint variable method for time domain time-domain transmission-line modeling with fixed structured grids,"

IEEE Trans. Microwave Theory Tech., vol. 52, no. 2, pp. 554–559, Feb. 2004.

[7] N. K. Nikolova, H. W. Tam, and M. H. Bakr, "Sensitivity analysis with the FDTD method on structured grids," *IEEE Trans. Microwave Theory Tech.*, vol. 52, no. 4, pp. 1207–1216, April 2004.

[8] N. K. Nikolova, Ying Li, Yan Li and M. H. Bakr, "Sensitivity analysis of scattering parameters with electromagnetic time-domain simulators," *IEEE Trans. Microwave Theory Tech.*, vol. 54, no. 4, pp. 1589–1610, Apr. 2006.

[9] J. C. Strikwerda, *Finite Difference Schemes and Partial Differential Equations*. Pacific Grove, CA: Wadsworth & Brooks, 1989.

[10] M. H. Bakr and N. K. Nikolova, "An adjoint variable method for frequency domain TLM problems with conducting boundaries," *IEEE Microwave Wireless Comp. Lett.*, vol. 13, no. 9, pp. 408–410, Sept. 2003.

Chapter 3

SELF-ADJOINT SENSITIVITY ANALYSIS WITH TIME-DOMAIN EM SOLVERS

3.1 INTRODUCTION

In Chapter 2, an efficient AVM-based discrete sensitivity approach with time-domain solvers was introduced. The discrete adjoint approach produces the responses and their gradients with only two system analyses regardless of the number of design parameters. However, due to the difficulty of setting up adjoint excitation in commercial solvers, the adjoint approach is only applicable to in-house codes.

To overcome the above limitation, we propose the self-adjoint sensitivity analysis algorithm for time-domain EM solvers [1]-[2]. The self-adjoint approach computes the response Jacobians without any additional system analyses. The adjoint field solution is derived directly from the field solution of the original system, and thus the adjoint system analysis is eliminated. The overhead of the sensitivity computation is negligible in comparison with the EM simulation time. Beside its computational efficiency, our approach also features high accuracy. It has second-

order accuracy for shape-parameter sensitivities, and is exact when derivatives with respect to constitutive parameters are calculated.

More importantly, the sensitivity solver uses its own grid, and operates independently of the EM solver. The Jacobian computation is done as a post-process outside the EM solver. The only requirement is to access the field solution at user-defined points. This makes our sensitivity solver applicable with any time-domain EM solvers on both structured grids and unstructured grids.

In this Chapter, we start with an introduction to the theory of time-domain self-adjoint sensitivity analysis. Both *S*-parameter and point-wise response sensitivity formulas are presented. Subsequently, the details of the implementation and the de-embedding in the case of *S*-parameters are described. We verify our approach through a number of 1-D, 2-D and 3-D examples with a commercial time-domain EM solver [3]. The examples are divided into two classes: self-adjoint sensitivities for dielectric structures and self-adjoint sensitivities for metallic structures.

3.2 THEORY OF TIME-DOMAIN SELF-ADJOINT SENSITIVITY ANALYSIS

In this section, we first briefly summarize the time-domain discrete adjoint-sensitivity analysis, which was discussed in Chapter 2. Then, we derive self-adjoint *S*-parameter sensitivity formula and self-adjoint point-wise sensitivity formula in the time domain.

3.2.1 Summary of Time-Domain Discrete Sensitivity Analysis

The adjoint-sensitivity approach offers an efficient way to produce response Jacobian with two system analyses: original- and adjoint-system analysis. In the case of shape parameters, the derivatives of the system coefficients cannot be computed analytically when structured grids are used to discretize the problem [4]-[5]. Instead, FD estimates with one-cell perturbation are used. The sensitivity of a generic response F with respect to the nth design parameter p_n uses the original and the adjoint field solutions as follows [6]:

$$\frac{\partial F}{\partial p_n} \approx \frac{\partial^e F}{\partial p_n} - \int_0^{T_{\max}} \iiint_{\Omega} (\hat{\mathbf{E}})_n \cdot \frac{\Delta_n R(\bar{\mathbf{E}})}{\Delta p_n} \, d\Omega \, dt, \; n = 1, \ldots, N \tag{3.1}$$

where

$$\frac{\Delta_n R(\bar{\mathbf{E}})}{\Delta p_n} = \frac{\Delta_n \mathbb{C}^2}{\Delta p_n} \cdot \bar{\mathbf{E}} - \frac{\Delta_n \alpha}{\Delta p_n} \cdot D_{tt} \bar{\mathbf{E}} - \frac{\Delta_n s}{\Delta p_n} \cdot D_{t2} \bar{\mathbf{E}} - \frac{\Delta_n \mathbf{G}}{\Delta p_n} \tag{3.2}$$

Here, $\partial^e F / \partial p_n$ denotes the explicit derivative. $T_{\max}$ is the simulation time and Ω is the computational volume. The original field $\bar{\mathbf{E}}$ is the time-dependent solution of the nominal structure. The system coefficients α, β and s are [2]

$$\alpha = \varepsilon_r \left(\frac{\Delta h}{c \Delta t} \right)^2, \; \beta = \mu_0 \frac{\Delta h^2}{\Delta t}, \; s = \frac{\sigma \mu_0 \Delta h^2}{2 \Delta t}. \tag{3.3}$$

Here, c is the speed of light in vacuum, μ_0 is the permeability of vacuum, ε_r is the relative permittivity, Δt is the discretization step in time, and $\Delta h = \min(\Delta x, \Delta y, \Delta z)$ is the smallest cell size. In (3.2), $\mathcal{C}^2$ is the FD double curl operator, D_{tt} is a second-order FD operator in time, D_{t2} and D_t are first-order FD operators in time, and $\mathbf{G} = \beta \cdot D_t \mathbf{J}$ where $\mathbf{J}$ is the excitation current density.

The adjoint field $(\hat{\mathbf{E}})_n$ in (3.1) is the solution of the perturbed adjoint problem governed by (2.31). It has the same boundary conditions as the original problem. The excitation of the adjoint system is dependent on the derivative of the local response with respect to the field solution $\partial f / \partial E_\varsigma$, $\varsigma = x, y, z$ [6]. N adjoint-field solutions of the N perturbed states are obtained from only one adjoint solution of the unperturbed structure using a field-mapping technique [5]-[6].

In the case of constitutive parameters, the derivatives of the system coefficients can be computed analytically. With analytical derivatives of the system coefficients, the adjoint solution must correspond to the unperturbed structure. Thus, field mapping is not needed. The sensitivity expression is exact [2]:

$$\frac{\partial F}{\partial p_n} = \frac{\partial^e F}{\partial p_n} - \int_0^{T_{\max}} \iiint_\Omega \hat{\mathbf{E}} \cdot \frac{\partial R(\bar{\mathbf{E}})}{\partial p_n} \, d\Omega \, dt, \quad n = 1, \ldots, N \tag{3.4}$$

where $\hat{\mathbf{E}}$ is the adjoint field solution in the unperturbed state. Since perturbation in the constitutive parameters affects only the system coefficients α and s, the analytical derivative $\partial R(\bar{\mathbf{E}})/\partial p_n$ becomes

$$\frac{\partial R(\bar{\mathbf{E}})}{\partial p_n} = -\frac{\partial \alpha}{\partial p_n} \cdot D_{t1}\bar{\mathbf{E}} - \frac{\partial s}{\partial p_n} \cdot D_{t2}\bar{\mathbf{E}} \tag{3.5}$$

where

$$\frac{\partial \alpha}{\partial p_n} = \begin{cases} \left(\frac{\Delta h}{c\Delta t}\right)^2, & p_n = \varepsilon_r \\ 0, & p_n = \sigma \end{cases} \tag{3.6}$$

and

$$\frac{\partial s}{\partial p_n} = \begin{cases} 0, & p_n = \varepsilon_r \\ \frac{\mu_0 \Delta h^2}{2\Delta t}, & p_n = \sigma. \end{cases} \tag{3.7}$$

The sensitivity computation with respect to the constitutive parameters is more accurate compared to the shape parameters. This is because two approximations are avoided: the FD estimation of the derivatives of the system coefficients and the approximated adjoint solutions of the N perturbed states via field mapping.

3.2.2 Self-Adjoint *S*-Parameter Sensitivity Formula

Linear EM problems usually allow for a self-adjoint formulation of the sensitivity expression [7]. The self-adjoint algorithm takes advantage of the harmonic nature of the adjoint excitation and obtains the associated adjoint-field solutions from the original field solutions without performing adjoint simulations. The computation of adjoint solution from the original field solution is explained below.

The *S*-parameters of a multi-port structure can be expressed as [7]

$$S_{pq}^{\omega_0} = \sqrt{\frac{Z_q^{\omega_0}}{Z_p^{\omega_0}}} \cdot \frac{\tilde{F}_{pq}^{\omega_0}}{\tilde{F}_q^{\omega_0}} \tag{3.8}$$

where $Z_\xi^{\omega_0}$ $(\xi = p, q)$ is the wave impedance of the ξth port. $\tilde{F}_{pq}^{\omega_0}$ is the ω_0 spectral component of the scattered field at port p when port q is excited, and $\tilde{F}_q^{\omega_0}$ is the ω_0 spectral component of the incident field at port q. $\tilde{F}_{pq}^{\omega_0}$ and $\tilde{F}_q^{\omega_0}$ are defined as

$$\tilde{F}_{pq}^{\omega_0} = \int_0^{T_{\max}} \iint_{S_{p\text{-port}}} \mathbf{E}_q^{out}(x_p', y_p', t) \cdot \mathbf{M}_p(x_p', y_p') dx_p' dy_p' \cdot e^{-j\omega_0 t} dt \tag{3.9}$$

$$\tilde{F}_q^{\omega_0} = \int_0^{T_{\max}} \iint_{S_{q\text{-port}}} \mathbf{E}_q^{in}(x_q', y_q', t) \cdot \mathbf{M}_q(x_q', y_q') dx_q' dy_q' \cdot e^{-j\omega_0 t} dt \,. \tag{3.10}$$

Here, $\mathbf{E}_q^{out}$ is the outgoing (scattered) field at port p when port q is excited, and $\mathbf{E}_q^{in}$ is the incoming (incident) field when port q is excited. $\mathbf{M}_\xi$ is the field modal (orthonormal) vector at port ξ $(\xi = p, q)$ [8]. x_ξ' and y_ξ' are the local coordinates at the ξth port plane. The superscript ω_0 denotes the frequency at which the *S*-parameters are computed. For brevity, the superscript ω_0 will be omitted but implied in all formulas hereafter.

The port waveguides are usually assumed not to be subjected to design changes. This makes Z_p, Z_q and $\tilde{F}_q$ independent of p_n. The derivative of the *S*-

parameter with respect to the nth parameter p_n is then determined by the derivative of the response $F = \tilde{F}_{pq}$ as follows

$$\frac{\partial S_{pq}}{\partial p_n} = \sqrt{\frac{Z_q}{Z_p}} \cdot \frac{1}{\tilde{F}_q} \cdot \frac{\partial \tilde{F}_{pq}}{\partial p_n}, \quad n = 1, \ldots, N. \tag{3.11}$$

Here, the derivative of the complex response $\tilde{F}_{pq}$ can be computed using (3.1) or (3.4). $\tilde{F}_{pq}$ allows for a self-adjoint formulation of the sensitivity problem, i.e., the associated adjoint-field solution $\hat{\mathbf{E}}_p$ is obtained from the original-field solution $\mathbf{E}_p$ as explained next.

As discussed in Chapter 2, the adjoint current density $\hat{\mathbf{J}}_{pq}$ is the derivative of the local response f with respect to the field $\mathbf{E}$. The local response f associated with the response $F = \tilde{F}_{pq}$ in (3.9) can be identified by comparing with (2.2) as follows

$$f(x'_p, y'_p, t) = \begin{cases} \dfrac{\mathbf{E}_q^{out}(x'_p, y'_p, t) \cdot \mathbf{M}(x'_p, y'_p)}{\Delta z_p} \cdot e^{-j\omega_0 t}, & \text{at } p\text{th port} \\ 0, & \text{elsewhere.} \end{cases} \tag{3.12}$$

Here, Δz_p is the longitudinal cell size at the pth port. It takes care of the dimensionality of the integrand in the surface integration of (3.9) as compared to that of the volume integral in (2.2). In the case of the S-parameters, f has no explicit dependence on p_n, i.e., $\partial^e F_{pq} / \partial p_n = 0$, $n = 1, \ldots, N$.

As follows from (2.32) and (3.12), the adjoint current density $\hat{\mathbf{J}}_{pq}$ at the pth port can be computed from

$$\beta \cdot D_t \hat{\mathbf{J}}_{pq}(x_p', y_p', t) = \frac{\mathbf{M}(x_p', y_p') \cdot e^{-j\omega_0 t}}{\Delta z_p}. \tag{3.13}$$

Here, the difference time operator can be replaced with its analytical counterpart as $D_t \leftrightarrow \Delta t \cdot \frac{\partial}{\partial t}$. When the integration in time is performed, the real and the imaginary parts of $\hat{\mathbf{J}}_{pq}$ can be written as [7]

$$(-\hat{\mathbf{J}}_{pq})_R(x_p', y_p', t) = \mathbf{M}(x_p', y_p') \cdot \hat{g}_R(t) \tag{3.14}$$

$$(-\hat{\mathbf{J}}_{pq})_I(x_p', y_p', t) = \mathbf{M}(x_p', y_p') \cdot \hat{g}_I(t) \tag{3.15}$$

where

$$\hat{g}_R(t) = \frac{\sin(\omega_0 t)}{\omega_0 \beta \Delta t \Delta z_p}, \quad \hat{g}_I(t) = \frac{\cos(\omega_0 t)}{\omega_0 \beta \Delta t \Delta z_p}. \tag{3.16}$$

The adjoint excitation is taken with a minus in order to obtain the adjoint field with the correct sign. The real part of the adjoint solution $(\hat{\mathbf{E}}_{pq})_R$, which is due to $(-\hat{\mathbf{J}}_{pq})_R$, is used in the computation of the derivative of the real part of S_{pq}, The imaginary part $(\hat{\mathbf{E}}_{pq})_I$, which is due to $(-\hat{\mathbf{J}}_{pq})_I$, is used for the computation of the derivative of the imaginary part of S_{pq}. $(\hat{\mathbf{E}}_{pq})_R$ and $(\hat{\mathbf{E}}_{pq})_I$ are needed only at the perturbation grid points.

The original excitation current density $\mathbf{J}_p$ at the pth port is expressed as

$$\mathbf{J}_p(x_p', y_p', t) = J_p \cdot \mathbf{M}(x_p', y_p') \cdot g(t) . \tag{3.17}$$

Here, J_p is the magnitude of the original current density excitation and $g(t)$ is the excitation waveform.

The field solutions of the two problems are identical in their respective times if their excitations $-\hat{\mathbf{J}}_{pq}(x_p', y_p', \tau)$ and $\mathbf{J}_p(x_p', y_p', t)$ have identical distributions across the port and in time. Here, it is clear that $-\hat{\mathbf{J}}_{pq}(x_p', y_p', \tau)$ in (3.14)-(3.15) and $\mathbf{J}_p(x_p', y_p', t)$ in (3.17) have the same distributions across the port p.

When the adjoint problem is excited by $-\hat{\mathbf{J}}_{pq}$ and runs backwards in time, i.e. $\tau = T_{\max} - t$, it is equivalent to the original problem as far as the adjoint electric field $\hat{\mathbf{E}}_{pq}$ is concerned [7]. To make the adjoint simulation in τ-time identical to the original simulation in t-time, we excite the adjoint problem by the reversed pulse $\hat{g}(t) = g(T_{\max} - t)$, which is equivalent to $\hat{g}(\tau) = g(t)$. The ω_0 spectral component of the forward pulse $g(t)$ is

$$\underset{\sim}{G} = \int_0^{T_{\max}} g(t) \cdot e^{-j\omega_0 t} dt = G_m \cdot e^{j\varphi_g} , \tag{3.18}$$

which is related to that of the reversed pulse $g(T_{\max} - t) = \hat{g}(t)$ as

$$\hat{\underset{\sim}{G}} = \int_0^{T_{\max}} g(T_{\max} - t) \cdot e^{-j\omega_0 t} dt = G_m \cdot e^{-j(\omega_0 T_{\max} + \varphi_g)} = \underset{\sim}{G}^* \cdot e^{-j\omega_0 T_{\max}} . \tag{3.19}$$

Here, G_m and φ_g are the magnitude and phase of the ω_0 spectral component of $g(t)$.

From (3.18) and (3.19), it is clear that the ω_0 spectral component of $\hat{g}(t)$ is related to that of $g(t)$ as

$$\hat{g}^{\omega_0}(t) = G_m \cos(\omega_0 t - \varphi_g - \omega_0 T_{\max}). \tag{3.20}$$

Due to the equivalence between the original and the backward-running adjoint problem, the adjoint field is related to the original field at a point Q by

$$\hat{\mathbf{E}}_p(Q, T_{\max} - t) = \mathbf{E}_p(Q, t), \tag{3.21}$$

and its ω_0 spectral component is

$$\hat{E}_{\zeta p}(Q,t) = |E_{\zeta p(Q)}| \cos(\omega_0 t - \varphi_{e\zeta p(Q)} - \omega_0 T_{\max}), \quad \zeta = x, y, z. \tag{3.22}$$

Here, ζ denotes the vector component, i.e. x-, y-, or z-component. $|E_{\zeta p(Q)}|$ and $\varphi_{e\zeta p(Q)}$ are the magnitude and the phase of the ω_0 spectral component of the original $E_{\zeta p}$ waveform at point Q.

By comparing the desired adjoint excitation waveform in (3.16) with that in (3.20), the adjoint field of (3.22) should be adjusted both in magnitude and phase as [7]

$$(\hat{E}_\zeta)_R(Q,t) = \frac{|E_\zeta(Q)|}{J_{0p} G_m \omega_0 \beta \Delta t \Delta z} \cos\left(\omega_0 t - \varphi_{e\zeta p(Q)} + \varphi_g - \pi/2\right) \tag{3.23}$$

$$(\hat{E}_\varsigma)_I(Q,t) = \frac{|E_\varsigma(Q)|}{J_{0p} G_m \omega_0 \beta \Delta t \Delta z} \cos\left(\omega_0 t - \varphi_{e\varsigma p(Q)} + \varphi_g\right), \quad \varsigma = x, y, z. \quad (3.24)$$

Here, J_{0p} is the magnitude of the original current density excitation; G_m and φ_g are obtained through the Fourier transform of the original excitation waveform $g(t)$; $|E_\varsigma(Q)|$ and $\varphi_{e\varsigma p(Q)}$ are obtained through the Fourier transform of the original field at the grid point Q. Also, Δz is the longitudinal cell size at port p.

Finally, the real and imaginary parts of $\partial \tilde{F}_{pq} / \partial p_n$ are computed using (3.1) or (3.4) together with (3.23) and (3.24). The derivative of S_{pq} with respect to the nth parameter p_n is computed using (3.11).

3.2.3 Self-Adjoint Sensitivity Formula of Point-Wise Function

In open problems with a point excitation at point Q and a field observation at point P, there are no waveguide ports and the S-parameters may not be suitable response functions. Instead, we use a point-wise response function, which is analogous to an S-parameter. In comparison with the definition of an S-parameter in (3.8), the following simplifications are made: (i) the modal wave impedances are replaced by the intrinsic impedances Z_P and Z_Q of the media at point P and point Q, respectively; (ii) the incoming phasor $\tilde{F}_q$ is replaced by the ω_0 spectral component $\tilde{E}_Q$ of the incident field $E_Q(t)$ at point Q; (iii) the outgoing phasor $\tilde{F}_p$ is replaced by

the ω_0 spectral component $\tilde{E}_{PQ}$ of the observed scattered field component $E_{PQ}(t)$ at P. The point-wise response function then becomes [2]

$$F_{PQ} = \sqrt{\frac{Z_Q}{Z_P}} \cdot \frac{\tilde{E}_{PQ}}{\tilde{E}_Q}. \tag{3.25}$$

Here, $E_Q(t)$ is obtained through a reference simulation where point Q is excited in an infinite uniform medium of the same electrical properties as the medium at point Q.

The derivative of F_{PQ} with respect to the nth parameter is computed as

$$\frac{\partial F_{PQ}}{\partial p_n} = \sqrt{\frac{Z_Q}{Z_P}} \cdot \frac{1}{\tilde{E}_Q} \cdot \frac{\partial \tilde{E}_{PQ}}{\partial p_n}. \tag{3.26}$$

The derivative of $\tilde{E}_{PQ}$ is computed as that of $\tilde{F}_{pq}$ in the case of the S-parameters. The adjoint fields are derived in the same manner.

3.3 IMPLEMENTATION OF SELF-ADJOINT SENSITIVITY TECHNIQUE

We discuss in this section some implementation details of the proposed self-adjoint sensitivity algorithm. These include the acquisition of excitation waveform and the incident field waveform as well as the de-embedding technique.

3.3.1 Excitation Waveform

In order to compute G_m and φ_g in (3.23) and (3.24), we need the excitation waveform $g(t)$, which can be provided directly by most of the commercial simulators. Otherwise, the excitation waveform can be easily obtained by recording the current density waveform at any point of the excitation plane in an S-parameter analysis problem or at the excitation point Q in an open problem.

3.3.2 Reference Simulation

In the computation of the S-parameter sensitivities, the incoming field waveform $\mathbf{E}_q^{in}(x_q', y_q', t)$ in (3.10) is obtained through a reference simulation. The reference simulation is performed in an infinitely long waveguide with uniform cross section, which is the same as the cross section of port q.

For sensitivity computations in an open problem, the incident field waveform $E_Q(t)$ at point Q is obtained through a reference simulation where point Q is excited in an infinite uniform medium. The electrical properties of the uniform medium are the same as the medium at point Q. $\tilde{E}_Q$ in (3.25) is obtained from $E_Q(t)$ via Fourier transform.

In the case of $P \neq Q$, $E_{PQ}(t)$ is the field waveform recorded at point P in the nominal structure when point Q is excited. $\tilde{E}_{PQ}$ in (3.25) and (3.26) is obtained from

$E_{PQ}(t)$ via Fourier transform. In the case of $P=Q$, $E_Q(t)$ is also used to compute $E_{QQ}(t)$ as $E_{QQ}(t)=E_Q^t(t)-E_Q(t)$ where $E_Q^t(t)$ is the total field waveform recorded at excitation point Q in the nominal structure simulation.

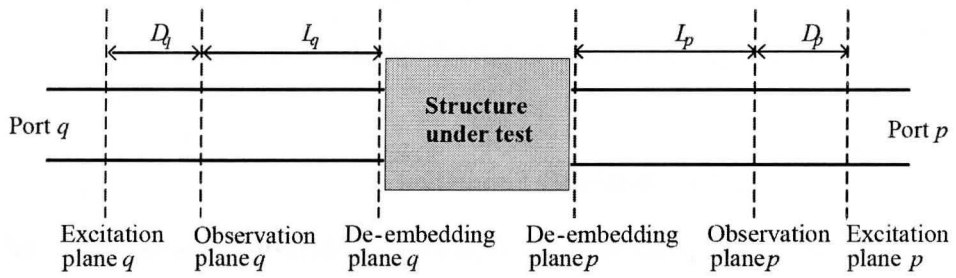

Fig. 3.1 Schematic illustration of the excitation, observation and de-embedding planes in a 2-port structure.

3.3.3 De-Embedding Technique

The de-embedding planes as shown in Figure 3.1 are the reference planes at which the *S*-parameters are extracted. They usually do not coincide with the excitation and observation planes as shown in Figure 3.1. This is because an observation plane has to be located away from discontinuities, e.g., interfaces and excitation, to avoid interference from evanescent modes. We need the de-embedding technique to account for the phase delay and, possibly, for the additional attenuation in a lossy line between the observation plane and the de-embedding plane.

The *S*-parameter definition (3.8) assumes that the de-embedding plane

coincides with the observation plane. When these two planes do not coincide, de-embedding is applied to the *S*-parameters as

$$S_{pq} = S^{o}_{pq} e^{\gamma_p L_p + \gamma_q L_q} \tag{3.27}$$

where the superscript o denotes the observation plane and γ_ξ is the complex propagation constant of the ξth port ($\gamma_\xi = \alpha_\xi + j\beta_\xi,\ \xi = p,q$). L_ξ ($\xi = p,q$) is the distance between the observation and de-embedding planes of the respective port. Now, the sensitivity expression (3.11) becomes

$$\frac{\partial S_{pq}}{\partial p_n} = \sqrt{\frac{Z_q}{Z_p}} \cdot \frac{1}{\tilde{F}^{o}_{q}} \cdot \frac{\partial \tilde{F}^{o}_{pq}}{\partial p_n} \cdot e^{\gamma_p L_p + \gamma_q L_q}. \tag{3.28}$$

The de-embedding is also needed for phase and magnitude adjustment of the adjoint field solutions. In the self-adjoint theory described previously, the adjoint excitation plane coincides with the observation plane. However, as discussed above, the observation plane is usually displaced with respect to the excitation plane. Thus, the adjoint excitation for the S_{pq} parameter associated with the observation plane at port p is displaced by D_p as shown in Figure 3.1 from the excitation plane. For the case depicted in Figure 3.1, the field solution at every point of space is delayed and attenuated (if the p-port waveguide is lossy) as compared to the field solution, which would have been obtained if the excitation was placed at the observation plane. Therefore, de-embedding is applied to the spectra of the recorded field waveforms at the perturbation grid points as

$$E_\zeta(Q)_{de} = E_\zeta(Q)\cdot e^{\gamma_p D_p},\ \zeta = x,\ y,\ z\,. \tag{3.29}$$

Note that this de-embedding can also be realized by keeping the recorded field $E_\zeta(Q)$ unchanged and modifying the ω_0 spectrum $\tilde{G}$ of the excitation waveform $g(t)$ as

$$\tilde{G}_{de} = \tilde{G}\cdot e^{-\gamma_p D_p}\,. \tag{3.30}$$

Then the adjoint solution in (3.23)-(3.24) with de-embedding becomes [2]

$$(\hat{E}_\zeta)_R(Q,t) = \frac{|E_\zeta(Q)|\cdot e^{\alpha_p D_p}}{J_{0p}G_m\omega_0\beta\Delta t\Delta z}\cos\left(\omega_0 t - \varphi_{e\zeta p(Q)} + \varphi_g - \beta_p D_p - \pi/2\right) \tag{3.31}$$

$$(\hat{E}_\zeta)_I(Q,t) = \frac{|E_\zeta(Q)|\cdot e^{\alpha_p D_p}}{J_{0p}G_m\omega_0\beta\Delta t\Delta z}\cos\left(\omega_0 t - \varphi_{e\zeta p(Q)} + \varphi_g - \beta_p D_p\right). \tag{3.32}$$

3.4 NUMERICAL EXAMPLES

We validate our self-adjoint sensitivity approach through a variety of examples. The examples include 2-D metallic structures, and 1-D, 2-D and 3-D dielectric structures. The sensitivities of the *S*-parameters and the point-wise response function (3.25) with respect to both shape and constitutive parameters are computed using the proposed self-adjoint approach and are compared with those obtained through FD estimates.

In all plots, we use TD-SASA as a notation for the results obtained by the time-domain self-adjoint sensitivity analysis method, while FFD, CFD and BFD denote the forward, central and backward FD estimates. The FD estimates use parameter perturbation of 1 Δh for shape-parameter derivatives.

3.4.1 Self-Adjoint Sensitivity for Metallic Structures

A. Single-Resonator Filter

We first illustrate the self-adjoint sensitivity analysis with a single-resonator filter as shown in Figure 3.2 [9]. The field analysis is carried out in the time domain with the FDTD-based commercial simulator XFDTD. The FDTD grid is uniform with mesh size Δh=1 mm. The size of the computational domain is 200×60×1 cells. A vertical domain size of one cell sets the XFDTD simulator into a 2-D TM mode of analysis by default.

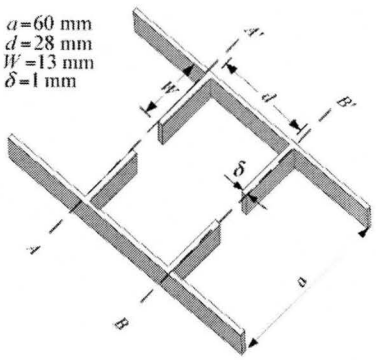

Fig. 3.2 Single-resonator filter and its nominal design parameters [9].

The structure is excited with a modulated Gaussian pulse covering the frequency band from 3 GHz to 5 GHz. We use 5 current-density excitation points placed uniformly along the excitation plane to form a half-sine modal distribution. The location of the excitation plane is 20 cells away from the Liao absorbing boundary [3] , [10] of the port.

The design parameters are $\boldsymbol{p}^T = [d\ W]$. We compute the derivatives of the S-parameters at the nominal design $[d\ W]$ = [28 13] mm. The derivatives of the real parts, the imaginary parts and the magnitudes of S_{11} and S_{21} with respect to W are shown in Figures 3.3 and 3.4. The sensitivities are computed with an assumed forward perturbation of W by one Δh, which corresponds to the metallization of one cell as shown in Figure 3.5b. It is observed that the results obtained with the self-adjoint method are in good agreement with the FD estimates. The sensitivities match best with those obtained with the central FD method, which has second-order accuracy.

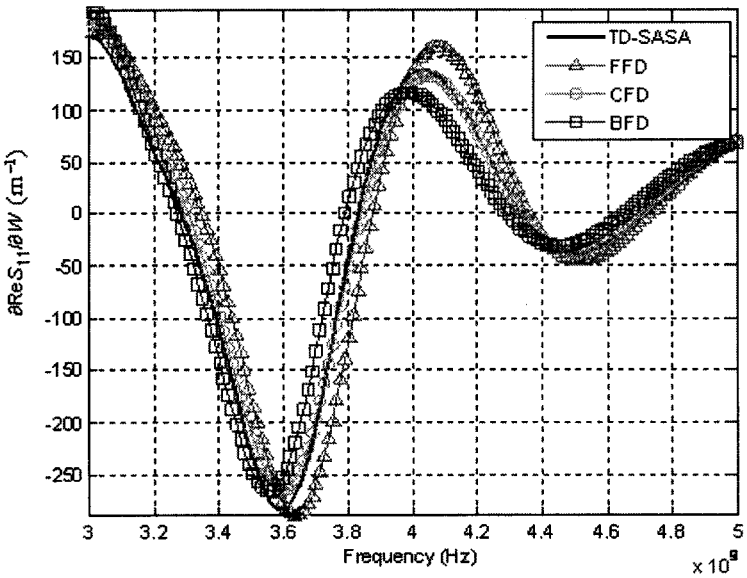
TD-SASA
FFD
CFD
BFD
150
100
50
0
-50
-100
-150
-200
-250
3
3.2
3.4
3.6
3.8
4
4.2
4.4
4.6
4.8
5
Frequency (Hz)
x 10^9
∂ReS11/∂W (m^-1)

(a)

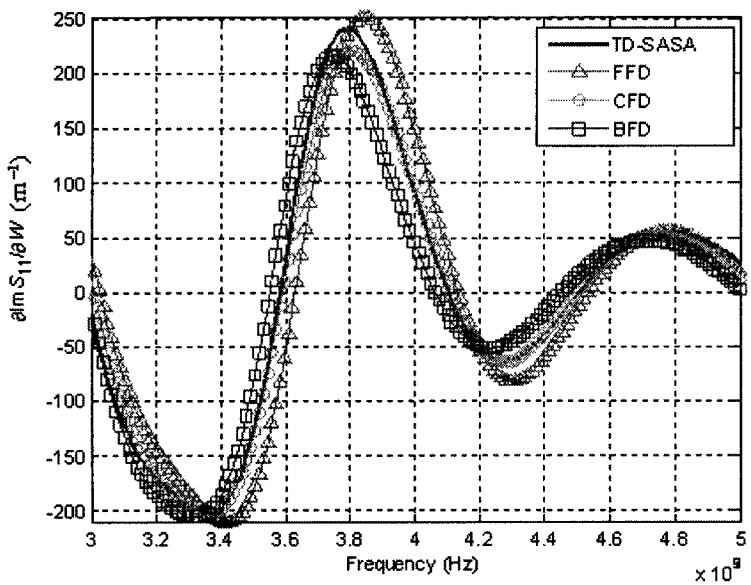
TD-SASA
FFD
CFD
BFD
250
200
150
100
50
0
-50
-100
-150
-200
3
3.2
3.4
3.6
3.8
4
4.2
4.4
4.6
4.8
5
Frequency (Hz)
x 10^9
∂ImS11/∂W (m^-1)

(b)

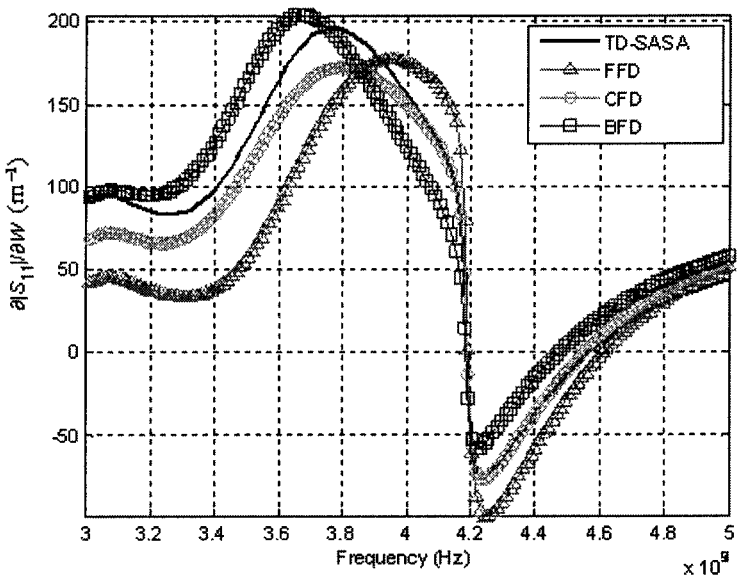

(c)

Fig. 3.3 Derivatives of S_{11} with respect to W for "metallization" case at the nominal design $[d\ W]$ = [28 13] mm in the single-resonator filter example: (a) derivative of $\mathrm{Re}(S_{11})$ with respect to W; (b) derivative of $\mathrm{Im}(S_{11})$ with respect to W; (c) derivative of $|S_{11}|$ with respect to W.

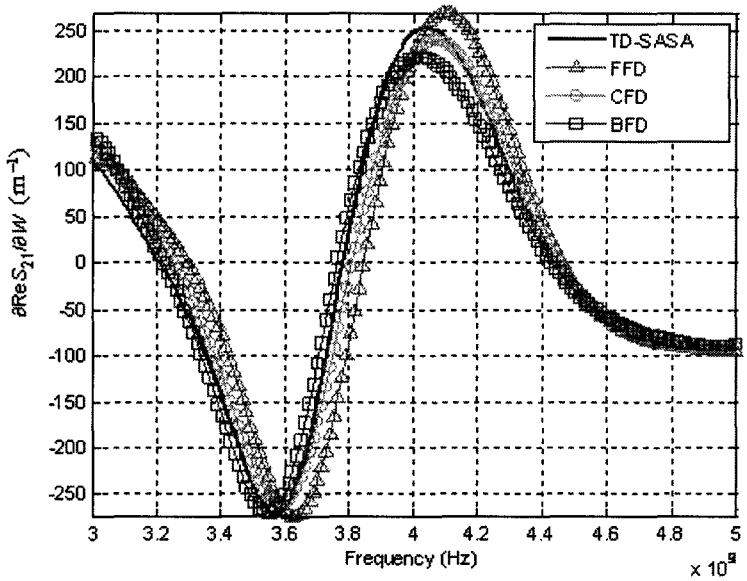
TD-SASA
FFD
CFD
BFD
∂ReS21/∂W (m-1)
Frequency (Hz)
x 10^9

(a)

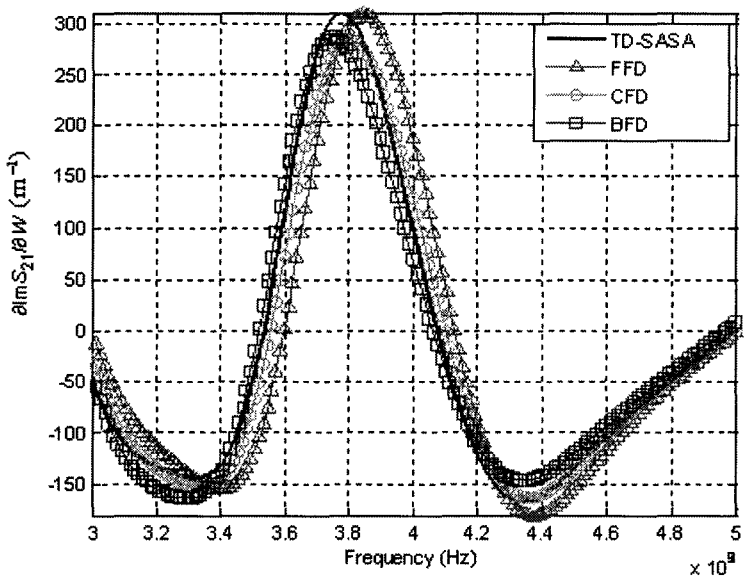
TD-SASA
FFD
CFD
BFD
∂ImS21/∂W (m-1)
Frequency (Hz)
x 10^9

(b)

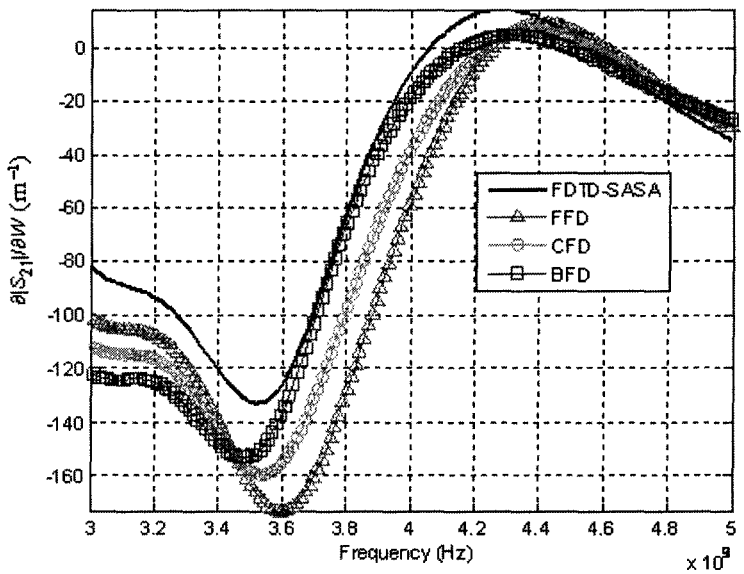

(c)

Fig. 3.4 Derivatives of S_{21} with respect to W for "metallization" case at the nominal design $[d\ W]$ = [28 13] mm in the single-resonator filter example: (a) derivative of $\mathrm{Re}(S_{21})$ with respect to W; (b) derivative of $\mathrm{Im}(S_{21})$ with respect to W; (c) derivative of $|S_{21}|$ with respect to W.

The de-metallization case is studied as well, where the derivatives are computed with an assumed backward perturbation of shape parameter by one Δh. Figure 3.5c shows the de-metallization of one cell for W. It is noted that the results obtained from these two approaches (forward and backward perturbation) are practically the same as expected. This is due to the second-order accuracy of the discrete sensitivity formula (3.1). The absolute differences between the sensitivities obtained with these two approaches are shown in Figure 3.6. They are on the order of

10^{-12} smaller compared to the values of the sensitivities themselves.

In fact, the perturbation points where system coefficients change are the same for both approaches. For example, when we compute the sensitivities with respect to *W*, the perturbation grids points are marked with crosses as shown in Figure 3.5a. The locations where the original field solution is needed are marked with circles. The locations marked with a square are the places where the adjoint fields of the perturbed adjoint problem are needed. Dots denote the locations where the field solution of the nominal original problem is recorded and used to compute the adjoint field solution of the nominal problem using (3.23) and (3.24). The adjoint field solution of the perturbed adjoint problem is obtained through a one-to-one field mapping from the adjoint field of the nominal problem [12]-[13]. The field mapping is illustrated by the arrows in Figures 3.5b-c.

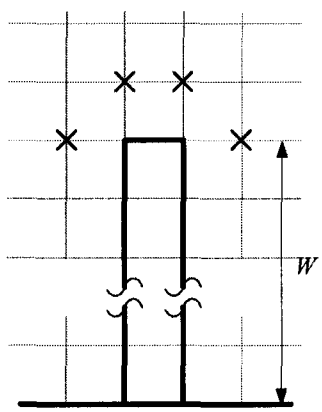

(a)

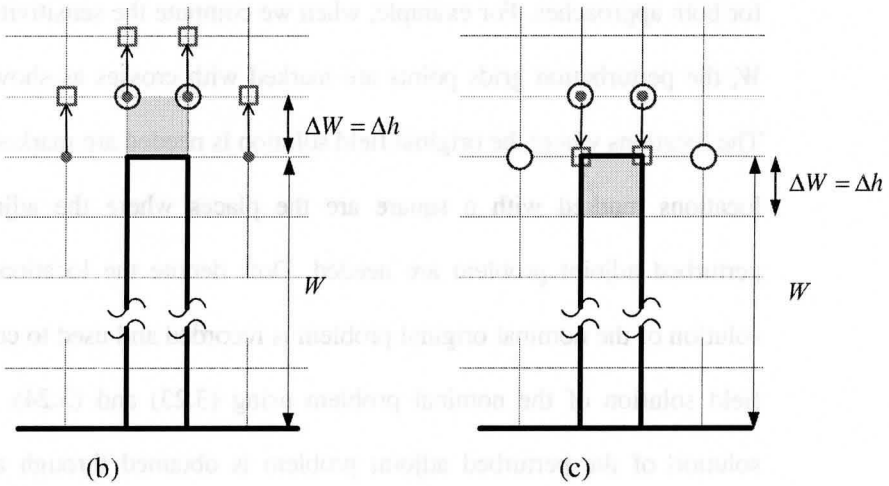

Fig. 3.5 Illustration of assumed perturbation of W in the single-resonator filter example: (a) perturbation grid points where system coefficients change; (b) assumed forward perturbation (metallization case); (c) assumed backward perturbation (de-metallization case). Crosses denote the perturbation grid points. Locations where the original and the adjoint field are needed are marked with circles and squares, respectively. Arrows illustrate the one-to-one field mapping.

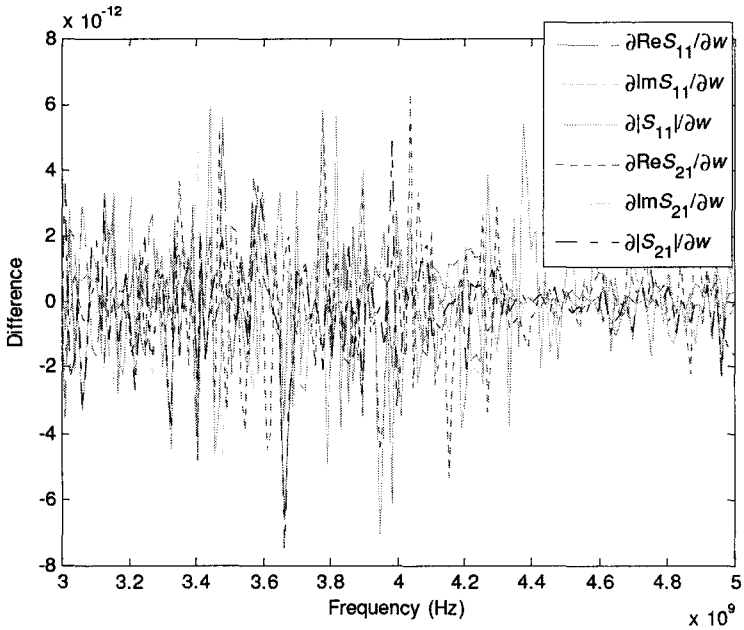

Fig. 3.6 The differences between the *S*-parameter derivatives with respect to *W* in the cases of assumed "metallization" and "de-metallization" in the single-resonator filter example.

B. H-Plane Filter

The six-resonator H-plane filter [11] is shown in Figure 3.7. All field analyses are carried out in the time domain with the FDTD-based solver XFDTD. The FDTD grid is uniform with Δh=0.6223 mm. The excitation is a modulated Gaussian pulse with spectrum from 5 GHz to 10 GHz. We use 5 probes placed uniformly along the excitation plane to form a half-sine modal distribution.

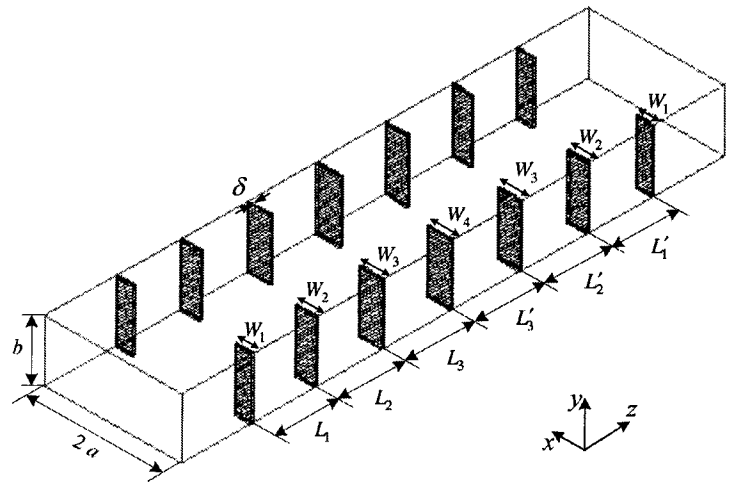

Fig. 3.7 The six-resonator H-plane filter and its nominal design parameters [11].

The design parameters are $\boldsymbol{p}^T = [a \quad b \quad \delta \quad W_1 \quad W_2 \quad W_3 \quad W_4 \quad L_1 \quad L_2 \quad L_3 \quad L_1' \quad L_2' \quad L_3']$. The nominal values of the design parameters are $[a \quad b \quad \delta \quad W_1 \quad W_2 \quad W_3 \quad W_4 \quad L_1 \quad L_2 \quad L_3 \quad L_1' \quad L_2' \quad L_3']$ = [17.4244 15.7988 0.6223 4.3561 5.6007 6.223 6.223 16.1798 16.1798 16.8021 16.1798 16.1798 16.8021] mm. We compute the S-parameter sensitivities with respect to L_1 while the other design parameters remain at their nominal values. The derivatives of the magnitudes of S_{11} and S_{21} with respect to L_1 for a sweep of L_1 at 7 GHz are plotted in Figure 3.8 and Figure 3.9, respectively. It is noted that the sensitivities computed using our self-adjoint approach match well with those obtained with the central FD approximation.

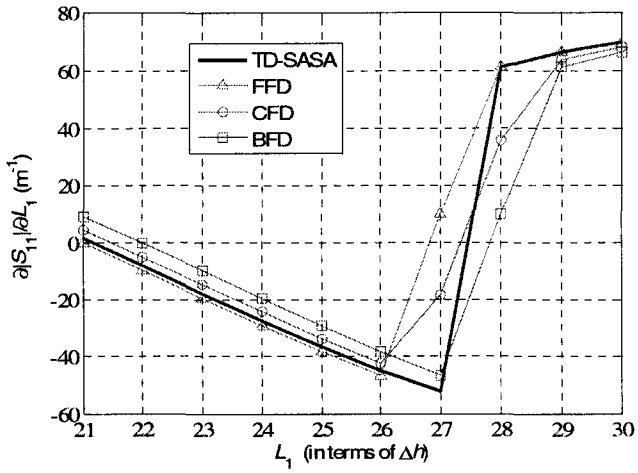

Fig. 3.8 Derivatives of $|S_{11}|$ with respect to L_1 at 7 GHz for a parameter sweep of L_1 in the H-plane filter example. All other parameters are at their nominal values.

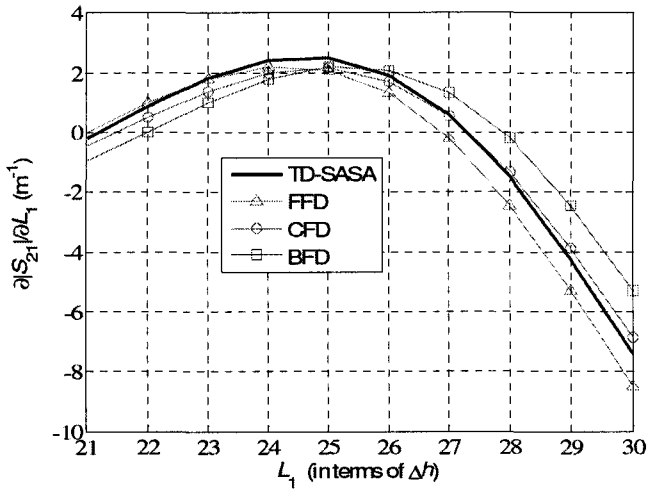

Fig. 3.9 Derivatives of $|S_{21}|$ with respect to L_1 at 7 GHz for a parameter sweep of L_1 in the H-plane filter example. All other parameters are at their nominal values.

When we compute the sensitivities with respect to L_1, an assumed shift of the first septum to the left by $1\,\Delta h$ is illustrated in Figure 3.10. The assumed shift increases the length of L_1 by $1\,\Delta h$ over its nominal value. Consequently, the grid points on the left side of the septum are metalized while those on the septum right are de-metalized. Locations where the original and the adjoint field solutions are needed are marked with circles and squares, respectively. Dots denote the locations where the field solution of the nominal original problem is actually recorded and used to compute the adjoint field solution of the nominal adjoint problem using (3.23) and (3.24). The adjoint field of the perturbed adjoint problem is obtained through a one-to-one field mapping, which is illustrated by the arrows.

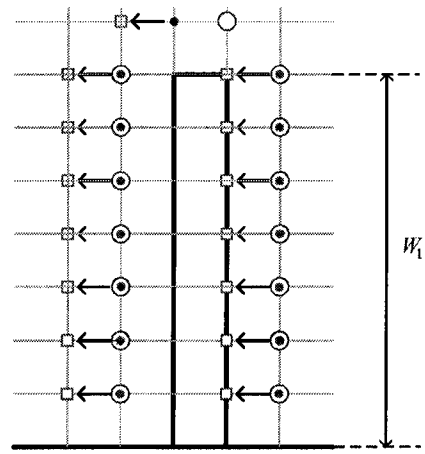

Fig. 3.10 Illustration of assumed shift of the first septum by $1\,\Delta h$ in the H-plane filter example. Locations where the original and the adjoint field solutions are needed are marked with circles and squares, respectively. Arrows illustrate the one-to-one field mapping.

3.4.2 Self-Adjoint Sensitivity for Dielectric Structures

A. 1-D Lossless Dielectric Structure

We first verify the self-adjoint approach for dielectric structures with a 1-D lossless structure. The structure and its nominal parameters are shown in Figure 3.11. Both the host medium and the central layer shown in shade are lossless.

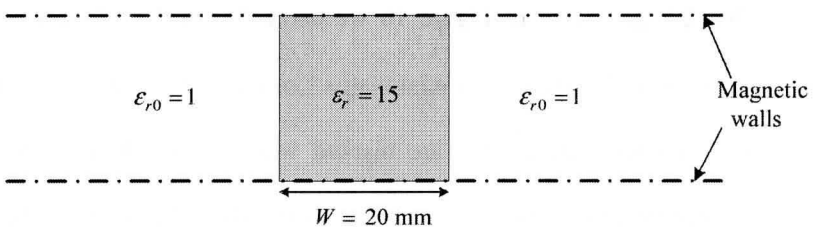

Fig. 3.11 The geometry of the 1-D structure and its nominal parameters.

All field analyses are performed over a frequency range from 3.0 GHz to 5.0 GHz with the FDTD-based solver XFDTD. Uniform mesh (Δh = 0.5 mm) is used. The excitation is a modulated Gaussian pulse, which has a uniform distribution across the port conforming to a TEM plane wave.

The design parameters are $\boldsymbol{p}^T = [\varepsilon_r \; W]$, which are the relative permittivity and the thickness of the central layer. Figures 3.12 and Figure 3.13 show the derivatives of $|S_{11}|$ and $|S_{21}|$ with respect to ε_r, respectively. Here, the CFD estimates use 4 % perturbation of ε_r over its nominal value $\varepsilon_r = 15$. Figure 3.14 and Figure

3.15 show the derivatives of $|S_{11}|$ and $|S_{21}|$ with respect to its width W, respectively. It is noted that the results obtained using our self-adjoint approach show good agreement with the CFD results.

We illustrate in Figures 3.16a-b the locations where the adjoint field and the original field are needed for the computation of the sensitivities with respect to ε_r and W, respectively. Note that the actual size of the FD grid of the central layer is $(20\times20)\,\Delta h$ while in Figure 16 we use a FD grid of $(3\times3)\,\Delta h$ to represent the central layer for the sake of simplicity. Locations where both the original and adjoint field solutions are needed are marked with squares. In the case of computing W sensitivities, the dots denote the locations where the original field of the nominal problem is actually recorded and used for the computation of the adjoint field solution of the nominal adjoint problem. Arrows illustrate the one-to-one field mapping from the adjoint field solution of the nominal problem to that of the perturbed problem. No field mapping is needed for the sensitivity computation of constitutive parameters.

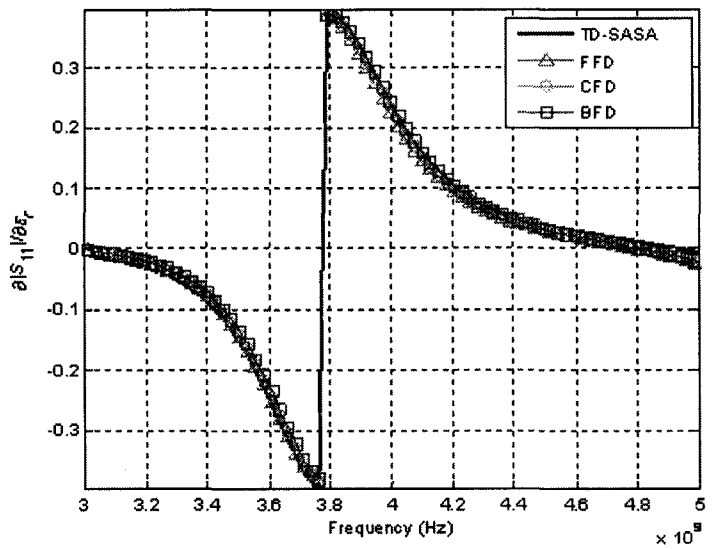

Fig. 3.12 Derivative of $|S_{11}|$ with respect to ε_r in the 1-D example.

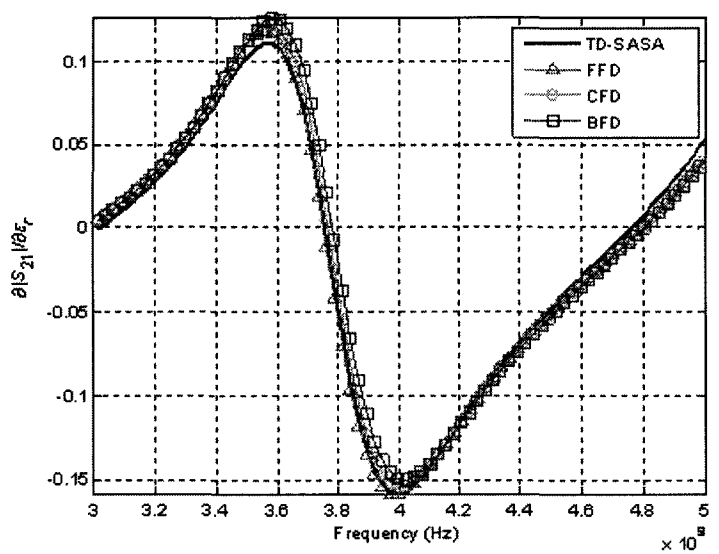

Fig. 3.13 Derivative of $|S_{21}|$ with respect to ε_r in the 1-D example.

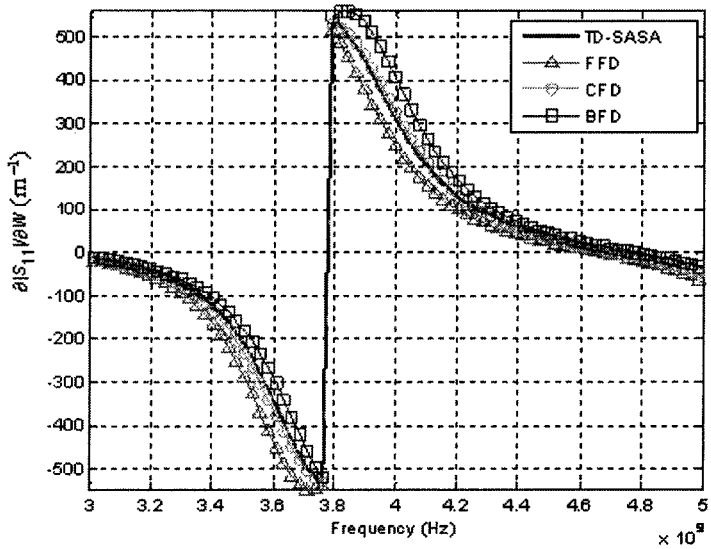

Fig. 3.14 Derivative of $|S_{11}|$ with respect to W in the 1-D example.

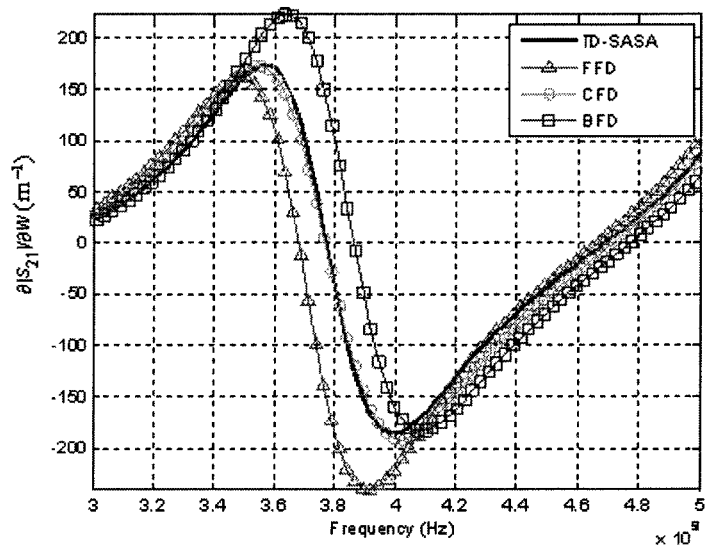

Fig. 3.15 Derivative of $|S_{21}|$ with respect to W in the 1-D example.

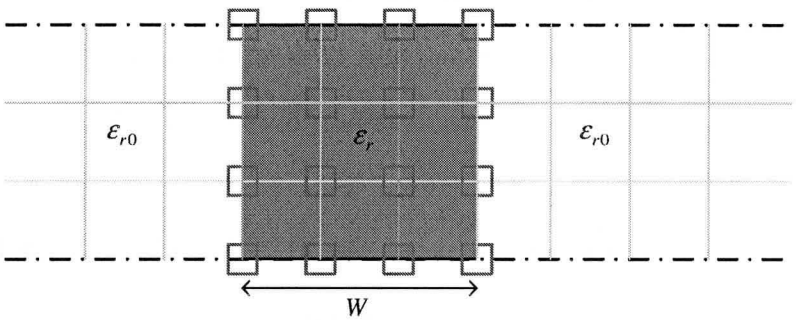

Fig. 3.16 Locations (marked with squares) where both the original and adjoint field solutions are needed for the computation of the sensitivity with respect to ε_r in the 1-D example. No field-mapping is needed.

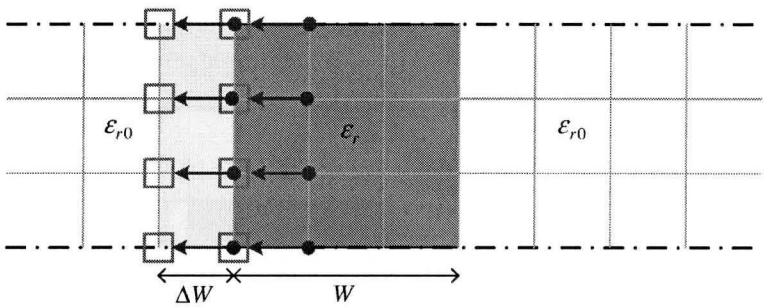

Fig. 3.17 Illustration of the assumed perturbation to the left for a derivative calculation with respect to W. Locations (marked with squares) where both the adjoint and the original field solution are needed for the computation of sensitivity with respect to W in the 1-D example. The locations (marked with dots) where the original filed solution of the nominal problem is actually recorded and used to compute the adjoint field of the nominal adjoint problem. Arrows illustrate the one-to-one field mapping.

B. 2-D Object in Lossy Layered Medium

Figure 3.18 shows the top view of the 2-D structure together with its nominal parameters [2]. The structure includes three layers with a lossy object immersed in the middle layer.

We analyze the structure with XFDTD in a 2-D H-plane. Uniform mesh with Δh = 0.5 mm is used. The excitation is a Gaussian modulated pulse covering the frequency range from 3.0 to 5.0 GHz.

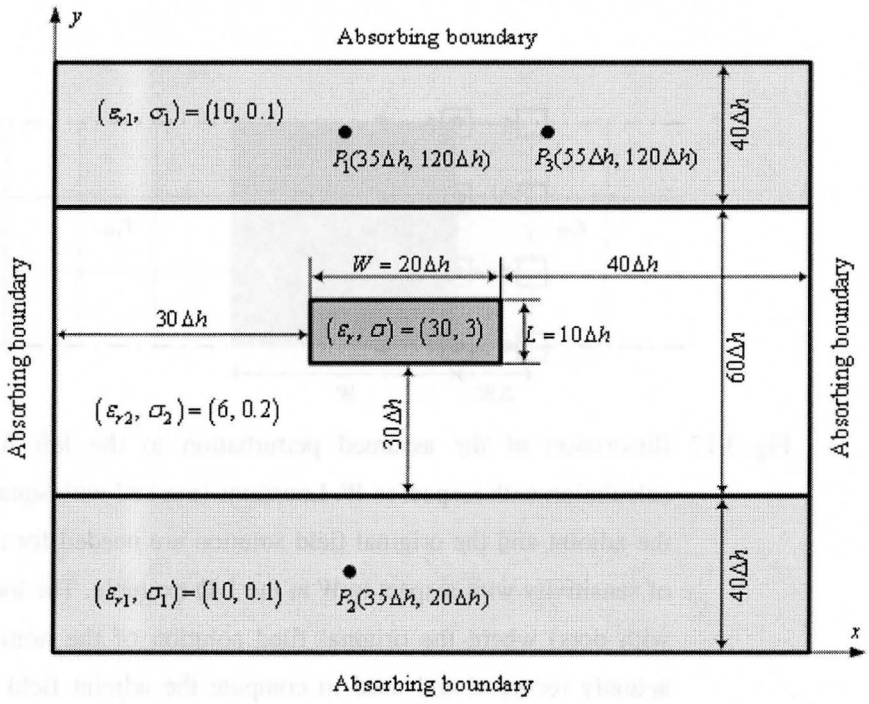

Fig. 3.18 Top view of the structure in the 2-D example and its nominal parameters.

The design parameters are $\boldsymbol{p}^T = [\varepsilon_r\ \sigma\ W\ L]$, which are the constitutive and shape parameters of the immersed object. We compute the sensitivities of the normalized response function defined in (3.25). In Figure 3.18, P_1 is the excitation point while P_2 and P_3 are the observation points. The derivatives of $\left|F_{P_1P_1}\right|$ and $\left|F_{P_2P_1}\right|$ with respect to W are plotted in Figure 3.19 and Figure 3.20, respectively. It is observed that all sensitivity curves agree with each other. The derivatives of $\left|F_{P_1P_1}\right|$ and $\left|F_{P_3P_1}\right|$ with respect to ε_r are shown in Figure 3.21 and Figure 3.22, respectively. The derivative curves of $\left|F_{P_1P_1}\right|$ and $\left|F_{P_2P_1}\right|$ with respect to σ are shown in Figure 3.23 and Figure 3.24, respectively. It is noted that the results computed using our self-adjoint method are in excellent agreement with the FD results. Here, the central FD estimates use 2 % and 6.6 % perturbations of the constitutive parameters ε_r and σ, respectively.

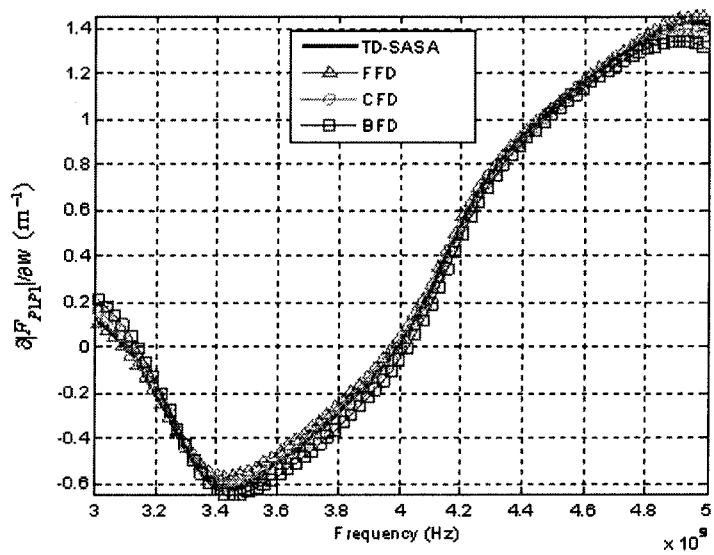

Fig. 3.19 Derivative of $\left|F_{P_1P_1}\right|$ with respect to W in the 2-D example.

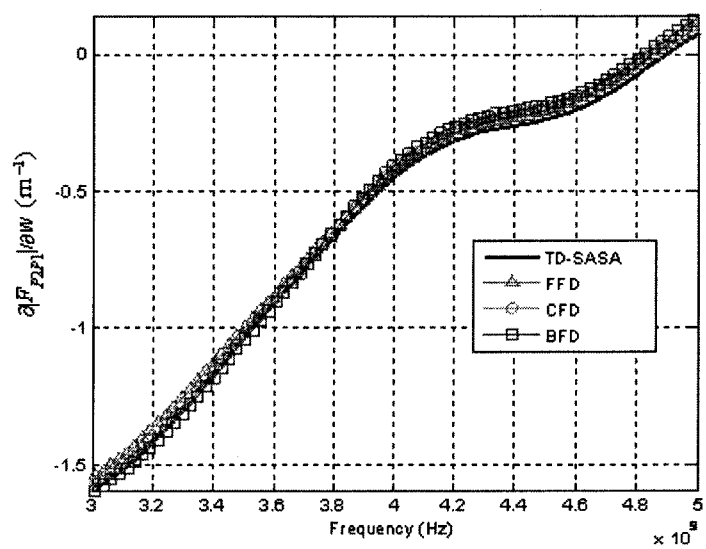

Fig. 3.20 Derivative of $\left|F_{P_2P_1}\right|$ with respect to W in the 2-D example.

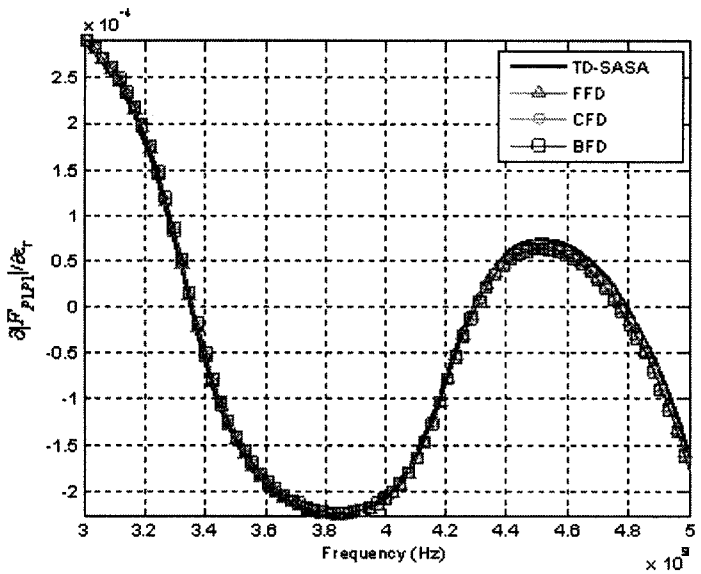

Fig. 3.21 Derivative of $\left|F_{P_1P_1}\right|$ with respect to ε_r in the 2-D example.

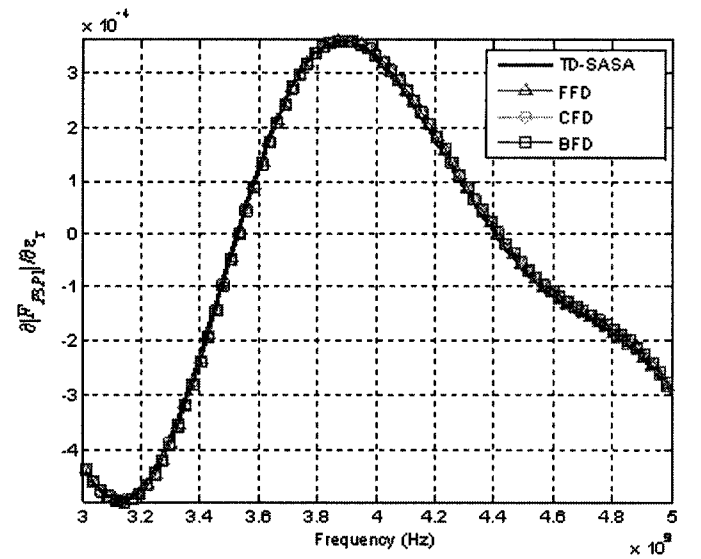

Fig. 3.22 Derivative of $\left|F_{P_3P_1}\right|$ with respect to ε_r in the 2-D example.

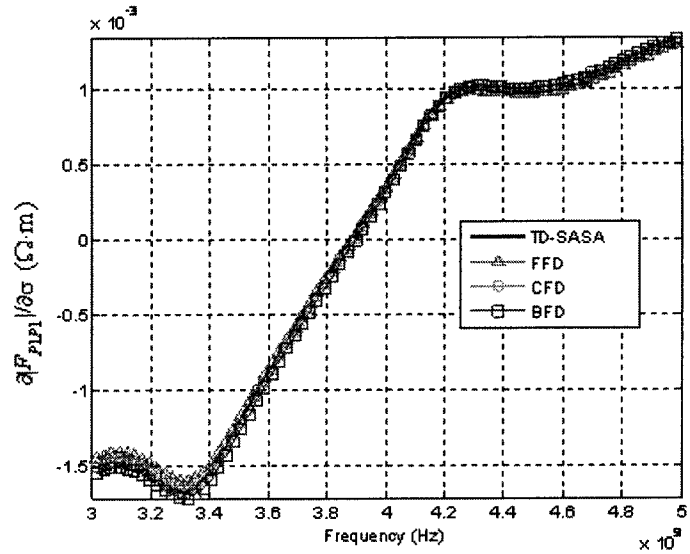

Fig. 3.23 Derivative of $\left|F_{P_1P_1}\right|$ with respect to σ in the 2-D example.

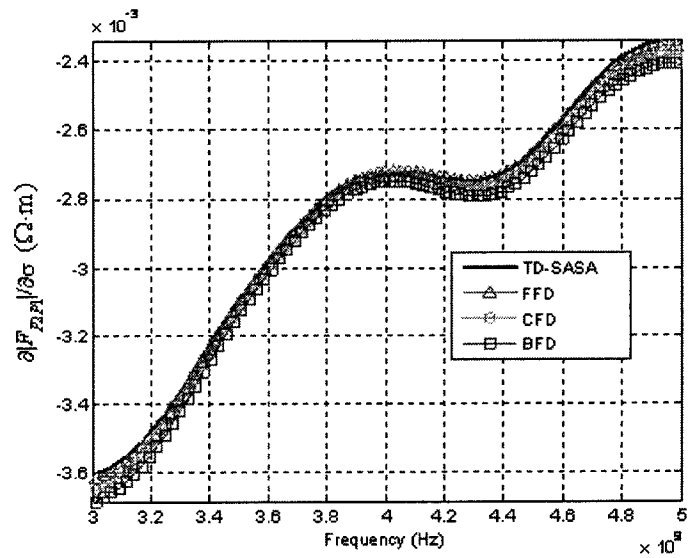

Fig. 3.24 Derivative of $\left|F_{P_2P_1}\right|$ with respect to σ in the 2-D example.

C. 3-D Object in Lossy Medium

A 2-D cross section in the x-y plane of the 3-D structure is shown in Figure 3.25 together with its nominal parameters [2]. The host medium and the immersed object are lossy. The host medium is a rectangular box with a corner at (0, 0, 0) mm. It extends 44.5 mm along the x-axis, 51.5 mm along the y-axis and 44.5 mm along the z-axis. The immersed object is a small cube of side a = 1.5 mm with a corner at (21.5, 20, 21.5) mm. The field analysis is carried out with XFDTD. Uniform mesh ($\Delta h = 0.5$ mm) is used. All boundaries are set as perfectly matched layers. The excitation is the same as in the 2-D example.

The optimizable parameters are $\boldsymbol{p}^T = [a \ \varepsilon_{r2} \ \sigma_2]$, which are the size and the constitutive parameters of the immersed object. The point-wise response function defined in (3.25) is used. In Figure 3.25, Q is the excitation point located at (15, 36.5, 22.5) mm while P is the observation point located at (26.5, 36.5, 22.5) mm. The derivatives of $|F_{QQ}|$ and $|F_{PQ}|$ with respect to the side a of the immersed object is shown in Figure 3.26 and Figure 3.27, respectively. The derivatives of $|F_{PQ}|$ with respect to ε_{r2} and with respect to σ_2 are plotted in Figure 3.28 and Figure 3.29, respectively. It is observed that the results obtained using our self-adjoint approach are in very good agreement with the CFD results. In order to obtain reliable CFD estimates, *trial and error* is used to determine the proper parameter perturbations.

Here, the CFD estimates use 50 % perturbation of the nominal value of ε_{r3} and 100 % perturbation of the nominal value of σ_3.

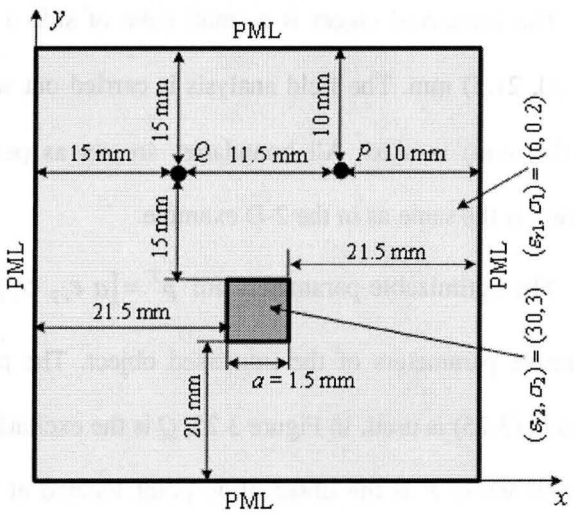

Fig. 3.25 2-D cross section in the *x*-*y* plane of the 3-D example and its nominal parameters.

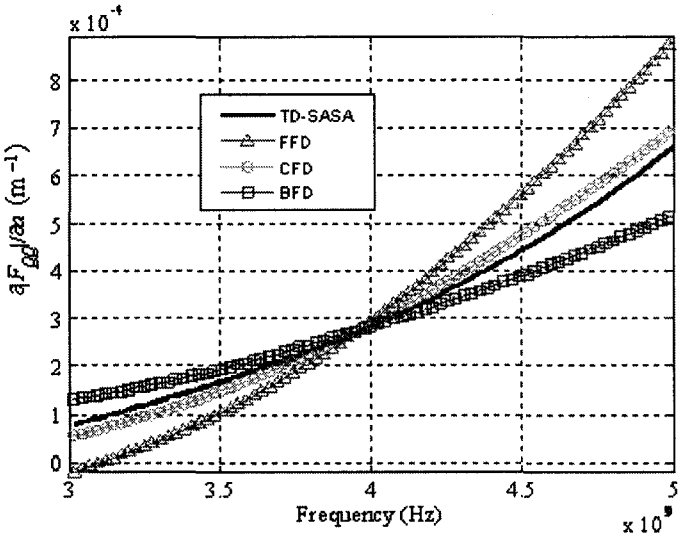

Fig. 3.26 Derivatives of $|F_{QQ}|$ with respect to a in the 3-D example.

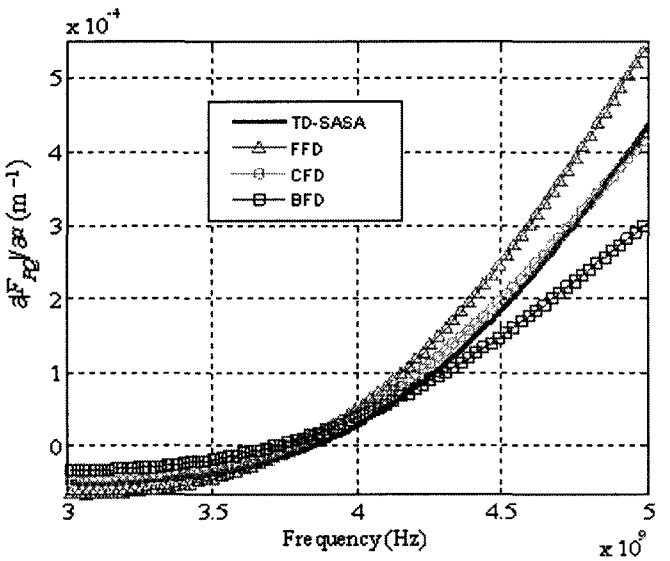

Fig. 3.27 Derivatives of $|F_{PQ}|$ with respect to a in the 3-D example.

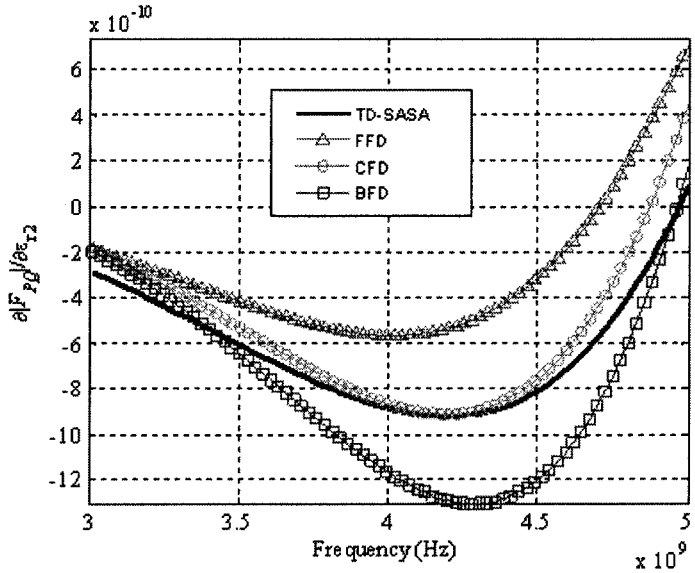

Fig. 3.28 Derivative of $|F_{PQ}|$ with respect to ε_{r2} in the 3-D example.

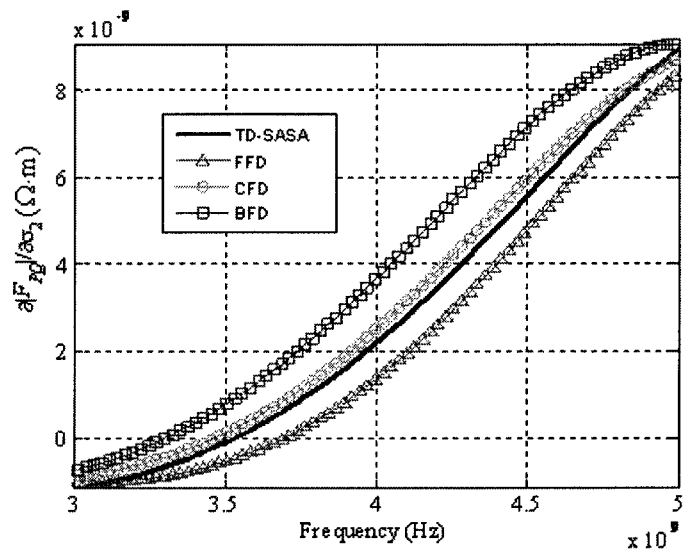

Fig. 3.29 Derivative of $|F_{PQ}|$ with respect to σ_2 in the 3-D example.

3.5 SUMMARY

In this Chapter, we presented the time-domain self-adjoint sensitivity analysis method for the computation of the response derivatives with respect to constitutive and shape parameters. The *S*-parameter sensitivity formula and self-adjoint point-wise sensitivity formula in the time domain are introduced. The implementation details are also discussed.

Our self-adjoint method is based on its own FD grid, which is independent of the EM solvers. It can provide Jacobians of second-order accuracy with negligible computational overhead regardless of the number of design or optimizable parameters. The approach is developed for easy standalone software implementations aiding microwave design and modeling in conjunction with any commercial time-domain computer-aided design package.

We have verified the self-adjoint approach through a number of examples, which include 1-D and 2-D metallic structures, 1-D lossless dielectric structure, 2-D and 3-D lossy dielectric structures. The sensitivities obtained using our self-adjoint method have good agreement with those obtained using central FD estimates. All field solutions are obtained with a FDTD-based commercial EM simulator.

REFERENCES

[1] N. K. Nikolova, Ying Li, Yan Li and M. H. Bakr, "Sensitivity analysis of scattering parameters with electromagnetic time-domain simulators," *IEEE Trans. Microwave Theory Tech.*, vol. 54, no. 4, pp. 1589–1610, Apr. 2006.

[2] Y. Song, Ying Li, N. K. Nikolova, and M. H. Bakr, "Self-adjoint sensitivity analysis of lossy dielectric structures with electromagnetic time-domain simulators," *Int. J. of Numerical Modeling: Electronic Networks, Devices and Fields*, vol. 21, no. 1–2, pp. 117–132, Jan.–Apr. 2008.

[3] XFDTD v. 6.2, *Reference Manual*, Remcom, 2004, http://www.recom.com/xfdtd6/.

[4] N. K. Nikolova, J. W. Bandler, and M. H. Bakr, "Adjoint techniques for sensitivity analysis in high-frequency structure CAD," *IEEE Trans. Microwave Theory Tech.*, vol. 52, no. 1, pp. 403–419, Jan. 2004.

[5] M. H. Bakr and N. K. Nikolova, "An adjoint variable method for time domain time-domain transmission-line modeling with fixed structured grids," *IEEE Trans. Microwave Theory Tech.*, vol. 52, no. 2, pp. 554–559, Feb. 2004.

[6] N. K. Nikolova, H. W. Tam, and M. H. Bakr, "Sensitivity analysis with the FDTD method on structured grids," *IEEE Trans. Microwave Theory Tech.*, vol. 52, no. 4, pp. 1207–1216, April 2004.

[7] N. K. Nikolova, Ying Li, Yan Li, and M. H. Bakr, "Self-adjoint Sensitivity Analysis of Linear Electromagnetic Problems in the Time Domain," *The 22nd Int. Review of Progress in Applied Computational Electromagnetics (ACES 2006)*, Mar. 2006, pp. 685–690.

[8] N. Marcuvitz, *Waveguide Handbook.* London, UK: Peter Peregrinus Ltd., 1993 reprint, Chapter 2.

[9] M. H. Bakr and N. K. Nikolova, "An adjoint variable method for time domain TLM with fixed structured grids," *IEEE Trans. Microw. Theory Tech.*, vol. 52, no. 2, pp. 554–559, Feb. 2004.

[10] Z. P. Liao, H. L. Wong, Y. Baipo, and Y. Yifan, "A transmitting boundary for transient wave analyses," *Sci. Sinica*, ser. A, vol. XXVII, no. 10, pp. 1063–1076, Oct. 1984.

[11] G. Matthaei, L. Young, and E. M. T. Jones, *Microwave Filters, Impedance-Matching Networks, and Coupling Structures.* Norwood, MA: Artech House, 1980, p. 545.

[12] M. H. Bakr and N. K. Nikolova, "An adjoint variable method for frequency domain TLM problems with conducting boundaries," *IEEE Microwave Wireless Comp. Lett.*, vol. 13, pp. 408–410, Sept. 2003.

[13] N. K. Nikolova, H.W. Tam, and M. H. Bakr, "Sensitivity analysis with the FDTD method on structured grids," *IEEE Trans. Microw. Theory Tech.*, vol. 52, no. 4, pp. 1207–1216, Apr. 2004.

Chapter 4

SELF-ADJOINT SENSITIVITIES WITH COARSE-GRID APPROACH

4.1 INTRODUCTION

In Chapter 3 we presented an efficient discrete self-adjoint approach for the computation of the response sensitivities with time-domain solvers [5]-[2]. The proposed technique needs only one EM system analysis to compute both the responses and their Jacobian matrices regardless of the number of the optimizable parameters. More importantly, it is applicable with commercial EM simulators. The only requirement is that the EM solver can export the field solution at user-defined points.

In the original self-adjoint approach, the sensitivity solver adopts the grid of the FDTD simulation for the computation of the response gradient. In order to compute the response sensitivity using an adjoint approach, the waveforms of all three **E**-field components at all perturbation grid points need to be saved and post-processed. Therefore, the memory requirements of the response sensitivity analysis may become excessive for electrically large objects or problems with a large number

of optimizable parameters. For some time-domain solvers, the speed of the overall simulation may be affected as well. This happens if the simulator stores on the hard disk the requested **E**-field solution at each iteration [3]. Slow-down due to recording the field solution is insignificant if the latter is exported after the simulation is over [4]. Even in this case, when the time-domain simulation is very long and the number of required field points is large, the memory requirements may easily become unmanageable for most computers.

In order to alleviate the problems described above, we propose the use of an independent coarse FD grid of the sensitivity solver [5]. The use of coarse grids can reduce the memory requirements drastically and improve the computational efficiency of the sensitivity analysis while maintaining good accuracy. Applications focus on lossy dielectric media as those used to model high-frequency problems arising in biomedical applications of microwave imaging.

In this Chapter, we show that the sensitivity solver grid can be many times larger than the one used in the FDTD simulation. We first describe the implementation of the coarse-grid in inhomogeneous structures containing lossy dielectric objects. We then investigate the accuracy of the proposed coarse grid approach through 1-D, 2-D and 3-D examples. Recommendations are given for a proper choice of the step size for the sensitivity solver grid.

4.2 SENSITIVITY SOLVER GRID

In our discrete self-adjoint sensitivity analysis method, the computational domain is discretized into rectangular cells as in a FD grid. Figure 4.1 illustrates the FD 2-D grid for a dielectric rectangular object, which is modeled with constitutive parameters ε_{r2} and σ_2. The host medium is modeled with ε_{r1} and σ_1. The vertical **E**-field component of a 2-D TM mode is computed at the nodes of the grid. In our original self-adjoint approach [1]-[2] introduced in Chapter 3, the sensitivity solver adopts the grid of the FDTD simulation. In order to compute the response Jacobians, the field at all perturbation grid points is stored and post-processed. For example, if the response derivatives with respect to ε_{r2} and σ_2 are computed, the waveforms of all nodes marked with dots in Figure 4.1a must be stored. The dash lines in Figure 4.1 denote the grid of the FDTD simulation.

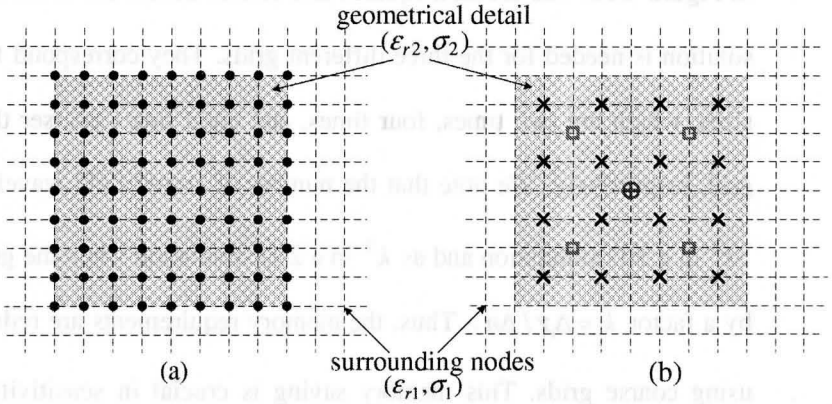

Fig. 4.1 Sensitivity solver grid in the case of constitutive parameters: (a) the fine simulation grid; (b) the coarse sensitivity-analysis grids.

Since the grid of the sensitivity solver is used only to compute the sensitivity integral in the expression (3.1) or (3.4), it can be independent of the simulation grid. Here, we use $\Delta\chi$ to denote the step size of the sensitivity solver grid, which can be many times larger than the step size Δh used by the FDTD simulation. While Δh relates to Δt through the Courant stability condition [6], $\Delta\chi$ is limited only by the smoothness of the integrated field quantity in the perturbation region. We emphasize that a coarse grid for the sensitivity calculation does not imply in any way a possibility to use a coarse grid in the FDTD simulation. The accuracy of the sensitivity calculation depends crucially on the accuracy of the field solution and, therefore, the grid of the EM simulation must remain fine enough to ensure convergent numerical analysis.

To illustrate the coarse grid of the sensitivity solver, three different are shown in Figure 4.1b. The crosses, squares and circles denote the locations where the field solution is needed for the three different grids. They correspond to sensitivity mesh sizes, which are two times, four times, and eight times coarser than the simulation grid, respectively. We note that the number of stored field waveforms decreases as $3k^3$ in a 3-D simulation and as k^2 in a 2-D simulation when the grid is made coarser by a factor $k = \Delta\chi / \Delta h$. Thus, the memory requirements are reduced drastically by using coarse grids. This memory saving is crucial in sensitivity computation for electrically large objects or problems with large number of optimizable parameters,

where the memory requirements may be excessive.

The coarse sensitivity-solver grid can be applied to shape parameters in the same manner as constitutive parameters. The savings in memory are not as dramatic as in the case of constitutive parameters since perturbation grid points exist only at the object's interfaces instead of its whole volume. For instance, when the response gradient with respect to w is computed, the nodes where the field is saved are shown in Figures 4.2a-b. The dots in Figure 4.2a are the perturbation nodes for our original approach. Figure 4.2b shows the coarse grids that our sensitivity solver can use. Crosses denote the case when $\Delta\chi = 2\Delta h$ (12 nodes), squares for $\Delta\chi = 4\Delta h$ (6 nodes), and circles for $\Delta\chi = 8\Delta h$ (3 nodes). Again, the FDTD simulation grid is shown with dash lines.

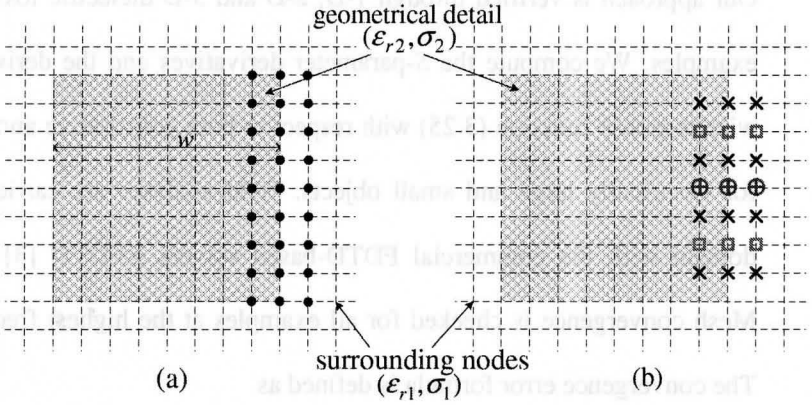

Fig. 4.2 Sensitivity solver grid in the case of shape parameters: (a) the fine simulation grid; (b) the coarse sensitivity-analysis grids.

Coarse grids are needed for computationally large objects, i.e., objects which are more than several Δh in size, due to the excessive memory requirements. For computationally small objects, we suggest that the sensitivity solver adopts the simulation grid, i.e. $\Delta\chi = \pm\Delta h$. In the case of computationally large objects, we investigate the limits of the factor $k = \Delta\chi / \Delta h$, below which the Jacobian computation is of acceptable accuracy. We consider 1-D, 2-D and 3-D examples in the next section. Recommendations are given for a proper choice of the step size of the sensitivity solver grid in different situations.

4.3 NUMERICAL EXAMPLES

Our approach is verified through 1-D, 2-D and 3-D dielectric lossy inhomogeneous examples. We compute the *S*-parameter derivatives and the derivatives of a point-wise response function (3.25) with respect to both constitutive and shape parameters for electrically large and small objects. Field analyses are carried out in the time domain with the commercial FDTD-based solvers XFDTD [3] and QW-3D [4]. Mesh convergence is checked for all examples at the highest frequency of interest. The convergence error formula is defined as

$$e = \left| \tilde{E}_\zeta^{(k+1)} - \tilde{E}_\zeta^{(k)} \right| / \left| \tilde{E}_\zeta^{(k+1)} \right|, \qquad \zeta = x,\ y,\ z. \tag{4.1}$$

Here, the superscripts denote two consecutive mesh sizes. $\tilde{E}_{\zeta}^{(k+1)}$ and $\tilde{E}_{\zeta}^{(k)}$ are the phasors of the field solutions for two consecutive mesh sizes at the highest frequency of interest. This error is usually monitored at the ports for *S*-parameter analysis or at the observation points *P* and *Q*.

In all plots, the results obtained using the original approach of our self-adjoint sensitivity analysis are marked as FDTD-SASA. The results obtained using coarse-grid schemes of the self-adjoint sensitivity analysis are marked as '$\Delta\chi = k\Delta h$', which means that the sensitivity-solver grid is k times coarser than the FDTD grid. The results estimated using the forward, central and backward finite differences at the response level are marked as FFD, CFD and BFD, respectively. For shape parameter derivatives, the FD estimates use parameter perturbation of $1\Delta h$ unless specified otherwise in brackets in the plot's legend. For material-parameter derivatives, the amount of parameter perturbation is shown in brackets as a percentage of the nominal value. Wherever available, analytical results are marked as 'Analytical'. All analyses are performed over a frequency range from 3.0 GHz to 5.0 GHz.

A. Parallel-Plate Waveguide with an Electrically Large Middle Layer

We first illustrate the coarse-grid approach with a parallel-plate waveguide with an electrically large central layer. The geometry of the parallel-plate waveguide and its parameters are shown in Figure 4.3. Uniform mesh ($\Delta h = 0.25$ mm) is used in the

FDTD simulation with a mesh convergence error less than 5 %. The excitation is a modulated Gaussian pulse. It has a uniform distribution across the port conforming to a TEM plane wave.

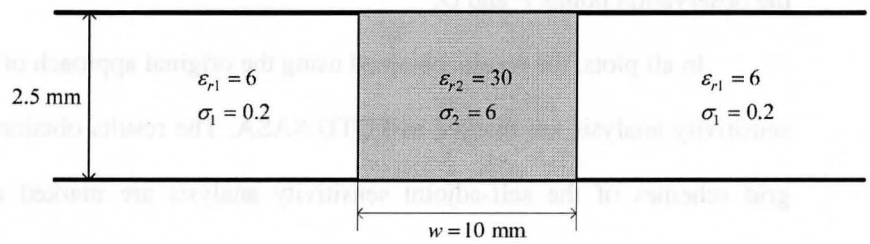

Fig. 4.3 Geometry of the parallel-plate waveguide with an electrically large central layer and its parameters.

The optimizable parameters $\boldsymbol{p}^T = [\varepsilon_{r2}, \sigma_2, w]$ are the constitutive parameters of the central layer and its width. Figures 4.4 and 4.5 show the derivatives of $|S_{11}|$ with respect to σ_2 and ε_{r2}, respectively. It is observed that the results obtained using all coarse schemes except the one using $\Delta\chi = 20\Delta h$, which is close to the Nyquist limit at 5 GHz, show good agreement with the analytical, the FDTD-SASA and the CFD results.

For electrically large objects in a 1-D problem, if the optimizable parameters are material parameters, we recommend to choose the step size of the sensitivity solver as $\Delta\chi \le \lambda_{\min}/4$ in order to maintain good accuracy. Here, $\lambda_{\min}$ is the minimum wavelength of interest in the medium of the optimized object.

Figures 4.6a-b show the derivatives of the real and imaginary parts of S_{11} with respect to the shape parameter *w*, respectively. It is noted that results obtained using coarse grids except the one with $\Delta\chi = 2\Delta h$ show substantial discrepancies in comparison with the FDTD-SASA ($\Delta\chi = \Delta h$) as well as the FD curves. For 1-D problems, if the shape parameter is optimized, we recommend to choose the step size of the sensitivity solver equal to that of the simulation grid in order to maintain good accuracy. Also, the memory requirements in this case are small and there is no need to employ a coarse grid as means of reducing memory requirements.

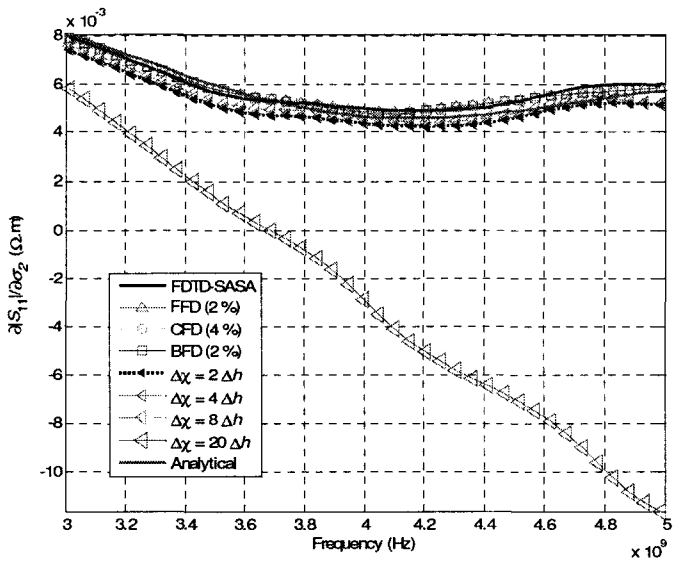

Fig. 4.4 Derivative of $|S_{11}|$ with respect to σ_2 in the 1-D example with an electrically large central layer.

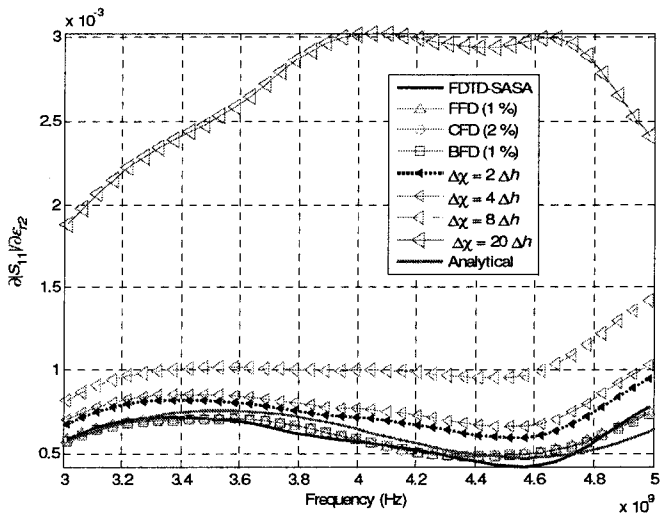

Fig. 4.5 Derivative of $|S_{11}|$ with respect to ε_{r2} in the 1-D example with an electrically large layer.

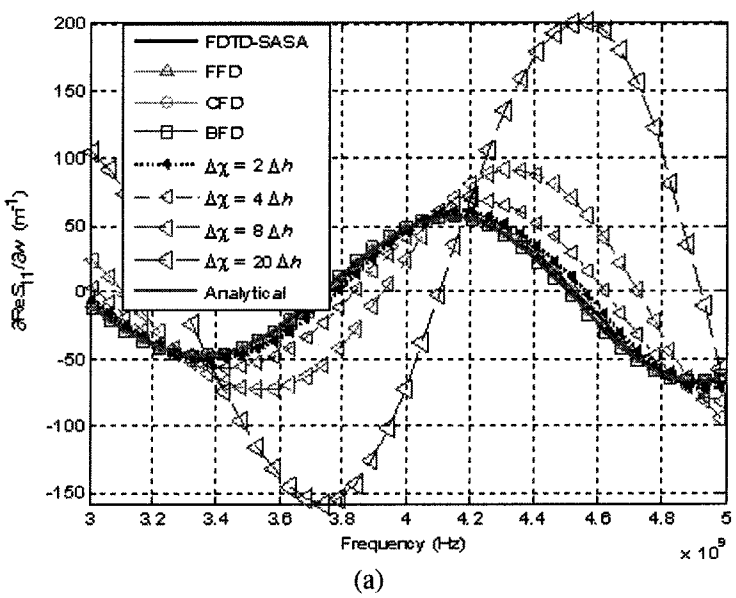

(a)

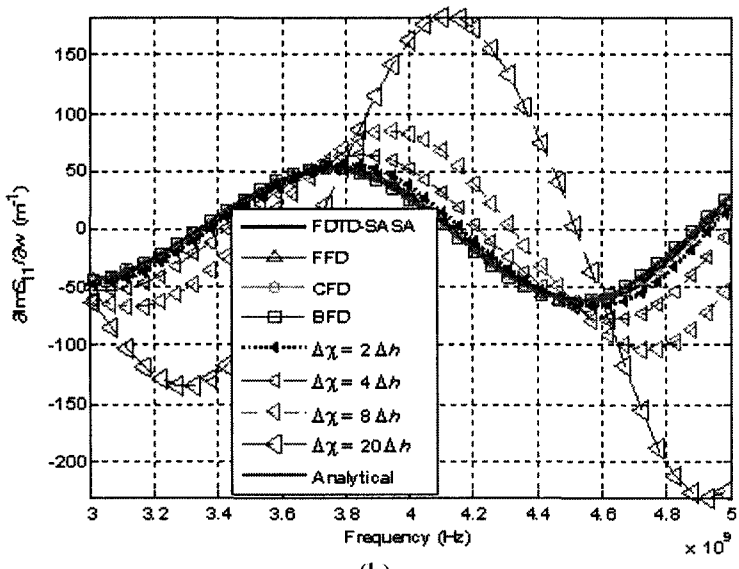

(b)

Fig. 4.6 Derivative of S_{11} with respect to w in the 1-D example with an electrically large layer: (a) derivative of $\mathrm{Re}(S_{11})$; (b) derivative of $\mathrm{Im}(S_{11})$.

B. Parallel-Plate Waveguide with an Electrically Small Middle Layer

A parallel-plate waveguide with an electrically small central layer and its parameters are shown in Figure 4.7. Uniform mesh ($\Delta h = 0.125$ mm) with a mesh convergence error less than 4 % is used in the FDTD simulation. The excitation and the optimizable parameters are the same as in the first example.

Figures 4.8a-b show the derivatives of the real and the imaginary parts of S_{21} with respect to σ_2, respectively. It is noted that all curves obtained using different coarse-grid schemes are in good agreement. There is very small discrepancy between

the curves obtained using coarse grids and all the other curves. We conclude that for an electrically small object in a 1-D problem, the step size $\Delta\chi$ of the sensitivity solver can be chosen as large as the size of the object when derivatives with respect to material parameters are computed.

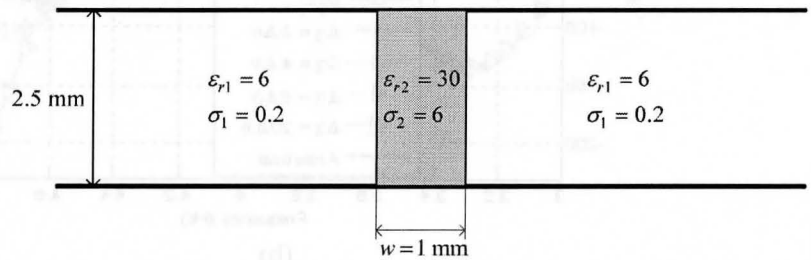

Fig. 4.7 Geometry of the parallel-plate waveguide with an electrically small central layer and its parameters.

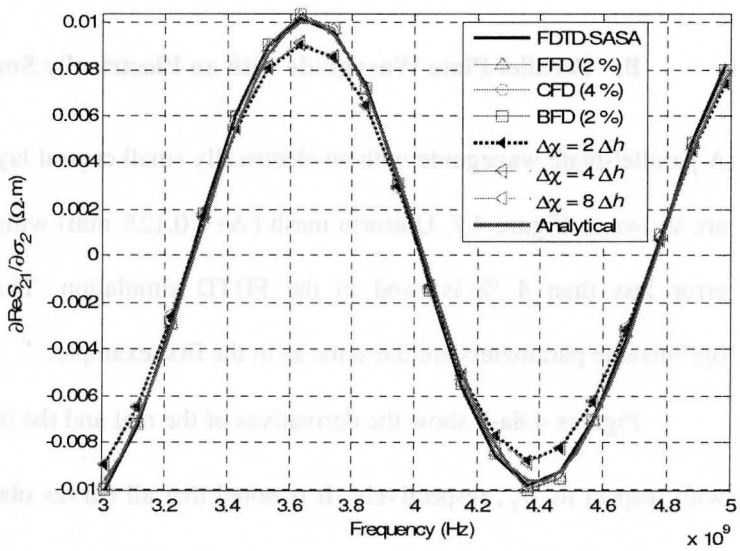

(a)

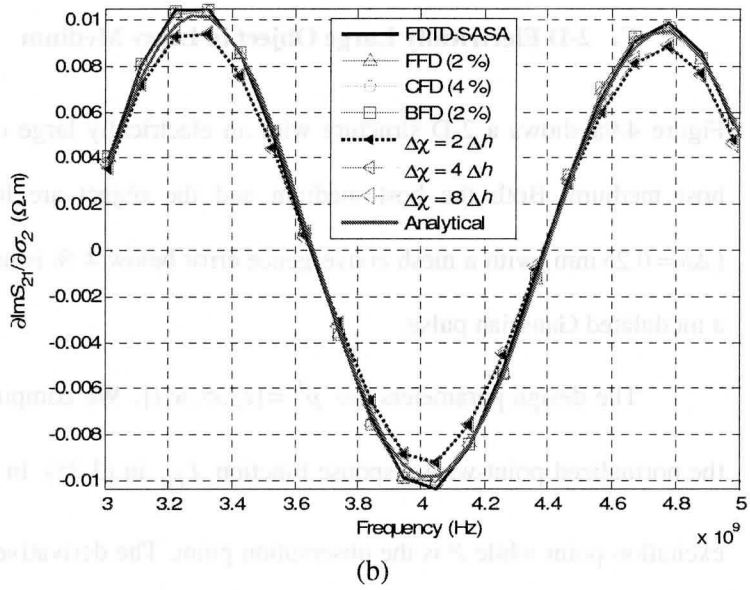

(b)

Fig. 4.8 Derivative of S_{21} with respect to σ_2 in the 1-D example with an electrically small layer: (a) derivative of $\mathrm{Re}(S_{21})$; (b) derivative of $\mathrm{Im}(S_{21})$.

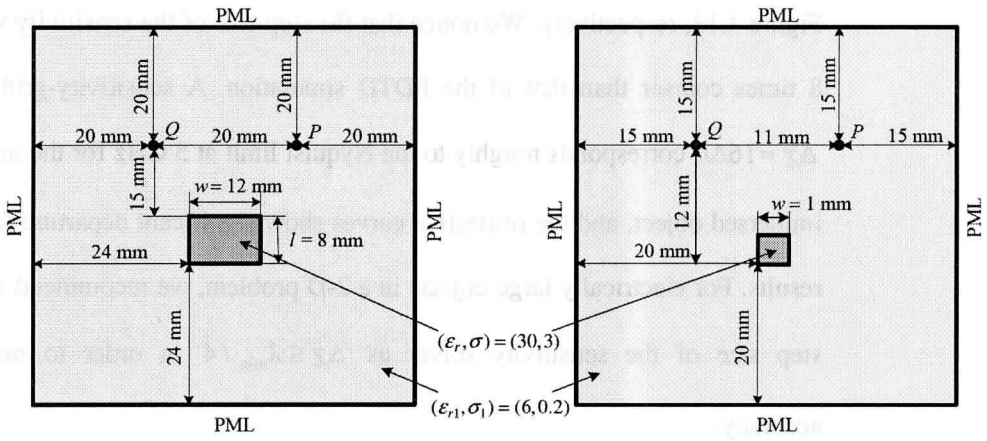

(a) (b)

Fig. 4.9 Geometry of the 2-D examples of objects in lossy medium and their parameters: (a) electrically large, and (b) electrically small.

C. 2-D Electrically Large Object in Lossy Medium

Figure 4.9a shows a 2-D structure with an electrically large object immersed in a host medium. Both the host medium and the object are lossy. Uniform mesh ($\Delta h = 0.25$ mm) with a mesh convergence error below 4 % is used. The excitation is a modulated Gaussian pulse.

The design parameters are $\boldsymbol{p}^T = [\varepsilon_r, \sigma, w, l]$. We compute the sensitivities of the normalized point-wise response function F_{PQ} in (3.25). In Figure 4.9a, Q is the excitation point while P is the observation point. The derivatives of $|F_{QQ}|$ and $|F_{PQ}|$ with respect to ε_r are shown in Figure 4.10 and Figure 4.11, respectively. The derivatives of $|F_{QQ}|$ and $|F_{PQ}|$ with respect to w are plotted in Figures 4.12 and Figure 4.13, respectively. We notice that the step size of the sensitivity solver can be 8 times coarser than that of the FDTD simulation. A sensitivity-grid cell size of $\Delta\chi = 16\Delta h$ corresponds roughly to the Nyquist limit at 5 GHz for the medium of the immersed object, and the respective curves show significant departure from all other results. For electrically large objects in a 2-D problem, we recommend to choose the step size of the sensitivity solver as $\Delta\chi \le \lambda_{\min}/4$ in order to maintain good accuracy.

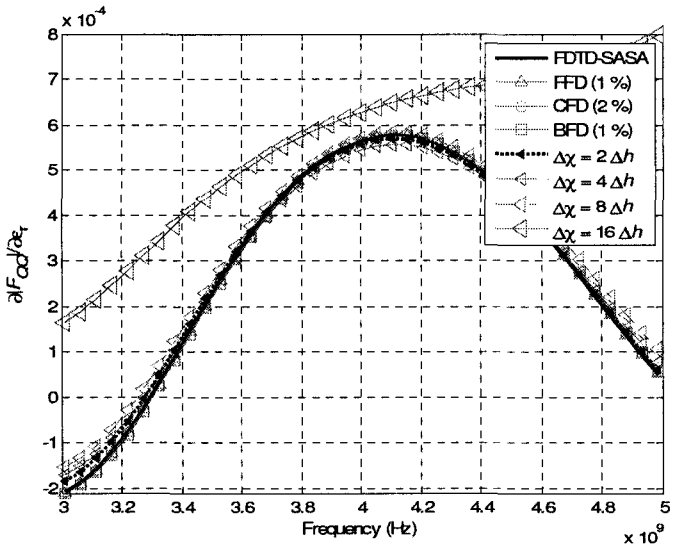

Fig. 4.10 Derivative of $|F_{QQ}|$ with respect to ε_r in the 2-D example with a large object.

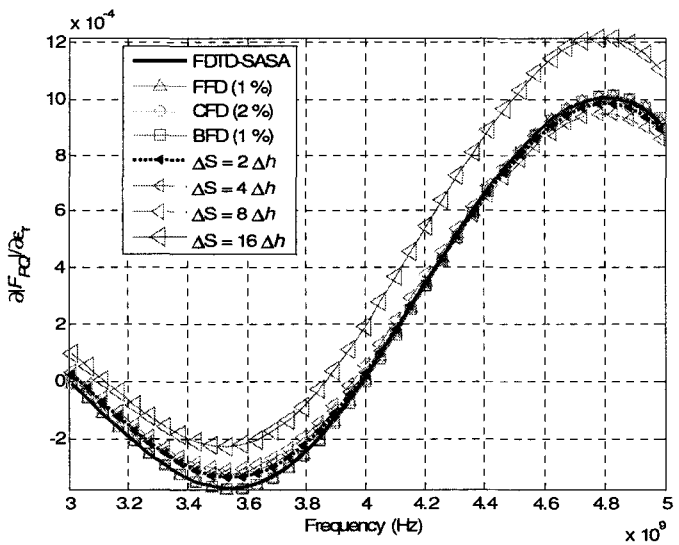

Fig. 4.11 Derivative of $|F_{PQ}|$ with respect to ε_r in the 2-D example with a large object.

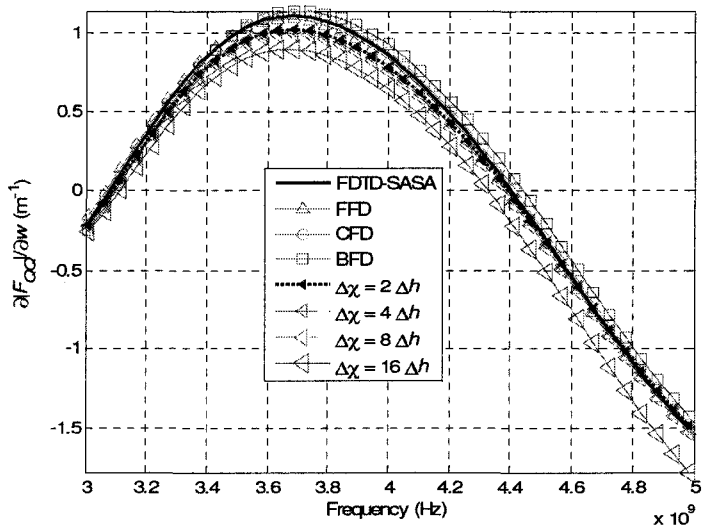

Fig. 4.12 Derivative of $|F_{QQ}|$ with respect to w in the 2-D example with a large object.

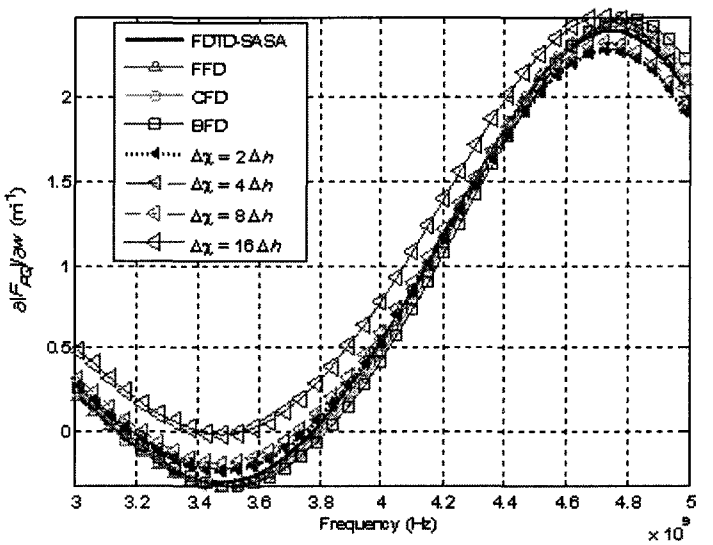

Fig. 4.13 Derivative of $|F_{PQ}|$ with respect to w in the 2-D example with a large object.

D. 2-D Electrically Small Object in Lossy Medium

Figure 4.9b shows a 2-D structure with an electrically small inhomogeneity in a host medium. Both the host medium and the inhomogeneity are lossy. A uniform mesh ($\Delta h = 0.125$ mm) with a mesh convergence error below 3 % is used. The excitation and the response functions are the same as those in the example in subsection *C*.

The design parameters are $\boldsymbol{p}^T = [\varepsilon_r, \sigma, w]$. In Figure 4.9b, Q is the excitation point while P is the observation point. The sensitivities of $|F_{PQ}|$ with respect to σ_2 and w are plotted in Figure 4.14 and Figure 4.15, respectively. The sensitivity of the imaginary part of F_{QQ} is plotted in Figure 4.16. We observe that the step size of the sensitivity solver needs to be the same as that of the FDTD simulation in order to achieve good accuracy. For electrically small objects in 2-D problems, we recommend to choose the step size of the sensitivity solver as that of the FDTD simulation for both shape and material parameters in order to maintain good accuracy.

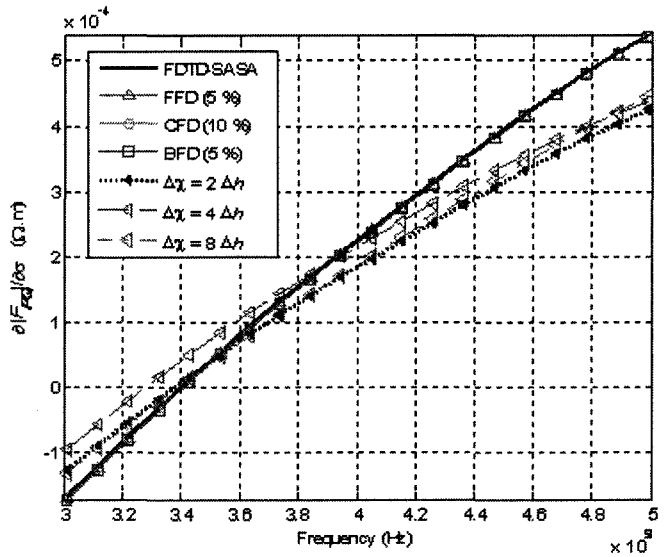

Fig. 4.14 Derivative of $|F_{PQ}|$ with respect to σ in the 2-D example with a small object.

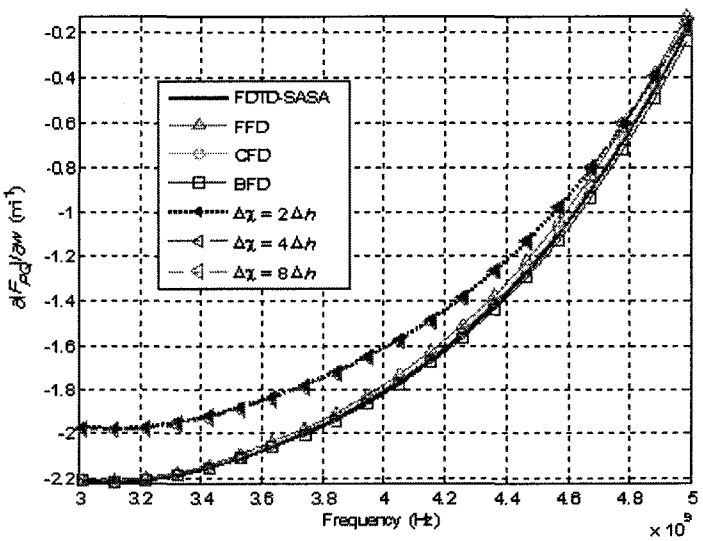

Fig. 4.15 Derivative of $|F_{PQ}|$ with respect to w in the 2-D example with a small object.

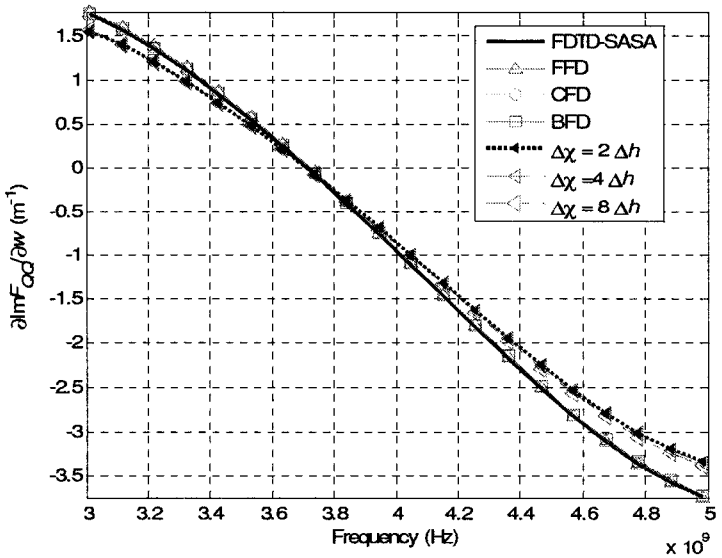

Fig. 4.16 Derivative of $\mathrm{Im}(F_{QQ})$ with respect to w in the 2-D example with a small object.

E. 3-D Object in Lossy Medium

Figure 4.17 shows a 2-D cross-section of the 3-D structure and its parameters. The host medium and the immersed object are lossy. The host medium is a rectangular box with a corner at (0, 0, 0) mm. It extends 40 mm along the x-axis and the z-axis, and 44 mm along the y-axis. The immersed object is a small rectangular object with a corner at (18, 15, 18) mm, and an extent of w = 4 mm along the x-axis, h = 4 mm along the y-axis and l = 4 mm along the z-axis. Uniform mesh ($\Delta h = 0.25$ mm) with a mesh convergence error below 5 % is used. Please note that the "Super Mur" is an absorbing boundary condition used in QW-3D [4].

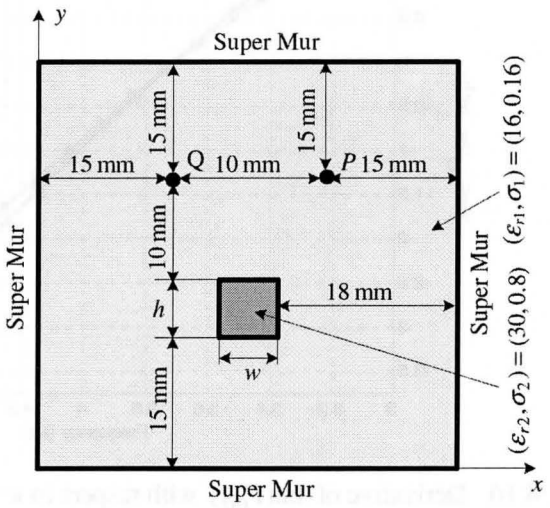

Fig. 4.17 A 2-D cross-section of the 3-D example and its parameters.

The design parameters are $\boldsymbol{p}^T = [\varepsilon_{r2}, \sigma_2, w, h, l]$. The excitation and the response functions are the same as those of the example in subsection *C*. In Figure 4.17, *Q* is the excitation point located at (15, 29, 17) mm while *P* is the observation point located at (25, 29, 17) mm. Figure 4.18 shows the derivative of $|F_{QQ}|^2$ with respect to *w*. It is noted that all curves obtained using coarse grids except the one with $\Delta\chi = 16\Delta h$, which approaches the Nyquist limit of the object medium at 5 GHz, have good agreement with the curves computed using our original self-adjoint approach. These curves are in close agreement, i.e., they are convergent. In contrast, the curves computed using response-level FDs are not convergent. Different shape

parameter perturbations have been tried. The best FD estimates are shown here obtained with $\Delta w = 2\Delta h$.

Figures 4.19 and 4.20 show the derivatives of $|F_{QQ}|^2$ and $|F_{PQ}|^2$ with respect to ε_{r2}, respectively. Similar results are obtained. All curves except the one with $\Delta\chi = 16\Delta h$ are in good agreement. We recommend that in a 3-D problem, the step size of the sensitivity solver is chosen as $\Delta\chi \le \lambda_{\min}/4$ for both material and shape parameters in order to maintain good accuracy.

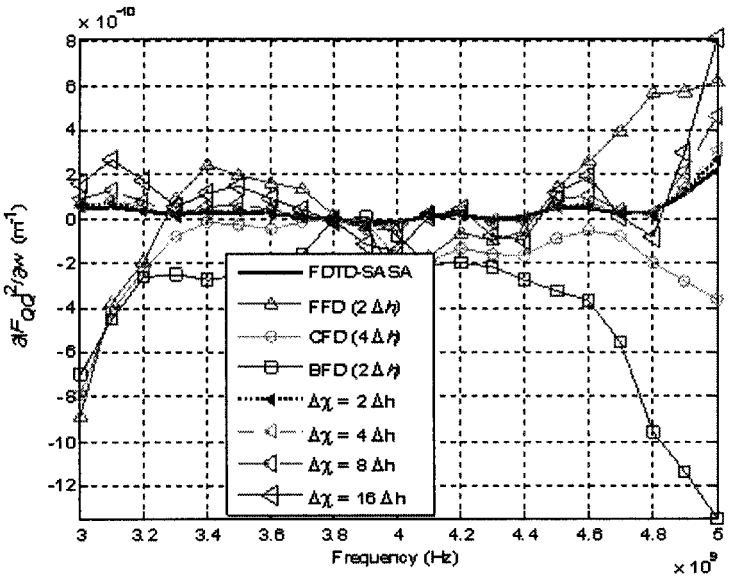

Fig. 4.18 Derivative of $|F_{QQ}|^2$ with respect to w in the 3-D example.

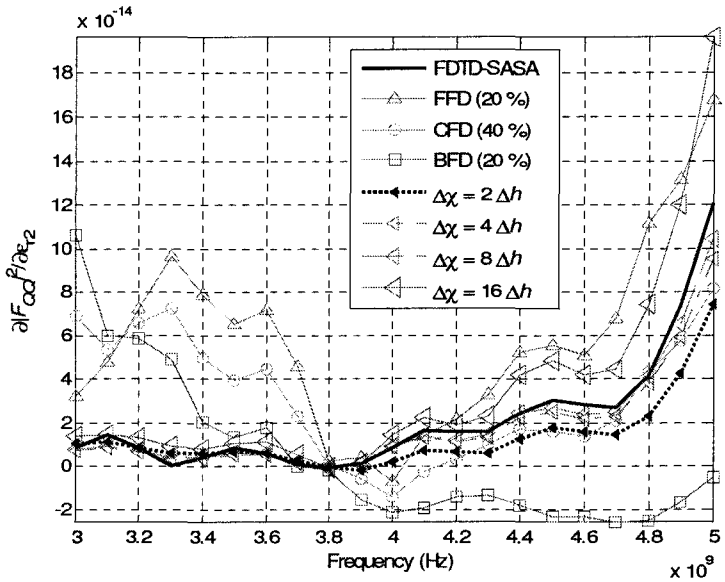

Fig. 4.19 Derivative of $|F_{QQ}|^2$ with respect to ε_{r2} in the 3-D example.

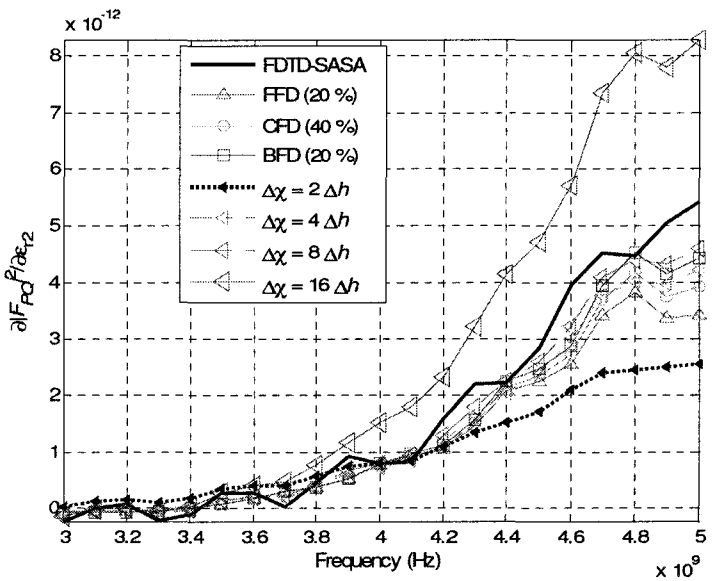

Fig. 4.20 Derivative of $|F_{PQ}|^2$ with respect to ε_{r2} in the 3-D example.

4.4 SUMMARY

We proposed a coarse-grid approach for the efficient computation of response Jacobians using the self-adjoint sensitivity analysis method. The grid of sensitivity solver can be many times coarser than that used by the EM simulation. The proposed technique reduces the memory requirements significantly. It is especially useful in the case of electrically large regions whose permittivity or conductivity distribution is being optimized, since the memory requirement of our original self-adjoint approach, which uses the FDTD simulation grid directly, may become excessive.

The coarse-grid approach is verified through a number of examples. We found that the sensitivity solver mesh size can be chosen as large as $\lambda_{\min}/4$ and still maintain good accuracy. Here, $\lambda_{\min}$ is the shortest wavelength of interest. Recommendations about the step size of the sensitivity solver grid are given for both electrically large and small objects. We emphasize that the accuracy of the sensitivity result is dependent on the accuracy of the field solution and, therefore, the grid of the EM simulation must remain fine enough to ensure convergent solution. Yet, the sensitivity grid can be as coarse as a quarter wavelength for the highest frequency of interest. This is because it is nothing more than a discrete means of calculating the sensitivity integral. It is limited only by the requirement that the local field solution is a sufficiently smooth function of space at the given frequency.

Our new grid scheme is independent of the simulation grid and is simple to

implement. The approach can be realized as standalone software to compute response Jacobians, which can be used in gradient-based computer-aided design and inverse-problem solutions. Applications focus on lossy dielectric media as those used to model high-frequency problems arising in biomedical applications of microwave imaging.

REFERENCES

[1] N. K. Nikolova, Ying Li, Yan Li, and M. H. Bakr, "Sensitivity analysis of scattering parameters with electromagnetic time-domain simulators," *IEEE Trans. Microwave Theory Tech.*, vol. 54, No. 4, pp. 1589–1610, April 2006.

[2] Y. Song, Ying Li, N. K. Nikolova, and M. H. Bakr, "Self-adjoint sensitivity analysis of lossy dielectric structures with electromagnetic time-domain simulators," *Int. J. of Numerical Modelling: Electronic Networks, Devices and Fields*, vol. 21, No. 1–2, pp. 117–132, Jan.–Apr. 2008.

[3] XFDTD v. 6.3, *Reference Manual*, Remcom, 2004, http://www.remcom.com/xfdtd.

[4] QuickWave-3D v. 6.0, *Reference Manual*, QWED, 2006, http://www.qwed.com.pl/index.html.

[5] Y. Song, N. K. Nikolova, and M. H. Bakr, "Efficient time-domain sensitivity analysis using coarse grids," *Applied Computational Electromagnetics Society Journal*, vol. 23, No. 1, pp. 5–15, Mar. 2008.

[6] A. Taflove and S. C. Hagness, *Computational Electromagnetics The Finite-Difference Time-Domain Method.* Artech House, INC, 2000.

Chapter 5

SELF-ADJOINT SENSITIVITIES WITH CENTRAL-NODE APPROACH

5.1 INTRODUCTION

Chapter 4 introduced an efficient coarse-grid approach for self-adjoint sensitivity analysis [1]. The use of coarse grids can reduce the memory requirements drastically and improve the computational efficiency of the sensitivity analysis while maintaining good accuracy. The target of the coarse-grid approach is the sensitivity analysis of electrically large objects or problems with a large number of optimizable parameters whose memory requirements may be excessive for the original self-adjoint approach.

In this Chapter, we introduce an important central-node approach for self-adjoint sensitivity analysis, which can be used to simplify the implementation of the sensitivity computation. It can also improve the accuracy of the sensitivity computation for dielectric structures.

In order to perform sensitivity analysis with respect to shape parameters using adjoint approaches, the field solutions at the perturbation grid points, which are

adjacent to the perturbation boundaries, are needed. On the other hand, the field solutions provided by time-domain solvers are the least accurate at dielectric interfaces. These interfaces are the places where some or all perturbation grid points reside. Therefore, the accuracy of sensitivity computation deteriorates when lossy inhomogeneous structures are considered. Moreover, the ambiguity in the way permittivity and conductivity are assigned at planar and edge interfaces complicates the sensitivity computation.

The central-node approach overcomes the above problems [2]. It uses an independent central-node FD grid, which departs from the conventional FDTD Yee-cell [3]. In the central-node FD grid, all three E-field components are co-located and at least half a grid step away from interface planes and edges. It is expected that the field solution accuracy is going to be better away from material interfaces regardless of what the discretization scheme is used in the FDTD simulations. In the examples studied here, the accuracy is visibly improved compared to our original adjoint approach for dielectric discontinuities. More importantly, the implementation is simplified, especially for 3-D problems, since the derivatives of the system coefficients are independent of any averaging scheme that the solver may use at material interfaces. The focus of the central-node approach is on 3-D lossy-dielectric structures

We start with a brief discussion on local accuracy of the field solutions at dielectric interfaces. Then, we describe the central-node approach for

inhomogeneous structures containing dielectric objects. We verify our approach through 1-D and 3-D examples implemented with commercial FDTD solvers, XFDTD [4] and QuickWave-3D [5].

5.2 LOCAL ACCURACY OF THE FIELD SOLUTIONS AT DIELECTRIC INTERFACES

As we discussed in Chapter 3, the local field solution at dielectric interfaces is needed for the adjoint sensitivity analysis of the shape parameters of dielectric objects. However, in simulation, these local field values are the least accurate due to the rapid change of the field in space, especially in the case of high permittivity and loss contrast. In this section, we illustrate the field errors at dielectric interfaces.

We define a mesh-convergence error at the ith sample point ($i = 1,...,N$) and the kth mesh-refinement iteration as

$$e = \max\{e_1^{(k)},...,e_N^{(k)}\} \tag{5.1}$$

where

$$e_i^{(k)} = \left|\tilde{E}_i^{(k+1)} - \tilde{E}_i^{(k)}\right| \Big/ \left|\tilde{E}_i^{(k+1)}\right| \tag{5.2}$$

Here, a sample point is defined not only by its position in the grid but also by the polarization of the monitored field component. The field phasors (denoted with a *tilde*) are obtained via Fourier transform. The error is monitored at multiple locations, frequencies and polarizations. It defines the margins of uncertainty of the numerical analysis. A mesh refinement factor of 2 is used at all frequencies of

interest in the following example. It is well known that the solution-convergence error is related not just to the grid cell size but also to other numerical factors such as the absorbing boundaries, the local mesh refinement, etc. Note that here we refer to the numerical error defined in (5.1) and (5.2), which is dependent on the grid cell size only, as the mesh-convergence error.

Figure 5.1 shows a 2-D structure with a square inhomogeneity in a host medium and their parameters. P_3 is the excitation point located at (11, 48) mm. The mesh convergence analysis is performed at three points P_1, P_2 and P_3. Here, P_1 and P_2 are located at (27, 30) mm and (30, 30) mm, respectively. All field values are obtained directly from a FDTD-based commercial solver XFDTD [4]. The respective error curves *versus* frequency are plotted in Figure 5.2. Here, $\Delta h^{(k)} = 0.25$ mm and $\Delta h^{(k+1)} = 0.125$ mm. We note that P_1, which is located at the interface, has the largest convergence errors at 3.3 GHz. The convergence errors *versus* step sizes are listed in Table I. The convergence errors at P_1, P_2 and P_3 are denoted using e_1, e_2 and e_3, respectively. We observe that the mesh convergence error at the interface in general is the largest for all step sizes.

TABLE 5.1
MESH CONVERGENCE ERRORS AT P_1, P_2 AND P_3 AT 3.3 GHZ

$\Delta h^{(k+1)}$ (mm)	e_1 (%)	e_2 (%)	e_3 (%)
0.5	360.3	13.5	6.7
0.25	178.5	6.6	3.7
0.125	58.1	10.5	2.1

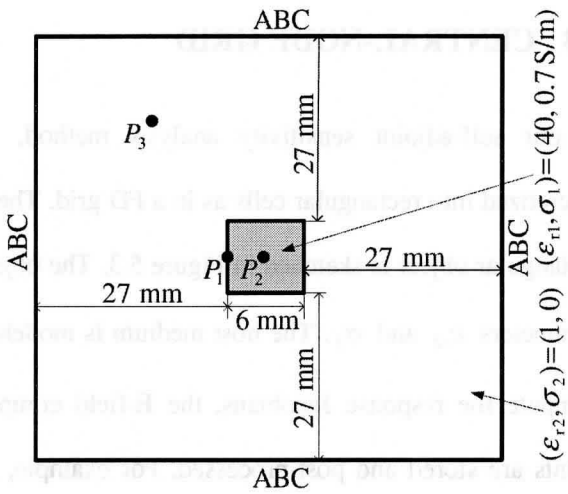

Fig. 5.1 Geometry of a 2-D structure used to illustrate the local accuracy of the field solution at a dielectric interface.

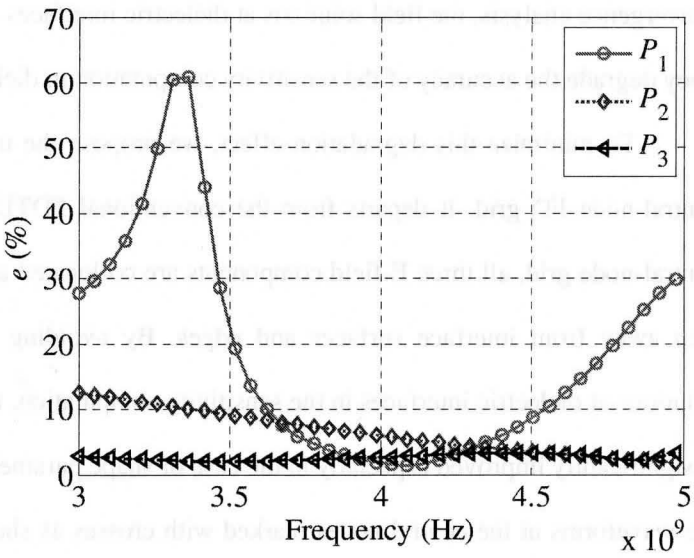

Fig. 5.2 Mesh convergence error vs. frequency at $\Delta h^{(k+1)} = 0.125$ mm.

5.3 CENTRAL-NODE GRID

In our self-adjoint sensitivity analysis method, the computational domain is discretized into rectangular cells as in a FD grid. The 2-D FD grid cross-section of a rectangular object is sketched in Figure 5.3. The object is modeled with constitutive parameters ε_{r2} and σ_2. The host medium is modeled with ε_{r1} and σ_1. In order to compute the response Jacobians, the **E**-field components at all perturbation grid points are stored and post-processed. For example, if the response derivative with respect to w is computed and if the object is dielectric, the field solutions are needed at all nodes marked with dots in Figure 5.3. It is noted that some of the perturbation grid points are located at the interface. As we discussed in Section 5.2 through mesh convergence analysis, the field solutions at dielectric interfaces are the least accurate. They degrade the accuracy of the sensitivity computation in dielectric structures.

To minimize this degradation effect, we propose the use of an independent central-node FD grid. It departs from the conventional FDTD Yee-cell [3]. In the central-node grid, all three **E**-field components are co-located and at least half a grid step away from interface surfaces and edges. By avoiding the use of the field solutions at dielectric interfaces in the sensitivity computation, the Jacobian accuracy is significantly improved especially in the case of shape parameters. In this approach, the waveforms at the central nodes marked with crosses as shown in Figure 5.3 are sampled and used in the sensitivity computation.

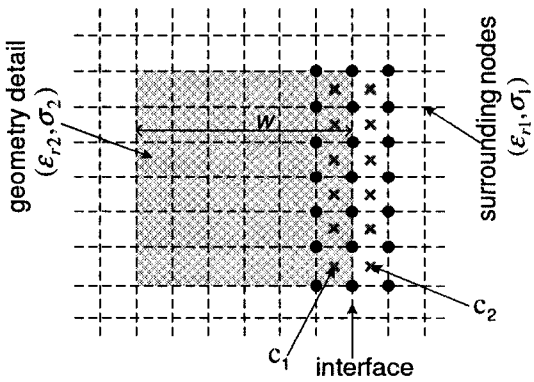

Fig. 5.3 2-D cross-section of a rectangular object and its sensitivity-solver grids for the shape parameter w: points — original approach; crosses — central-node approach.

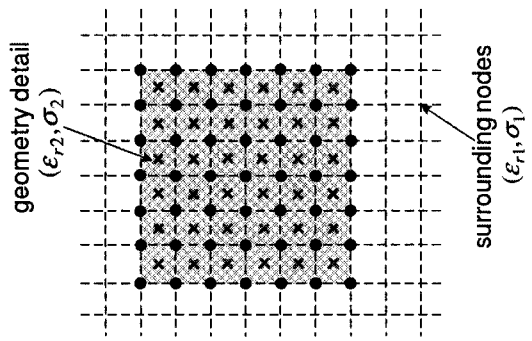

Fig. 5.4 2-D cross-section of a rectangular object and its sensitivity-solver grids for material parameters: points — original approach; crosses — central-node approach.

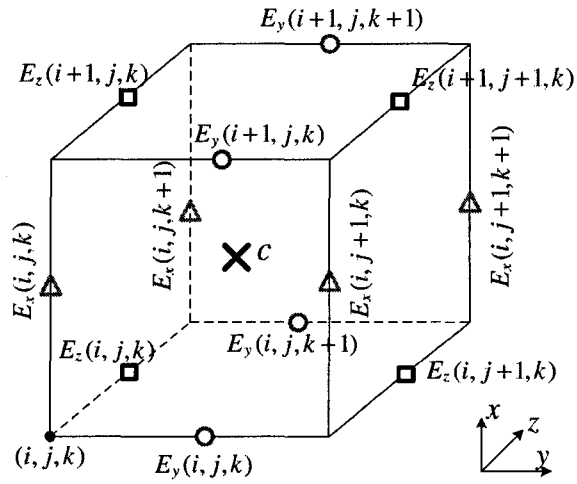

Fig. 5.5 One Yee cell and the corresponding central node c (marked with a cross).

The central-node approach can be applied to constitutive parameters in the same manner. The dots in Figure 5.4 are the perturbation grid points in our original approach, while the nodes marked with crosses are the perturbation grid points in our central-node approach in the case of sensitivities with respect to the object's permittivity and conductivity.

With FDTD solvers, the **E**-field is computed at the edges of the Yee cell [3]. To obtain the field at the central nodes, we use simple averaging of the values at the surrounding nodes, which coincide with the nodes of the Yee grid. Figure 5.5 illustrates one Yee cell and the corresponding central node c. Notice that the central nodes are always half a step away from interface planes and edges. At such points the nodal permittivity and conductivity are well defined and so are their changes

resulting from a discrete perturbation of the shape. The three **E**-field components at a central node are computed using simple averaging. For example, the three **E**-field components at c are

$$\bar{E}_x(i,j,k) = \frac{1}{4} \cdot \left[E_x(i,j,k) + E_x(i,j,k+1) + E_x(i,j+1,k+1) + E_x(i,j+1,k) \right] \quad (5.3)$$

$$\bar{E}_y(i,j,k) = \frac{1}{4} \cdot \left[E_y(i,j,k) + E_y(i+1,j,k) + E_y(i+1,j,k+1) + E_y(i,j,k+1) \right] \quad (5.4)$$

$$\bar{E}_z(i,j,k) = \frac{1}{4} \cdot \left[E_z(i,j,k) + E_z(i+1,j,k) + E_z(i+1,j+1,k) + E_z(i,j+1,k) \right]. \quad (5.5)$$

We emphasize that our sensitivity algorithm operates on its own independent structured grid, which may be several times coarser than that of the simulator as discussed in Chapter 4. We denote the ratio of the cell size of the sensitivity-solver grid to the simulator's cell size as k. Figures 5.3 to 5.5 and formulas (5.3)-(5.5) describe the method of transferring the solution of a FDTD-based solver onto the central-node grid in the case when $k = 1$. This method is based on a simple linear interpolation of the available field solution at points, which are equidistant from the central node. When $k > 1$, the points at which the field is available are not necessarily equidistant from the central node. In this case, general linear interpolation is used.

5.4 NUMERICAL EXAMPLES

We illustrate the proposed approach through 1-D and 3-D lossy dielectric inhomogeneous examples with FDTD-based commercial solvers [4]-[5]. We compute the derivatives of *S*-parameters and the point-wise response function defined in (3.25) with respect to both constitutive and shape parameters.

In all plots, the results obtained using the central-node self-adjoint sensitivity analysis are marked as CN-SASA. The results obtained using the original self-adjoint sensitivity analysis are marked as SASA. The results obtained using the forward, central and backward finite differences at the response level are marked as FFD, CFD and BFD, respectively. The FD estimates use parameter perturbation of $1\Delta h$ for shape-parameter derivatives. Wherever available, analytical results are marked as 'Analytical'. All analyses are performed over a frequency range from 3.0 GHz to 5.0 GHz.

A. Parallel-Plate Waveguide

We first illustrate the approach through a 1-D inhomogeneous parallel-plate waveguide which has analytical solution. The structure and its parameters are shown in Figure 5.6. Uniform mesh ($\Delta h = 0.25$ mm) is used. The structure is excited with a modulated Gaussian pulse, which has a uniform distribution across the port conforming to a TEM plane wave.

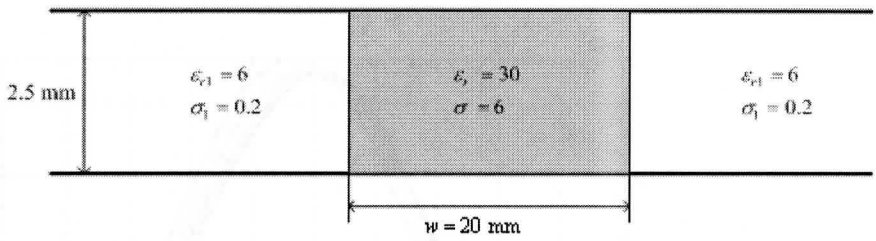

Fig. 5.6 Geometry of the parallel-plate waveguide and its parameters.

The optimizable parameters are $\boldsymbol{p}^T = [\varepsilon_r, \sigma, w]$, which are the constitutive and shape parameters of the central layer. The derivatives of the real and the imaginary parts of S_{11} with respect to ε_r are shown in Figure 5.7 and Figure 5.8, respectively. The derivatives of the real and the imaginary parts of S_{11} with respect to σ are shown in Figure 5.9 and Figure 5.10, respectively. We observe that the results obtained using our central-node self-adjoint approach agree best with the analytical results as compared to all other results. Here, central FD estimates use 2 % parameter perturbation of the nominal values of the constitutive parameters.

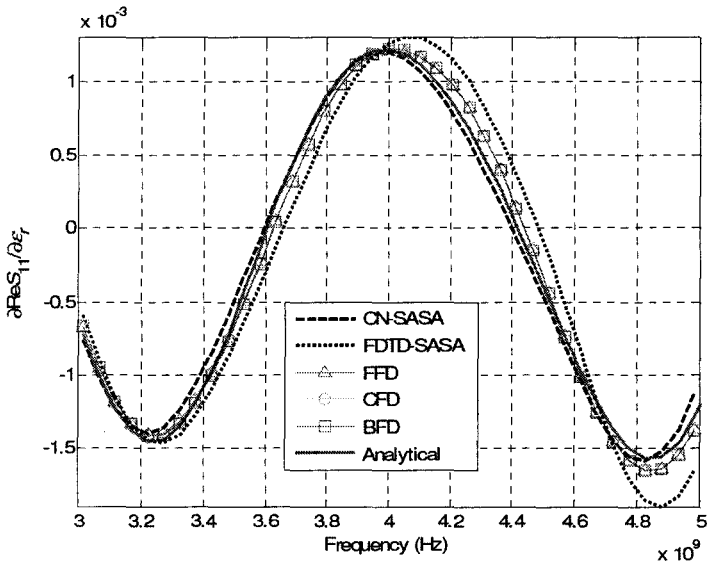

Fig. 5.7 Derivative of $\mathrm{Re}(S_{11})$ with respect to ε_r.

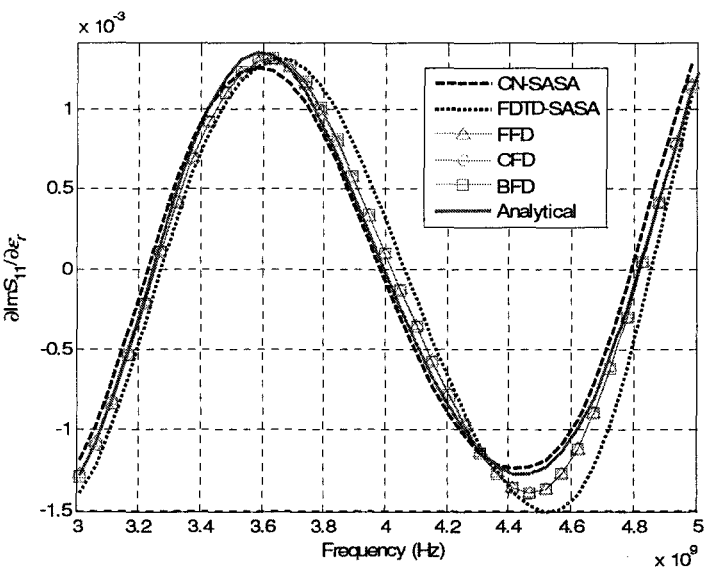

Fig. 5.8 Derivative of $\mathrm{Im}(S_{11})$ with respect to ε_r.

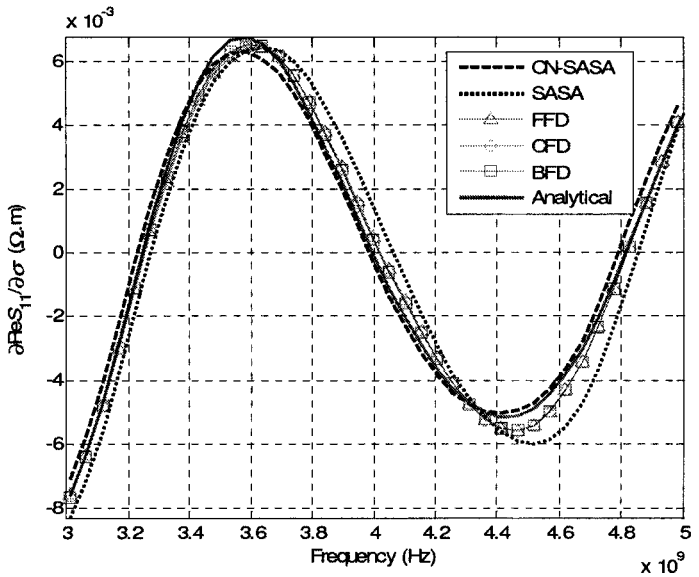

Fig. 5.9 Derivative of $\mathrm{Re}(S_{11})$ with respect to σ.

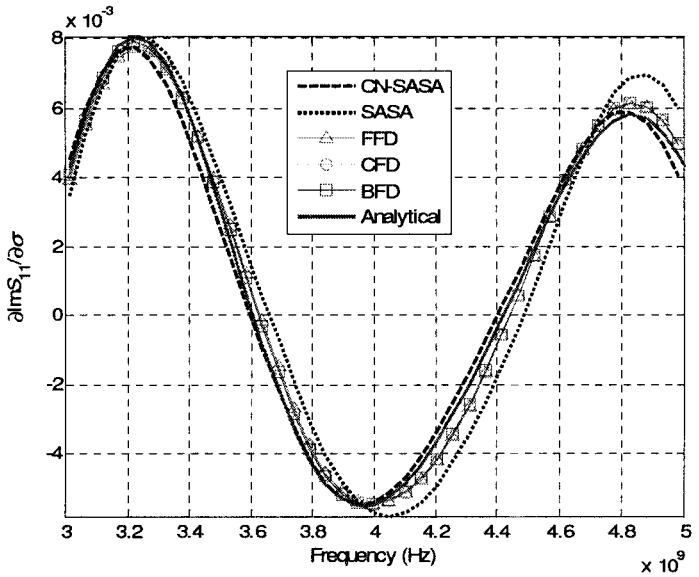

Fig. 5.10 Derivative of $\mathrm{Im}(S_{11})$ with respect to σ.

In 1-D problems, the accuracy improvement due to the central-node approach, although noticeable, is not usually significant. In general, the improvement is more significant in 2-D and 3-D problems. This is illustrated in our next 3-D example.

B. Object in Lossy Medium

Figure 5.11 shows a 2-D cross-section of the 3-D structure and its parameters. Both the host medium and the immersed object are lossy. The host medium is a rectangular box with a corner at (0, 0, 0) mm. It extends 30 mm along the x-axis, 34 mm along the y-axis and 30 mm along the z-axis. The immersed object is a small rectangular box with a corner at (13, 10, 13) mm, and an extent of w = 4 mm (x-axis), h = 4 mm (y-axis) and l = 4 mm (z-axis). Uniform mesh ($\Delta h = 0.25$ mm) is used. The excitation is a modulated Gaussian pulse.

The optimizable parameters are $\boldsymbol{p}^T = [w, h, l, \varepsilon_{r2}, \sigma_2]$. They describe the shape and the constitutive parameters of the immersed object. The normalized point-wise response function F_{PQ} in (3.25) is used. In Figure 5.11, Q is the excitation point located at (10, 24, 15) mm while P is the observation point located at (20, 24, 15) mm. The derivatives of the real part, the imaginary part and the magnitude of F_{QQ} with respect to w are plotted in Figures 5.12a-c, respectively. The derivatives of the real part, the imaginary part and the magnitude of F_{PQ} with respect to w are shown

in Figures 5.13a-c, respectively. It is observed that the results obtained using the central-node approach are in better agreement with the CFD results than those obtained with the original staggered-grid approach.

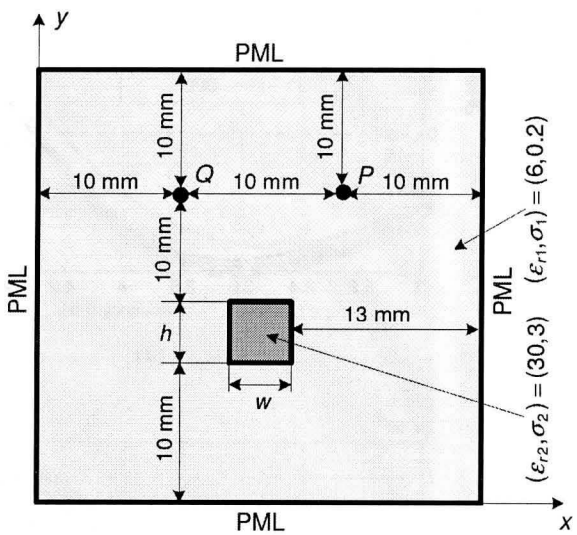

Fig. 5.11 A 2-D cross-sectional view of the geometry of the 3-D example and its parameters.

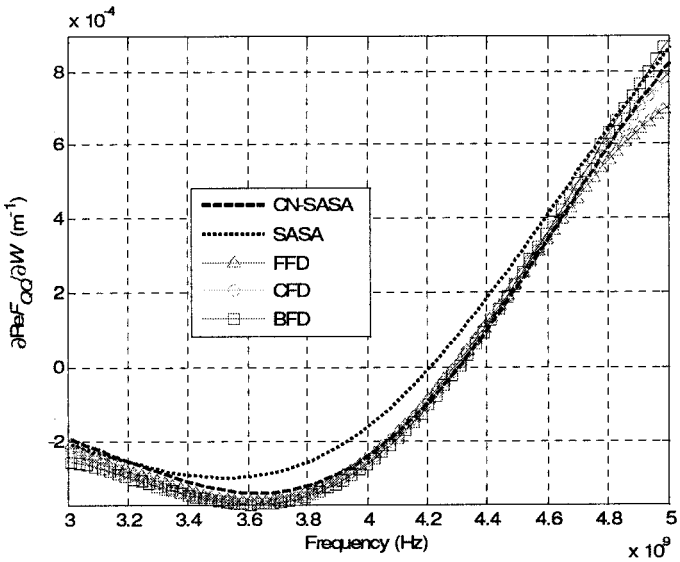
x 10^-4
8
6
4
2
0
-2
3
3.2
3.4
3.6
3.8
4
4.2
4.4
4.6
4.8
5
x 10^9
Frequency (Hz)
∂ReF_QO/∂W (m^-1)
CN-SASA
SASA
FFD
CFD
BFD

(a)

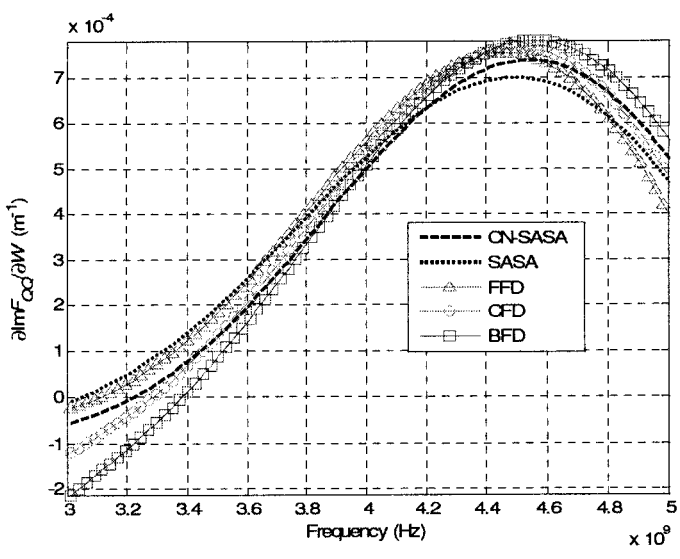
x 10^-4
7
6
5
4
3
2
1
0
-1
-2
3
3.2
3.4
3.6
3.8
4
4.2
4.4
4.6
4.8
5
x 10^9
Frequency (Hz)
∂ImF_QO/∂W (m^-1)
CN-SASA
SASA
FFD
CFD
BFD

(b)

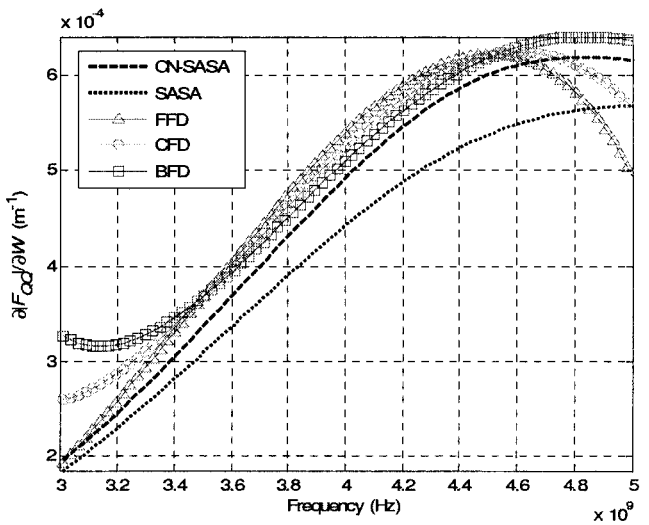

(c)

Fig. 5.12 Derivatives of F_{QQ} with respect to w in the 3-D example: (a) derivative of $\mathrm{Re}(F_{QQ})$; (b) derivative of $\mathrm{Im}(F_{QQ})$; (c) derivative of $|F_{QQ}|$.

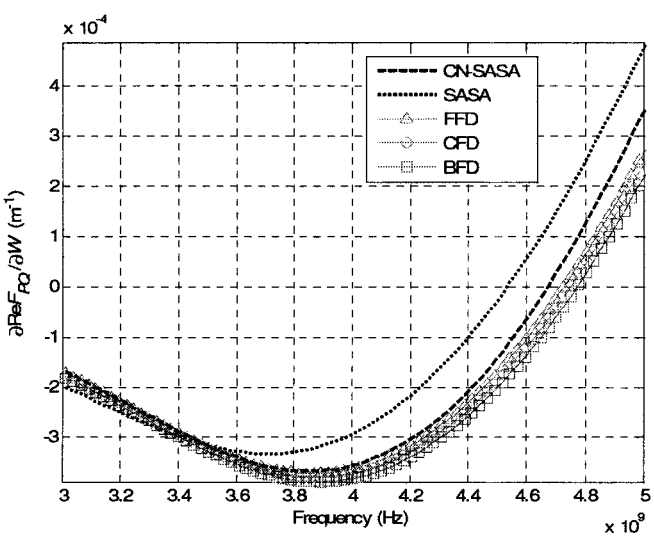

(a)

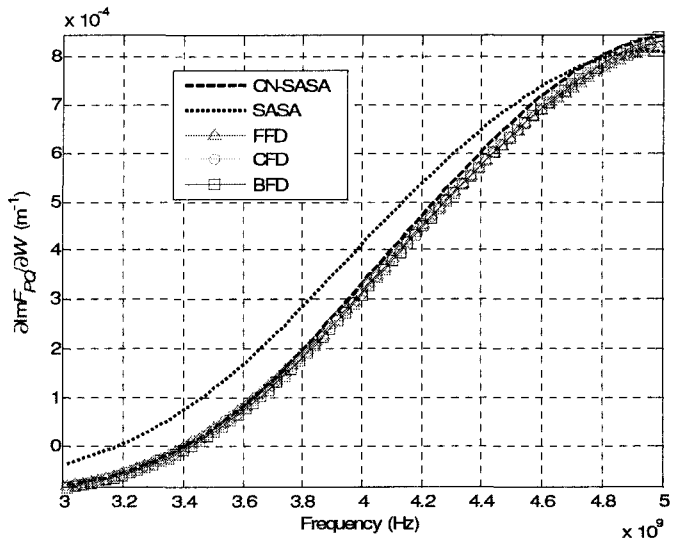

(b)

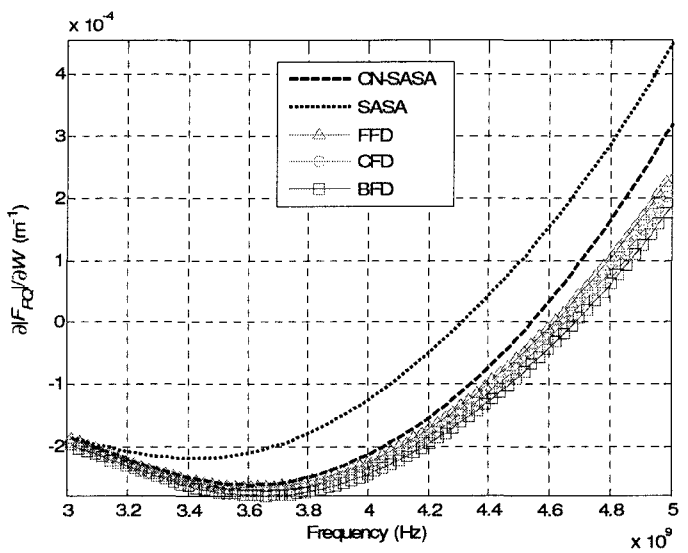

(c)

Fig. 5.13 Derivatives of F_{PQ} with respect to w in the 3-D example: (a) derivative of $\mathrm{Re}(F_{PQ})$; (b) derivative of $\mathrm{Im}(F_{PQ})$; (c) derivative of $\left|F_{PQ}\right|$.

5.5 SUMMARY

In this Chapter, we proposed a central-node approach for accurate computation of response sensitivities with self-adjoint sensitivity analysis technique using time-domain field solutions. The proposed technique is an important improvement to the self-adjoint sensitivity analysis method introduced in Chapter 3. The accuracy of the central-node approach is better than that of our original approach in the case of dielectric structures, while the efficiency remains the same.

The central-node approach uses an independent central-node FD grid where all three **E**-field components are co-located and at least half a grid step away from interfaces. The accuracy improvement is due to a shift in the position of the perturbation grid points, which places them at least one-half step away from the faces and the edges of dielectric interfaces where the field solutions are least accurate. The local accuracy of the field solutions at dielectric interfaces was discussed in Section 5.2.

The proposed technique was verified through 1-D and 3-D examples. It is observed that the accuracy of the central-node approach is superior to the original approach in the case of lossy dielectric structures. Besides its excellent accuracy, the implementation in 3-D structures is much simplified by using the central-node approach in comparison with the original approach. Applications focus on 3-D lossy

dielectric structures arising in biomedical applications of microwave imaging. The central-node approach can also be applied to metallic structures.

REFERENCES

[1] Y. Song, N. K. Nikolova, and M. H. Bakr, "Efficient time-domain sensitivity analysis using coarse grids," *Applied Computational Electromagnetics Society Journal*, vol. 23, No. 1, pp. 5–15, Mar. 2008.

[2] Y. Song and N. K. Nikolova, "Central-node approach for accurate self-adjoint sensitivity analysis of dielectric structures," *IEEE MTT-S Int. Microwave Symposium*, June 2007, pp. 895–898.

[3] A. Taflove and S. C. Hagness, *Computational Electromagnetics The Finite-Difference Time-Domain Method.* Artech House, INC, 2000.

[4] XFDTD v. 6.3, *Reference Manual*, Remcom, 2004, http://www.remcom.com/xfdtd.

[5] QuickWave-3D v. 6.0, *Reference Manual*, QWED, 2006, http://www.qwed.com.pl/index.html.

Chapter 6

SPECTRAL METHOD FOR WIDEBAND SELF-ADJOINT SENSITIVITIES

6.1 INTRODUCTION

So far, we have introduced our time-domain self-adjoint sensitivity analysis method for the computation of response Jacobians. Our method features several advantages: (i) it is applicable with commercial time-domain EM solvers since its only requirement is to access the **E**-field at user defined locations; (ii) it has superior accuracy over any response-level derivative approximations; (iii) its computational overhead is negligible in comparison with the time required by the EM simulation even if the number of the optimizable parameters N is in the order of thousands.

The time-domain self-adjoint sensitivity analysis method is intrinsically wideband since it operates on time-domain field waveforms. However, the memory requirements of the method may become a serious problem when N is very large and the simulation time is long. This is typical in microwave imaging where the imaged volume represents a considerable portion of the computational volume, i.e., the number of the grid points where the field waveforms are recorded is very large. In

this case, the memory requirements may easily reach hundreds of gigabytes, which is unmanageable for most computers.

To overcome the above problem, we propose a new sensitivity solver developed for time-domain analysis engines [5]. The proposed sensitivity solver is based on a spectral formula for the self-adjoint computation of the Jacobians. The new sensitivity formula operates on the spectral components of the **E**-field at the desired frequencies rather than on its time waveforms. The wideband nature of the time-domain analysis is preserved but the response sensitivities can be computed at select frequency points. The number of these frequency points N_f can be much smaller than the number of time-domain samples N_t in a recorded waveform. We now record only $3\times N_f$ complex numbers instead of recording $3\times N_t$ real numbers at each perturbation grid point. Note that the discrete Fourier transform needed to compute the field phasors is carried out "on-the-fly" and has negligible memory requirements. Thus, the memory requirements of the spectral approach are independent of the simulation time and are reduced by a factor of $N_t/(2N_f)$ as compared to the original time-domain approach. As a typical example, $N_t = 20000$ and $N_f = 10$, which results in a memory saving factor of 1000, thus reducing the memory from gigabytes to megabytes and making applications feasible. Beside its memory efficiency, the new approach retains all advantages of time-domain self-adjoint sensitivity analysis method discussed above.

Further, the proposed approach improves significantly the accuracy of the Jacobians by using a central-node grid as discussed in Chapter 5, where all three **E**-field components are co-located [4].

The proposed technique is well suited for wideband response Jacobian computation both in microwave imaging and in design. With a single time-domain analysis performed with any available simulation tool, high fidelity responses and Jacobians are obtained. The field phasors are recorded instead of the respective time waveforms and the length of the time-domain simulation is no longer a factor in the memory requirements.

We start with the derivation of the spectral sensitivity formula. We then verify the proposed spectral approach through 1-D and 3-D examples. We also show Jacobian distribution maps in a 3-D imaging problem. The memory and time requirements are discussed in Section 6.4. In all examples, field analyses are carried out with the commercial time-domain FDTD based solver QW-3D [6].

6.2 SPECTRAL SELF-ADJOINT SENSITIVITY FORMULA

The self-adjoint sensitivity formulas (3.1), (3.4), (3.23) and (3.24) introduced in Chapter 3 operate on the time waveforms of the **E**-field [1]-[2]. The sensitivities of any frequency-domain response, which is defined as a complex phasor $\tilde{F}$, can be

computed similarly to the *S*-parameter sensitivity (3.11). Here, we derive a new self-adjoint sensitivity formula for Jacobian computation of $\tilde{F}$. The proposed technique operates on the spectral components of the field solution at the frequencies of interest instead of its time waveforms. The development of the new spectral formula is carried out in detail based on the exact self-adjoint formula (3.4) in the case of constitutive parameters [5]. The derivation of the spectral counterpart for shape parameters is analogous.

We rewrite the self-adjoint sensitivity formula (3.4) for constitutive parameters as follows

$$\left(\frac{\partial \tilde{F}}{\partial p_n}\right)_{R,I} \approx -\int_0^{T_{\max}} \iiint_{\Omega} (\hat{\mathbf{E}})_{R,I} \cdot \frac{\partial R(\mathbf{E})}{\partial p_n} d\Omega dt, \qquad n = 1,...,N \tag{6.1}$$

Here, $\tilde{F}$ is the complex phasor at the frequency ω_0; p_n denotes the nth optimizable parameter; the subscripts R and I denote the real and the imaginary parts of a complex quantity, respectively; $T_{\max}$ is the simulation time; Ω is the computational volume; $\mathbf{E}$ is the time-dependent original field solution of the nominal structure; $(\hat{\mathbf{E}})_{R,I}$ are the time-dependant adjoint field solutions in the unperturbed state. Since perturbations in the constitutive parameters affect only the system coefficients α and s, $\partial R(\mathbf{E})/\partial p_n$ is computed as

$$\frac{\partial R(\bar{\mathbf{E}})}{\partial p_n} = -\frac{\partial \alpha}{\partial p_n} \cdot D_{t1}\bar{\mathbf{E}} - \frac{\partial s}{\partial p_n} \cdot D_{t2}\bar{\mathbf{E}} \tag{6.2}$$

where

$$\frac{\partial \alpha}{\partial p_n} = \begin{cases} \left(\frac{\Delta h}{c\Delta t}\right)^2, & p_n = \varepsilon_r \\ 0, & p_n = \sigma \end{cases} \tag{6.3}$$

and

$$\frac{\partial s}{\partial p_n} = \begin{cases} 0, & p_n = \varepsilon_r \\ \frac{\mu_0 \Delta h^2}{2\Delta t}, & p_n = \sigma. \end{cases} \tag{6.4}$$

Here, the operators D_{tt}, D_{t2} and D_t are second- and first-order finite difference operators with respect to time; Δh is a spatial step and Δt is a temporal step; c is the speed of light in vacuum, ε_r is the relative permittivity, μ_0 is the vacuum permeability and σ is the specific conductivity.

In the case of the S_{pq}-parameter derivative, the derivative of the complex response $\tilde{F} = \tilde{F}_{pq}$(3.9), $\partial \tilde{F}_{pq} / \partial p_n$, is needed. Discretizing (6.1) in space, the derivative of the real part of $\tilde{F}_{pq}$ with respect to p_n ($n = 1,...,N$) is calculated as

$$\left(\frac{\partial \tilde{F}_{pq}}{\partial p_n}\right)_R = -\int_0^{T_{\max}} \sum_{Q \in \Omega} (\hat{\mathbf{E}}_p(Q,t))_R \cdot \frac{\partial R\left(\mathbf{E}_q(Q,t)\right)}{\partial p_n} \cdot \Delta\Omega_Q dt. \tag{6.5}$$

Here, $(\hat{\mathbf{E}}_p(Q,t))_R$ denotes the associated adjoint-field solution at point Q and time t when port p is excited; $\mathbf{E}_q(Q,t)$ is the original field solution when port q is excited. $\Delta\Omega_Q$ is the cell volume related to the perturbation grid point Q. The expression for

the imaginary part of $\tilde{F}_{pq}$ is analogous with the only difference in the phase of the adjoint field $(\hat{\mathbf{E}}_p(Q,t))_I$, which is 90° larger than that of $(\hat{\mathbf{E}}_p(Q,t))_R$.

We rewrite (6.5) in a compact form as

$$\left(\frac{\partial \tilde{F}_{pq}}{\partial p_n}\right)_R = -\sum_{Q\in\Omega}\left(\mathcal{J}_R^{pq}\right)_Q \Delta\Omega_Q, \quad n=1,...,N \tag{6.6}$$

where

$$\left(\mathcal{J}_R^{pq}\right)_Q = \int_0^{T_{\max}} (\hat{\mathbf{E}}_p(Q,t))_R \cdot \left.\frac{\partial R(\mathbf{E}_q)}{\partial p_n}\right|_{(Q,t)} \cdot dt. \tag{6.7}$$

Here, the adjoint field $(\hat{\mathbf{E}}_p(Q,t))_R$ is derived from the ω_0 spectral component of the original field $\tilde{\mathbf{E}}_p(Q) = \sum_{\zeta=x,y,z}\hat{\zeta}\,|E_{\zeta p}(Q)|\cdot\exp[j\varphi_{e\zeta p}(Q)]$ as [1] (see also 3.23)

$$(\hat{E}_{\zeta p}(Q,t))_R = \frac{|E_{\zeta p}(Q)|}{a}\cdot\sin\left(\omega_0 t + \varphi_g - \varphi_{e\zeta p}(Q)\right) \tag{6.8}$$

where

$$a = J_p G_m \omega_0 \beta \Delta t \Delta z_p \tag{6.9}$$

and $\zeta = x, y, z$ denotes the respective vector component. $|E_{\zeta p}(Q)|$ and $\varphi_{e\zeta p}(Q)$ are the magnitude and phase of $\tilde{E}_{\zeta p}(Q)$, which is obtained from $E_{\zeta p}(Q,t)$ via Fourier transform; G_m and φ_g are the magnitude and phase of the original excitation pulse at frequency ω_0; Δz_p is the longitudinal cell size at port p, and J_p (usually set to 1) is the scaling factor used to account for the actual strength of the source.

Substituting (6.8) into (6.7), we obtain

$$\left(\mathcal{G}_R^{pq}\right)_Q = \sum_{\zeta=x,y,z} \frac{|E_{\zeta p}(Q)|}{a}\hat{\boldsymbol{\zeta}} \cdot \int_0^{T_{\max}} \left.\frac{\partial R(\mathbf{E}_q)}{\partial p_n}\right|_{(Q,t)} \sin[\phi_{\zeta p}(Q,t)]dt \qquad (6.10)$$

where we have used the short-hand notation $\phi_{\zeta p}(Q,t) = \omega_0 t + \varphi_g - \varphi_{e\zeta p}(Q)$.

Analogously, the derivative of the imaginary part of $\tilde{F}_{pq}$ is computed as

$$\left(\frac{\partial \tilde{F}_{pq}}{\partial p_n}\right)_I = -\sum_{P\in\Omega}\left(\mathcal{G}_I^{pq}\right)_Q \Delta\Omega_Q, \quad n=1,...,N \qquad (6.11)$$

where

$$\left(\mathcal{G}_I^{pq}\right)_Q = \sum_{\zeta=x,y,z} \frac{|E_{\zeta p}(Q)|}{a}\hat{\boldsymbol{\zeta}} \cdot \int_0^{T_{\max}} \left.\frac{\partial R(\mathbf{E}_q)}{\partial p_n}\right|_{(Q,t)} \cos[\phi_{\zeta p}(Q,t)]dt\,. \qquad (6.12)$$

From (6.6) and (6.11) , we obtain the derivative of $\tilde{F}_{pq}$ as

$$\frac{\partial \tilde{F}_{pq}}{\partial p_n} = \frac{\partial \operatorname{Re}\tilde{F}_{pq}}{\partial p_n} + j\cdot\frac{\partial \operatorname{Im}\tilde{F}_{pq}}{\partial p_n} = -\sum_{Q\in\Omega}\left(\tilde{\mathcal{G}}^{pq}\right)_Q \Delta\Omega_Q \qquad (6.13)$$

where

$$\left(\tilde{\mathcal{G}}^{pq}\right)_Q = \left(\mathcal{G}_R^{pq}\right)_Q + j\left(\mathcal{G}_I^{pq}\right)_Q. \qquad (6.14)$$

Substituting (6.10) and (6.12) into (6.14), we obtain

$$\left(\tilde{\mathcal{G}}^{pq}\right)_Q = \frac{j\exp(-j\cdot\varphi_g)}{a}\cdot\left[\tilde{\mathbf{E}}_p \cdot \frac{\partial R(\tilde{\mathbf{E}}_q)}{\partial p_n}\right]_Q \qquad (6.15)$$

where

$$\frac{\partial R(\tilde{\mathbf{E}}_q)}{\partial p_n} = -\frac{\partial \alpha}{\partial p_n} \cdot \ddot{\tilde{\mathbf{E}}}_q - \frac{\partial s}{\partial p_n} \cdot \dot{\tilde{\mathbf{E}}}_q . \tag{6.16}$$

Here, $\ddot{\tilde{\mathbf{E}}}_q$ and $\dot{\tilde{\mathbf{E}}}_q$ are the phasors representing the respective time-derivatives of the ω_0 spectral components of $\mathbf{E}_q(t)$:

$$\ddot{\tilde{E}}_{\zeta q} = \mathcal{F}^{\omega_0}\left\{D_{tt}E_{\zeta q}\right\} \approx \mathcal{F}^{\omega_0}\left\{\Delta t^2 \frac{\partial^2 E_{\zeta q}}{\partial t^2}\right\} = -\omega_0^2 \cdot \Delta t^2 \cdot \tilde{E}_{\zeta q} \tag{6.17}$$

$$\dot{\tilde{E}}_{\zeta q} = \mathcal{F}^{\omega_0}\left\{D_{t2}E_{\zeta q}\right\} = 2j\omega_0 \Delta t \cdot \tilde{E}_{\zeta q} . \tag{6.18}$$

In (6.17)-(6.18), $\mathcal{F}^{\omega_0}$ denotes the Fourier transform. In (6.16), the derivatives of the system coefficients are the same as in (6.3) and (6.4). Finally, from (6.13) and (6.15), we obtain

$$\frac{\partial \tilde{F}_{pq}}{\partial p_n} = -\frac{j \cdot \exp(-j \cdot \varphi_g)}{a} \sum_{P \in \Omega} \Delta\Omega_Q \cdot \left[\tilde{E}_p \cdot \frac{\partial R(\tilde{E}_q)}{\partial p_n}\right]_Q . \tag{6.19}$$

In the same manner, we obtain the spectral sensitivity formula for parameters belonging to a discrete space (the case of shape parameters):

$$\frac{\partial \tilde{F}_{pq}}{\partial p_n} \approx -\frac{j \cdot \exp(-j \cdot \varphi_g)}{a} \sum_{Q \in \Omega} \Delta\Omega_P \cdot \left[(\tilde{E}_p)_n \cdot \frac{\Delta_n R(\tilde{E}_q)}{\Delta p_n}\right]_Q \tag{6.20}$$

where

$$\frac{\Delta_n R(\tilde{\mathbf{E}})}{\Delta p_n} = \frac{\Delta_n \mathscr{C}^2 \tilde{\mathbf{E}}}{\Delta p_n} - \frac{\Delta_n \alpha}{\Delta p_n} \cdot \ddot{\tilde{\mathbf{E}}} - \frac{\Delta_n s}{\Delta p_n} \cdot \dot{\tilde{\mathbf{E}}} - \frac{\Delta_n (\beta \dot{\tilde{\mathbf{J}}})}{\Delta p_n} \tag{6.21}$$

and

$$\dot{\tilde{J}}_{\zeta q} = \mathscr{F}^{\omega_0} \left\{ D_t J_{\zeta q} \right\} = j\omega_0 \Delta t \cdot \tilde{J}_{\zeta q} . \tag{6.22}$$

The system-coefficient differences $\Delta_n \mathscr{C}^2$, $\Delta_n \alpha$, $\Delta_n s$ and $\Delta_n (\beta \dot{\tilde{\mathbf{J}}}_q)$ are determined in the same manner as in (3.2) [1]-[2].

In contrast to (6.1) and (3.1), the sensitivity formulas (6.19) and (6.20) use the field phasors at the perturbation grid points instead of their time waveforms. Thus, at each perturbation grid point only one complex number per frequency point is recorded instead of the entire waveform. This is important since discrete Fourier transform can be performed "on-the-fly" with negligible memory requirements.

6.3 NUMERICAL EXAMPLES

In all examples, mesh refinement is carried out ensuring mesh convergence error below 5 %. All analyses are performed over a frequency range from 3.0 GHz to 5.0 GHz. The *S*-parameter derivatives and the derivatives of a point-wise response function are computed. The point-wise function defined in (3.25) can be considered as a special case of an *S*-parameter. The results obtained using our new spectral approach are marked with S-SASA. The results obtained using a central-node grid

with our time-domain self-adjoint sensitivity analysis method are marked as TD-SASA.

6.3.1 Validation of the Spectral Approach

A. Parallel-Plate Waveguide

We first verify the spectral approach through a 1-D inhomogeneous parallel-plate waveguide. The structure and its parameters are shown in Figure 6.1. Uniform mesh of $\Delta h = 0.5$ mm is used. The current-density excitation is a modulated Gaussian pulse, which covers the frequency band from 3.0 GHz to 5.0 GHz. The magnitude spectrum at 3.0 GHz and 5.0 GHz is at about 35 % of the maximum spectral component. The source current density is uniformly distributed across the port conforming to a TEM plane wave.

The optimizable parameters are $\boldsymbol{p} = [w, \varepsilon_{r2}, \sigma_{r2}]^T$, which are the shape and constitutive parameters of the central layer. The derivatives of $|S_{11}|$ and $|S_{21}|$ with respect to w are shown in Figure 6.2 and Figure 6.3, respectively. As expected, the results obtained using the spectral approach are identical with those obtained using the central-node time-domain self-adjoint sensitivity analysis method.

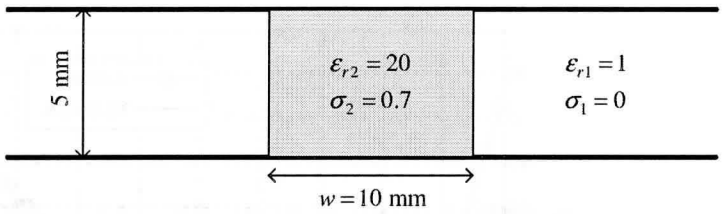

Fig. 6.1 The geometry of the parallel-plate waveguide used for the verification of the spectral approach.

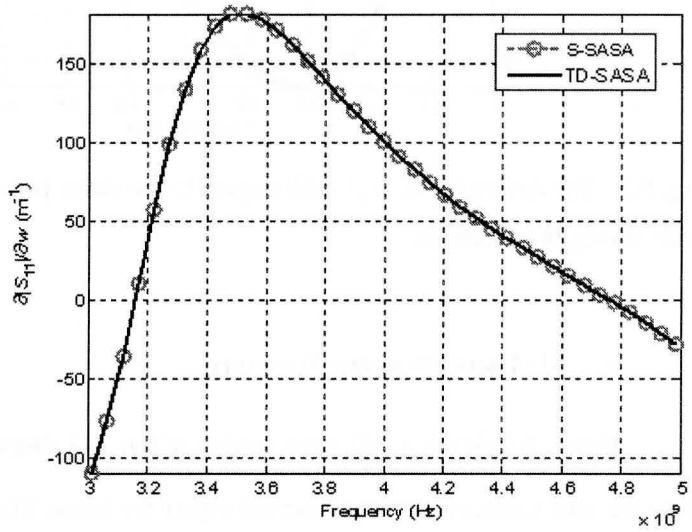

Fig. 6.2 The derivative of $|S_{11}|$ with respect to the shape parameter w in the parallel-plate waveguide example.

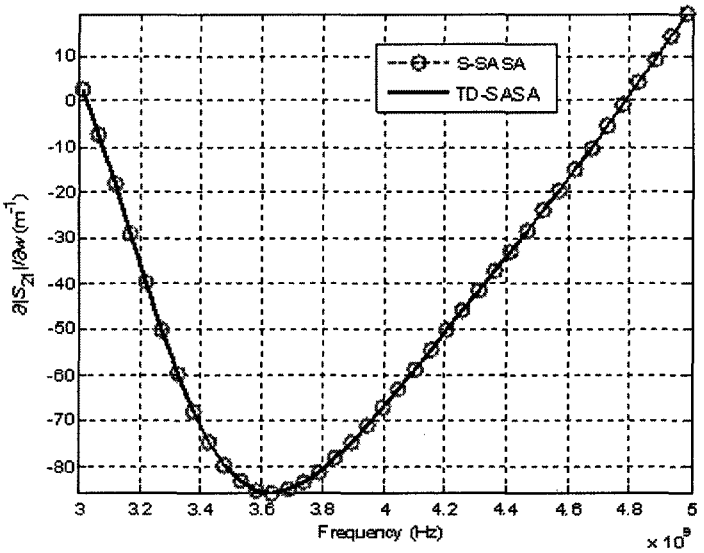

Fig. 6.3 The derivative of $|S_{21}|$ with respect to the shape parameter w in the parallel-plate waveguide example.

B. 3-D Lossy Dielectric Structure

Figure 6.4 shows a 2-D cross section of the 3-D structure and its parameters. Both the host medium and the immersed object are lossy. The host medium is a box with a corner at (0, 0, 0) mm. It extends 32 mm along the x-axis, 36 mm along the y-axis and 32 mm along the z-axis. The immersed object is a cube with a corner at (12, 10, 12) mm and a side of a = 8 mm. Uniform mesh is used with $\Delta h = 0.5$ mm. The excitation is the same as the excitation in the parallel-plate waveguide example.

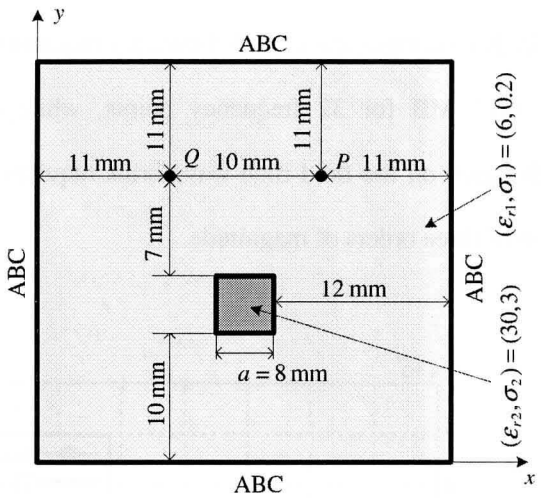

Fig. 6.4 The geometry of the 3-D example used for the verification of the spectral approach: 2-D cut in the plane of the observation and excitation points P and Q.

The optimizable parameters are $\boldsymbol{p} = [a, \varepsilon_{r2}, \sigma_{r2}]^T$, which are the size and the constitutive parameters of the immersed object. We compute the Jacobians of the point-wise response functions defined in (3.25). In Figure 6.4, Q is the excitation point located at (11, 25, 16) mm while P is the observation point located at (21, 25, 16) mm. The derivatives of $|F_{QQ}|$ and $|F_{PQ}|$ with respect to ε_{r2} are shown in Figure 6.5 and Figure 6.6, respectively. The derivative of $|F_{QQ}|$ with respect to σ_2 is plotted in Figure 6.7. As expected, the results obtained using the spectral approach are exactly the same as those obtained using our original self-adjoint sensitivity analysis on central-node grid, which uses time waveforms of the field solution.

In this example, the recorded memory requirement of the spectral approach is roughly 6.75 MB for 32 frequency points, while our time-domain self-adjoint approach based on the field time waveforms requires 2230 MB. This is a memory reduction of three orders of magnitude.

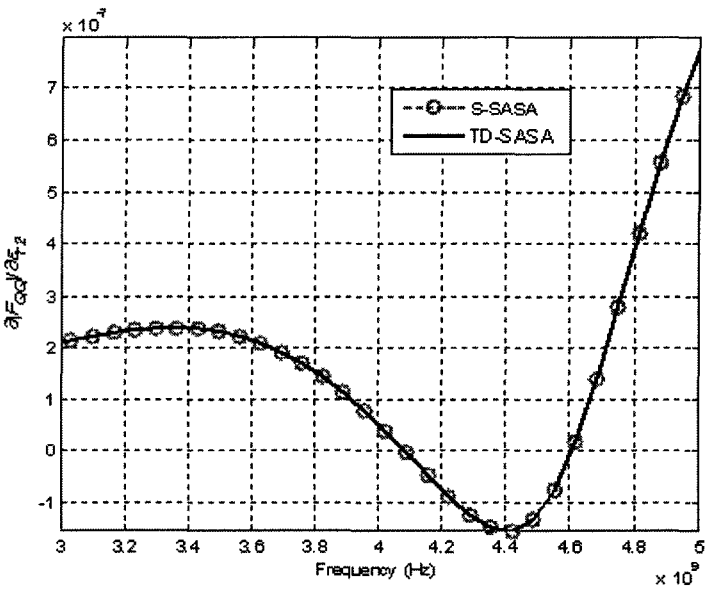

Fig. 6.5 Derivative of $|F_{QQ}|$ with respect to ε_{r2} in the 3-D example.

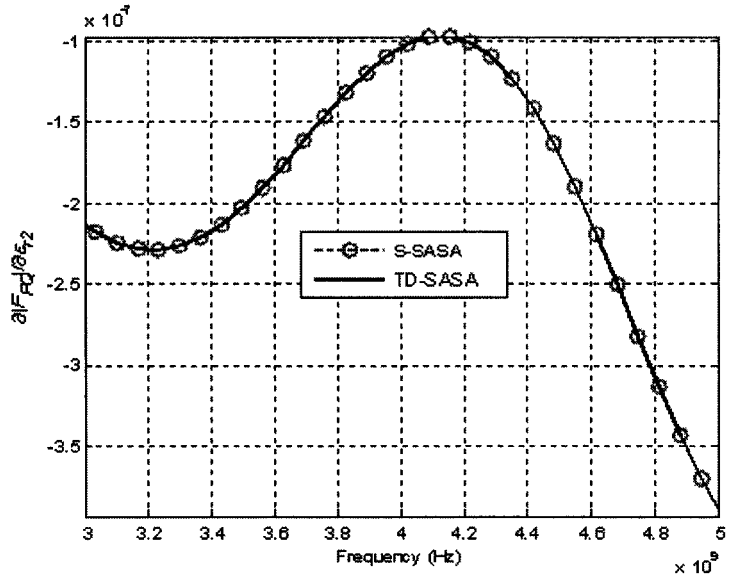

Fig. 6.6 Derivative of $|F_{PQ}|$ with respect to ε_{r2} in the 3-D example.

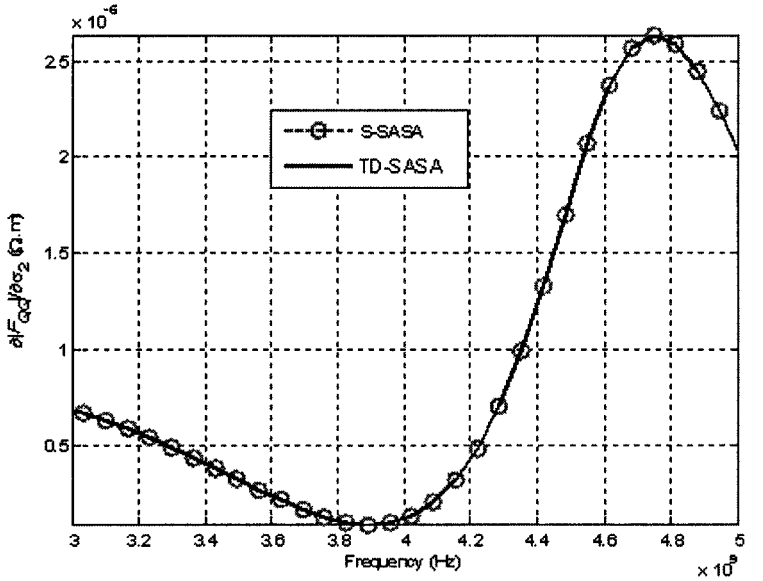

Fig. 6.7 Derivative of $|F_{QQ}|$ with respect to σ_2 in the 3-D example.

6.3.2 Jacobian Distributions in a 3-D Imaging Example

The objective of microwave tomography is to reconstruct the complex permittivity profile in an imaged region. This inverse problem is cast in the form of an optimization problem, which is solved by minimizing a cost function. The cost function is a measure of the difference between the measured (or target) responses and the responses produced by the forward model for the current estimate of the permittivity distribution. It can be defined as [7]

$$F(\boldsymbol{\varepsilon}) = \| \boldsymbol{\Phi}(\boldsymbol{\varepsilon}) - \bar{\boldsymbol{\Phi}} \| + \delta \cdot \| \boldsymbol{\varepsilon} - \boldsymbol{\varepsilon}_b \| \tag{6.23}$$

where $\bar{\boldsymbol{\Phi}} \in \mathbb{C}^{N_r \times 1}$ is the vector of target responses, $\boldsymbol{\Phi} \in \mathbb{C}^{N_r \times 1}$ is the vector of responses obtained from the forward model, and $\|\cdot\|$ represents a suitable, e.g., l_2, norm. The second term in (6.23) is the regularization term where the coefficient δ is usually chosen between 0 and 0.5. The vector $\boldsymbol{\varepsilon} \in \mathbb{C}^{N \times 1}$ represents the unknown complex permittivity profile of the reconstructed scatterer in the assumed discrete space, while $\boldsymbol{\varepsilon}_b \in \mathbb{C}^{N \times 1}$ is the "background" permittivity profile which is assumed known. The forward model is typically a high-frequency EM simulation. The optimization problem,

$$\boldsymbol{\varepsilon}^* = \arg\min_{\boldsymbol{\varepsilon}} F(\boldsymbol{\varepsilon}) \tag{6.24}$$

is solved iteratively by properly updating the permittivity distribution $\boldsymbol{\varepsilon}$. Often, at the initial iteration, $\boldsymbol{\varepsilon}$ is set equal to $\boldsymbol{\varepsilon}_b$, i.e., $\boldsymbol{\varepsilon}^{(0)} = \boldsymbol{\varepsilon}_b$.

When EM simulations are used as forward models, gradient-based optimization techniques are preferred in solving (6.24) due to their fast convergence [7]-[13]. On the other hand, gradient-based techniques require the Jacobian of the cost function $F(\boldsymbol{\varepsilon})$. The memory-efficient self-adjoint technique proposed here makes this computation possible. Moreover, since our technique reduces the Jacobian computation to a simple post-process, it can be applied with commercial simulators.

In the examples below, we consider the particular cost function [5]

$$F(\boldsymbol{\varepsilon}) = 0.5\left(\sum_{r=1}^{N_r} | \boldsymbol{\Phi}_r - \bar{\boldsymbol{\Phi}}_r |^2 + \delta \sum_{n=1}^{N} | \varepsilon_n - \varepsilon_{bn} |^2 \right) \tag{6.25}$$

and its permittivity Jacobian. The complex permittivity of each voxel ε_n, can be expressed in terms of its real part ε_n' and its effective specific conductivity σ_n as

$$\varepsilon_n = \varepsilon_n' \left(1 - j \frac{\sigma_n}{\omega \varepsilon_n'} \right), \quad n = 1, ..., N. \tag{6.26}$$

The respective derivatives of the cost function in (6.25) are

$$\frac{\partial F}{\partial \varepsilon_n'} = \sum_{r=1}^{N_r} \left[(\Phi_r - \bar{\Phi}_r)_R \cdot \left(\frac{\partial \Phi_r}{\partial \varepsilon_n'} \right)_R + (\Phi_r - \bar{\Phi}_r)_I \cdot \left(\frac{\partial \Phi_r}{\partial \varepsilon_n'} \right)_I \right] + \delta \cdot (\varepsilon_n - \varepsilon_{bn})_R \tag{6.27}$$

$$\frac{\partial F}{\partial \sigma_n} = \sum_{r=1}^{N_r} \left[(\Phi_r - \bar{\Phi}_r)_R \cdot \left(\frac{\partial \Phi_r}{\partial \sigma_n} \right)_R + (\Phi_r - \bar{\Phi}_r)_I \cdot \left(\frac{\partial \Phi_r}{\partial \sigma_n} \right)_I \right] - (\delta / \omega) \cdot (\varepsilon_n - \varepsilon_{bn})_I . \tag{6.28}$$

In (6.27)-(6.28), each complex response derivative $\partial \Phi_r / \partial \varepsilon_n'$, $\partial \Phi_r / \partial \sigma_n$ ($n = 1,\ldots,N$, $r = 1,\ldots,N_r$) is computed using the sensitivity formula (6.19).

In the following example, we compute the derivatives of the cost function at all voxels inside the imaged region. These derivatives, which constitute the Jacobian matrix, can be plotted as functions of the position of the voxel whose permittivity is an optimizable parameter. We refer to such plots as Jacobian maps.

Figure 6.8a shows a 2-D cut of a simplified semi-spherical breast 3-D model. This is the target structure, which serves to obtain the "measured" field data. It consists of a homogenized "breast" medium, a spherical "tumor" and a "chest wall". The breast semi-sphere has its center at (40, 35, 40) mm. Its diameter is 50 mm. The homogenized breast constitutive parameters are $\varepsilon_{r1} = 4.5$ and $\sigma_1 = 0.18$ S/m. The tumor sphere has its center at (28, 18, 40) mm and its diameter is 5 mm. Its constitutive parameters are $\varepsilon_{r2} = 40$ and $\sigma_2 = 1.6$ S/m. The chest wall is modeled as a thin rectangular box with a corner at (10, 35, 10) mm. It extends 60 mm, 5 mm and 60 mm along the x, y and z axes, respectively. Its constitutive parameters are $\varepsilon_{r3} = 50$ and $\sigma_3 = 3.0$ S/m. The surrounding (coupling) medium is terminated with absorbing boundaries. Its constitutive parameters are $\varepsilon_{r4} = 4.0$ and $\sigma_4 = 0.1$ S/m. The overall computational domain is a box with a corner at (0, 0, 0) mm, which extends 80 mm, 50 mm and 80 mm along the x, y and z axes, respectively. The FDTD mesh is uniform with $\Delta h = 0.5$ mm. The point-wise excitations (see points P_1

and P_2 in Figure 6.8) use a modulated Gaussian pulse, which covers the frequency band from 3.0 GHz to 5.0 GHz. P_1 and P_2 are located at (14, 28, 40) mm and (66, 28, 40) mm, respectively.

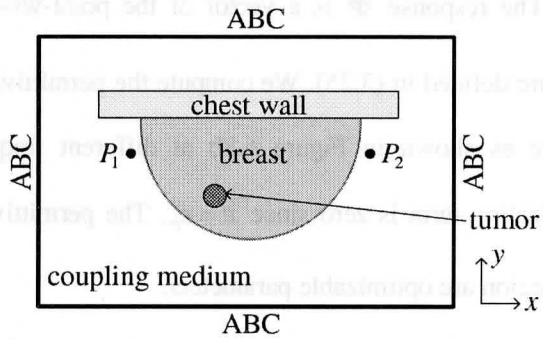

(a)

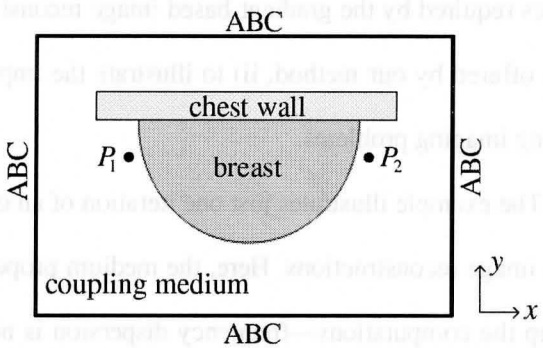

(b)

Fig. 6.8 The 2-D cuts of the 3-D models: (a) target model; (b) model at the starting point of the imaging reconstruction.

Figure 6.8b shows the 2-D cut of an estimated breast model. This particular estimate represents a typical starting point for imaging reconstruction, which

assumes a "tumor-free" simplified model of the breast. In this example, our estimate is identical with the target except for the absence of the tumor. Its permittivity distribution coincides with the assumed background permittivity, i.e., $\boldsymbol{\varepsilon} = \boldsymbol{\varepsilon}_b$.

The response $\boldsymbol{\Phi}$ is a vector of the point-wise responses $F_{\hat{p}_1\hat{p}_1}$ and $F_{\hat{p}_2\hat{p}_1}$, which are defined in (3.25). We compute the permittivity Jacobian for the estimated structure as shown in Figure 6.8b at different frequencies. Note that here the regularization term is zero since $\boldsymbol{\varepsilon} = \boldsymbol{\varepsilon}_b$. The permittivities of all voxels inside the breast region are optimizable parameters.

Our goal in considering this example is twofold: i) to illustrate the computer resources required by the gradient-based image reconstruction and the great memory savings offered by our method; ii) to illustrate the importance of the Jacobian maps in solving imaging problems.

The example illustrates just one iteration of an optimization process, typically used in image reconstructions. Here, the medium properties are greatly simplified to speed up the computations—frequency dispersion is not taken into account and the "breast" medium hosting the tumor is homogeneous. Neither of these simplifying assumptions, however, reflects on limitations of our sensitivity analysis technique. Regardless how complex the media may be, as long as the field solution is accurate, so will be the computed sensitivities. Also, we emphasize that our method utilizes a spectral formulation, thereby allowing for the use of different permittivity and

conductivity values at different frequencies where dispersive media are involved.

Here, we plot the Jacobian maps in the plane y = 18 mm, which contains the tumor's center in the target model in Figure 6.8a. The map spans a square with one corner at (22, 18, 22) mm and the opposite corner at (58, 18, 58) mm. Figures 6.9a-e show the Jacobian maps at 3 GHz, 3.5 GHz, 4 GHz, 4.5 GHz and 5 GHz, respectively. We observe that a minimum appears at the point (28, 18, 40) mm, which coincides with the center of the tumor in the target model. We find that on average, a wide-band set of Jacobian maps indicates fairly accurately the location of the scatterer.

One may note that the amplitudes of the Jacobians are very small. This is because they reflect changes in the cost function due to changes of the permittivity of a single voxel of the computational domain. Since a voxel constitutes barely 1-millionth part of the computational domain, its influence on the overall response is indeed miniscule. Despite the fact that the Jacobian map reflects the effect of such miniscule perturbations, it is accurate due to the exact nature of our self-adjoint formula for material parameter derivatives. Note that this computation is practically impossible with response-level finite differences because of: i) huge errors due to catastrophic cancellation; and ii) prohibitive computation time.

This example illustrates well the benefits high-quality Jacobian maps can bring to image reconstruction. First, they are required by all gradient-based reconstruction algorithms; see, for example, the Fréchet derivative operator in the

Newton-type minimization procedure in [7] or the Jacobian matrix in the Gauss-Newton procedure in [13]. Second, in addition to the cost function, the Jacobian doubles our knowledge of the system behavior. In particular, the minima and maxima of a Jacobian distribution are indicative of the location at which the model constitutive parameters differ the most from those of the object under test. As illustrated here, when the simulated host medium is an exact model of the host medium of the measured object, the wideband Jacobian maps can accurately locate embedded scatterers through a *single* simulation. In the reality of microwave imaging, however, exact knowledge of the entire host medium is usually not available, hence the need for iterative procedures. The convergence rate of such procedures crucially depends on the accuracy of the Jacobian/Fréchet matrices.

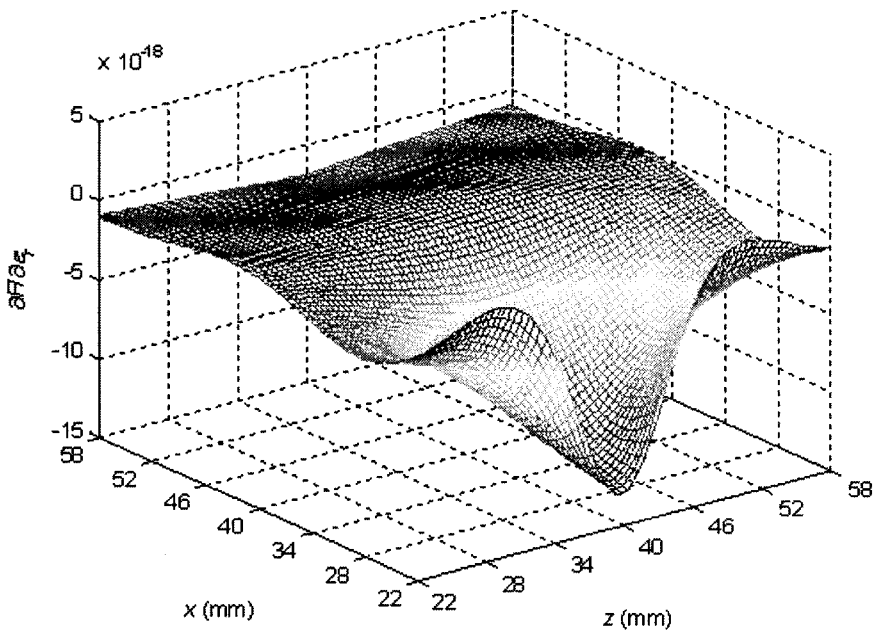
x 10^-18
5
0
-5
-10
-15
∂F/∂ξ
58
52
46
40
34
28
22
x (mm)
22
28
34
40
46
52
58
z (mm)

(a)

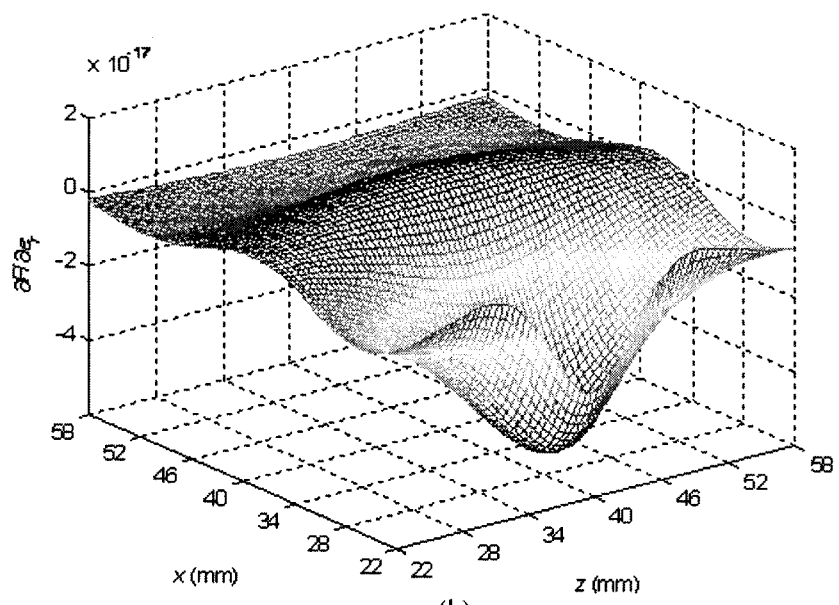
x 10^-17
2
0
-2
-4
∂F/∂ξ
58
52
46
40
34
28
22
x (mm)
22
28
34
40
46
52
58
z (mm)

(b)

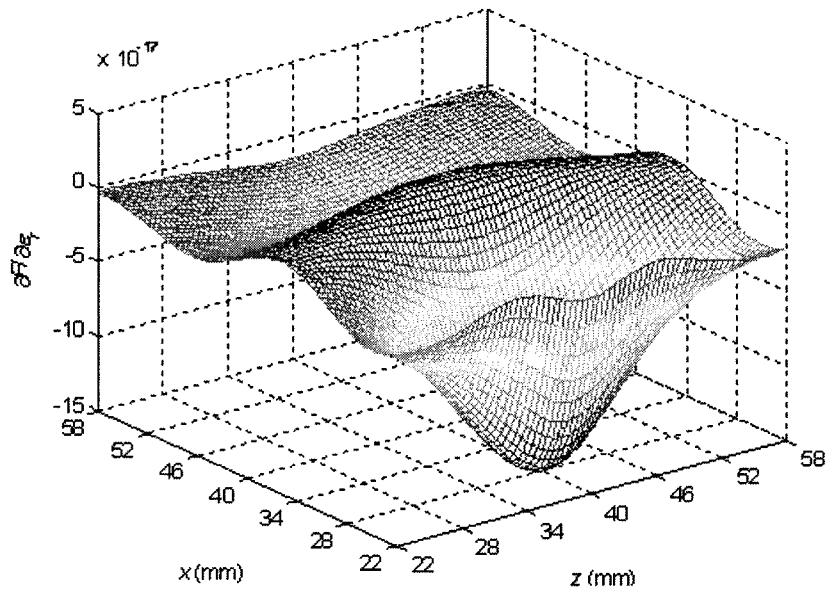
x 10^-17
5
0
-5
-10
-15
∂F/∂ε_f
58
52
46
40
34
28
22
x (mm)
22
28
34
40
46
52
58
z (mm)

(c)

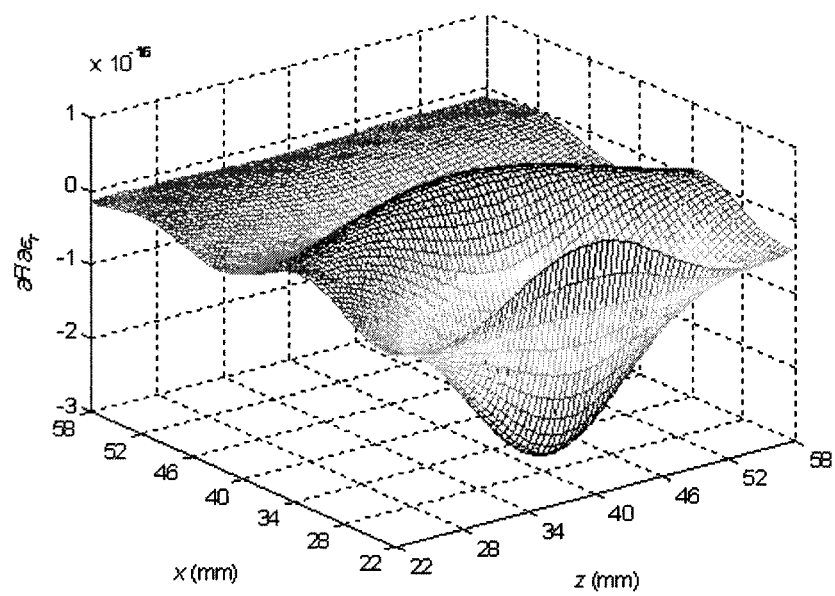
x 10^-16
1
0
-1
-2
-3
∂F/∂ε_f
58
52
46
40
34
28
22
x (mm)
22
28
34
40
46
52
58
z (mm)

(d)

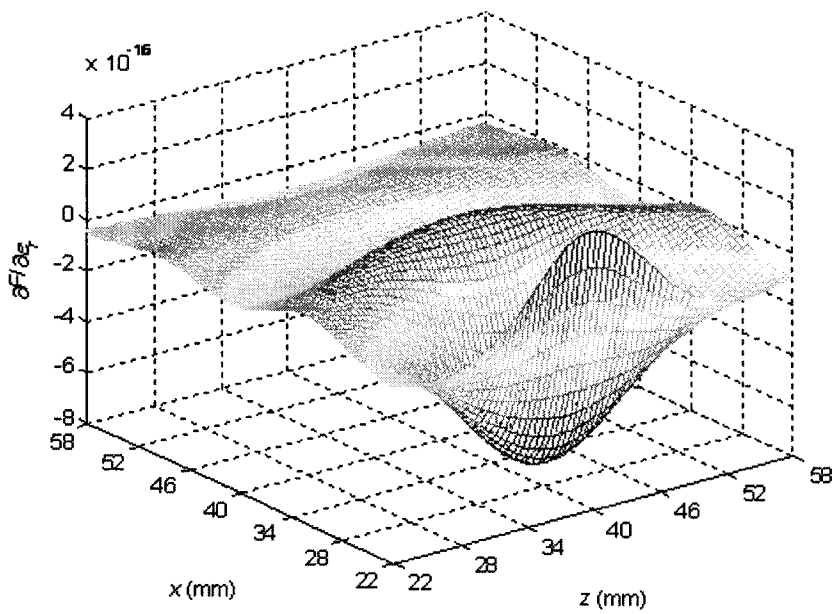

(e)

Fig. 6.9 Jacobian maps in the plane y = 18 mm at: (a) 3 GHz; (b) 3.5 GHz; (c) 4 GHz; (d) 4.5 GHz; (e) 5 GHz.

6.4 DISCUSSION OF NUMERICAL EFFICIENCY

The memory requirement of the proposed spectral approach is $24 \times N \times N_f$ bytes. Here, N is number of perturbation grid points, i.e., the number of points where the complex permittivity is reconstructed, and N_f denotes the number of frequencies of interest. At each frequency, the spectral components of all three **E**-field components

are recorded at each perturbation grid point. Note that each spectral scalar component consists of two real values, e.g., magnitude and phase. Thus, if single precision data format is used, the memory requirement per permittivity voxel per frequency is $3 \times 2 \times 4 = 24$ bytes.

On the other hand, the memory requirement of our original time-domain approach is $12 \times N \times N_t$ bytes, where N_t denotes the number of time steps in the simulation. Thus, our spectral approach realizes a memory saving factor of $N_t / (2N_f)$. In the 3-D imaging example of section 6.3.2, the total number of voxels in the imaging region is about 380 000. The memory required to store the data for the Jacobian computation in the whole 3-D imaged region is roughly 310 MB for 9 frequencies (from 3 GHz to 5 GHz with a step of 0.25 GHz). In contrast, the estimated memory requirement for our original time-domain approach is about 148.9 GB for N_t = 10 000. Such memory demands make the time-domain approach inapplicable. The estimated memory saving factor for this example when using the spectral self-adjoint approach is about 490, which makes the memory requirement manageable.

It is worth noting that if the required field solutions are recorded onto the hard disk at each iteration, the simulation slows down gravely. This is due to the excessive time required to read/write from/to the hard drive [3]. In contrast, due to the relatively small memory requirements of the spectral approach, all required field solutions can be kept in the computer RAM and exported to the hard disk after the

simulation is over. Thus, the slowdown of the simulation is insignificant. This is an important advantage of the spectral approach over our original time-domain approach.

Beside its memory efficiency, the spectral approach proves to be more computationally efficient as well. For example, the computational time of the Jacobian post-process which uses the field phasors is less than 9 minutes, while it is estimated that the computational time is more than 300 minutes for our original time-domain approach. This is because the original time-domain sensitivity formula performs a Fourier-type time integration. It may easily take hours to read the 148.9 GB of the recorded time waveforms from the hard disk.

We note that when working with the field phasors rather than their waveforms, there is some slow-down in the FDTD simulation due to the discrete Fourier transform performed 'on the fly'. However, this discrete Fourier transform overhead is negligible in comparison with the time required by the FDTD algorithm. This is because the discrete Fourier transform update needs only three floating-point operations per time step per voxel in the imaged region, while the FDTD update needs a minimum of thirty floating-point operations per time step per cell in the entire computational domain. Note that the imaging region usually covers only 1/10 to 1/5 of the whole computational domain. A rough estimate shows that the slow-down due to the discrete Fourier transform is roughly in the range of 1 % to 2 % of the total FDTD simulation time.

6.5 SUMMARY

We proposed a spectral formula for the self-adjoint computation of response Jacobians. It operates on the spectral components of the **E**-field instead of its time waveforms. Thus, the length of the time-domain simulation is no longer a factor in the memory requirements. In comparison with our original time-domain approach, the memory saving factor is approximately $N_t/(2N_f)$, where N_t is the number of time steps and N_f is the number of frequencies of interest.

To improve the accuracy of the Jacobian computation, the proposed approach adopts a central-node grid, where all three **E**-filed components of the central-node are collocated at the center of the traditional Yee cell.

The spectral approach was verified through 1-D and 3-D examples. The Jacobians obtained using the proposed approach are the same as those obtained with our original time-domain approach on central-node grid. In addition to the verifications, we computed the wideband Jacobian maps for a microwave imaging problem. The importance of Jacobian maps in the application of tumor localization was also addressed.

The numerical efficiency of the spectral approach was discussed in Section 6.4. We found that the spectral approach is not only memory efficient, but also

computationally efficient. These advantages are more profound in microwave inverse problems, where our original time-domain approach becomes inapplicable due to the excessive memory requirement.

The proposed sensitivity solver is well suited for the computation of wideband response Jacobians in microwave imaging and design problems. It can be easily implemented as standalone software, which can work with commercial EM simulators for the Jacobian computation.

REFERENCES

[1] N. K. Nikolova, Ying Li, Yan Li and M. H. Bakr, "Sensitivity analysis of scattering parameters with electromagnetic time-domain simulators," *IEEE Trans. Microw. Theory Tech.*, vol. 54, pp. 1589–1610, Apr. 2006.

[2] Y. Song, Ying Li, N. K. Nikolova, and M. H. Bakr, "Self-adjoint sensitivity analysis of lossy dielectric structures with electromagnetic time-domain simulators," *Int. J. of Numerical Modeling: Electronic Networks, Devices and Fields*, vol. 21, No. 1–2, pp. 117–132, Jan.–Apr. 2008.

[3] Y. Song, N. K. Nikolova, and M. H. Bakr, "Efficient time-domain sensitivity analysis using coarse grids," *Applied Computational Electromagnetics Society Journal*, vol. 23, No. 1, pp. 5–15, Mar. 2008.

[4] Y. Song and N. K. Nikolova, "Central-node approach for accurate self-adjoint sensitivity analysis of dielectric structures," *IEEE MTT-S Int. Microwave Symposium*, June 2007, pp. 895–898.

[5] Y. Song and N. K. Nikolova, "Memory efficient method for wideband self-adjoint sensitivity analysis," *IEEE Trans. Microwave Theory Tech.*, vol. 56, No. 8, pp. 1917–1927, Aug. 2008.

[6] QuickWave-3D v. 6.0, *Reference Manual*, QWED, 2006, http://www.qwed.com.pl/index.html.

[7] W. C. Chew and J. H. Lin, "A frequency-hopping approach for microwave imaging of large inhomogeneous bodies," *IEEE Microwave Guided Wave Lett.*, vol. 5, pp. 439–441, Dec. 1995.

[8] P. M. Meaney, M. W. Fanning, D. Li, S. P. Poplack, K. D. Paulsen, "A clinical prototype for active microwave imaging of the breast," *IEEE Trans. Microwave Theory Tech.*, vol. 48, pp. 1841–1853, Nov. 2000.

[9] Z. Q. Zhang and Q. H. Liu, "Three-dimensional nonlinear image reconstruction for microwave biomedical imaging," *IEEE Trans. Biomed. Eng.*, vol. 51, pp. 544–548, March 2004.

[10] R. E. Kleinman and P. M. van den Berg, "A modified gradient method for two-dimensional problems in tomography," *J. Comput. Appl. Math.*, vol. 42, pp. 17–35, 1992.

[11] S. Barkeshli and R. G. Lautzenheiser, "An iterative method for inverse scattering problems based on an exact gradient search," *Radio Sci.*, vol. 29, pp. 1119–1130, July–Aug. 1994.

[12] H. Harada, D. J. N. Wall, T. Takenaka, and M. Tanaka, "Conjugate gradient method applied to inverse scattering problems," *IEEE Trans. Antennas Propagat.*, vol. 43, pp. 784–792, Aug. 1995.

[13] T. K. Chan, Y. Kuga, and A. Ishimaru, "Subsurface detection of a buried object using angular correlation function measurement," in *Proc. PIERS'97,* Cambridge, MA, pp. 158, July 1997.

Chapter 7

CONCLUSIONS

This thesis has presented recent advances in the self-adjoint sensitivity analysis with time-domain EM field solutions. The proposed sensitivity solvers are independent from the simulator's grid, discretization method and system equations. They are based on a self-adjoint formulation which eliminates the need to perform adjoint system analysis. The sensitivity computation is done as a simple post-process of the field solution which can be applied with any commercial time-domain solvers. Our sensitivity solvers can be easily implemented as standalone software to plug into simulators aiding microwave design and image reconstruction.

Two different sensitivity solvers were developed in this work. The first sensitivity solver is based on a self-adjoint formula which operates on the time waveforms of the field solution. Three different approaches associated with this sensitivity solver have been introduced. They are the original self-adjoint approach, the coarse-grid approach and the central-node approach. Our original self-adjoint approach adopts the staggered grid of the FDTD simulation. The efficient coarse-grid approach uses a coarse independent FD grid whose step size can be many times

larger than that of the FDTD simulation. The accurate central-node approach uses a central-node grid whose field solutions are collocated in the center of the traditional Yee cell.

Our second sensitivity solver is based on a spectral sensitivity formula which operates on the spectral components of the field solution. This is a memory efficient wideband sensitivity solver. It overcomes the drawback associated with our first sensitivity solver whose memory requirements may become excessive when the number of the perturbation grid points is very large.

In Chapter 2, we reviewed the time-domain discrete adjoint techniques for the sensitivity analysis. These techniques are limited to in-house simulation codes. They are not applicable with commercial solvers due to the difficulty of setting up an adjoint excitation.

Our time-domain self-adjoint approach overcomes the above limitation. It was introduced in Chapter 3. The S-parameter sensitivity formula and the sensitivity formula of a point-wise function were presented. In this approach, the adjoint system analysis is not needed. The adjoint field is computed from the original field through simple mathematical manipulations. The accuracy of our approach is better or comparable to that of the central FD estimates at the response level.

We presented the coarse-grid approach in Chapter 4. We showed that the cell size of the sensitivity solver grid can be many times larger than that of the simulation grid while maintaining good accuracy. The proposed technique reduces the memory

requirements significantly. Recommendations for the proper choice of the cell size were also given.

In Chapter 5, we proposed a central-node approach for accurate computation of response sensitivities. It is an important improvement over the original approach introduced in Chapter 3. The sensitivity solver uses an independent central-node grid whose **E**-field components are collocated in the center of the Yee cell. The accuracy of the central-node approach is approved significantly in compare with that of our original approach in the case of dielectric structures while the computational efficiency remains the same. At the same time, the implementation is simplified, especially for 3-D problems, since the derivatives of the system coefficients are independent of any averaging scheme that the solver may use at material interfaces. The focus of the central-node approach is on 3-D lossy-dielectric structures. It is also applicable to metallic structures.

The spectral self-adjoint sensitivity solver was introduced in Chapter 6. We derived the spectral formula in details. The spectral sensitivity solver operates on the spectral components of the **E**-field instead of its time waveforms. Thus, the length of the time-domain simulation is no longer a factor in the memory requirements. By using the spectral approach, the memory requirements are reduced roughly from Gigabytes to Megabytes. The focus of this approach is on microwave imaging applications, where our first sensitivity solver is inapplicable due to the excessive

memory requirements. The proposed sensitivity solver is also well suited for microwave design problems.

The theoretical work in this thesis has been verified thoroughly and supported by various examples. The proposed self-adjoint approaches are the most computationally efficient methods for the computation of response Jacobians. They are milestones in the computation of response sensitivities since they can be easily applied with commercial simulators and double our knowledge of the system behavior in the design (modeling) parameter space. Our self-adjoint sensitivity solvers make EM simulation-based optimizations feasible.

We expect that more work will be carried out in self-adjoint sensitivity analysis. We foresee the following developments.

First, more work should be done regarding the application of our time-domain self-adjoint sensitivity analysis methods to microwave design problems. In principle, a general frequency-domain self-adjoint method can be developed, which will be applicable with both frequency-domain and time-domain simulators.

Second, microwave imaging reconstruction utilizing our time-domain self-adjoint sensitivity methods should be investigated.

Finally, the development of a full-fledged computer-aided-design and modelling framework incorporating our proposed sensitivity solvers will be a very exciting experience. Such a framework will bring about a breakthrough in microwave design and imaging. Currently, most of the commercial solvers are not

capable of providing response sensitivity information. The response Jacobians are usually computed through FD estimates, which can easily become impractical when the number of the optimizable parameters is large.

BIBLIOGRAPHY

Y. Song and N. K. Nikolova, "Sensitivity analysis of electrically small objects in lossy inhomogeneous structures," 2007 *IEEE AP-S Int. Symp.*, pp. 4453–4456, Jun. 2006.

Y. Chung, C. Cheon, I. Park, and S. Hann, "Optimal shape design of microwave device using FDTD and design sensitivity analysis," *IEEE Trans. Microwave Theory Tech.*, vol. 48, no. 12, pp. 2289–2296, Dec. 2000.

Y. Chung, J. Ryu, C. Cheon, I. Park, and S. Hahn, "Optimal design method for microwave device using time domain method and design sensitivity analysis—Part I: FETD case," *IEEE Trans. Magn.*, vol. 37, no. 9, pp. 3289–3293, Sep. 2001.

Y. Chung, J. Ryu, C. Cheon, I. Park, and S. Hahn, "Optimal design method for microwave device using time domain method and design sensitivity analysis—Part II: FDTD case," *IEEE Trans. Magn.*, vol. 37, no. 9, pp. 3255–3259, Sep. 2001.

N. K. Nikolova, J. W. Bandler, and M. H. Bakr, "Adjoint techniques for sensitivity analysis in high-frequency structure CAD," *IEEE Trans. Microwave Theory Tech.*, vol. 52, no. 1, pp. 403–419, Jan. 2004.

N. K. Nikolova, H. W. Tam, and M. H. Bakr, "Sensitivity analysis with the FDTD method on structured grids," *IEEE Trans. Microwave Theory Tech.*, vol. 52, no. 4, pp. 1207–1216, Apr. 2004.

M. H. Bakr and N. K. Nikolova, "An adjoint variable method for time domain TLM with fixed structured grids," *IEEE Trans. Microwave Theory Tech.*, vol. 52, no. 2, pp. 554–559, Feb. 2004.

H. Akel and J. P. Webb, "Design sensitivities for scattering-matrix calculation with tetrahedral edge elements," *IEEE Trans. Magn.*, vol. 36, no. 4, pp. 1043–1046, Jul. 2000.

Q. Fang, P. M. Meaney, S. D. Geimer, K. D. Paulsen, and A. V. Streltsov, "Microwave image reconstruction from 3-D fields coupled to 2-D parameter estimation," *IEEE Trans. Med. Imag.*, vol. 23, no.4, pp. 475–484, Apr. 2004.

N. K. Nikolova, Ying Li, Yan Li and M. H. Bakr, "Sensitivity analysis of scattering parameters with electromagnetic time-domain simulators," *IEEE Trans. Microwave Theory Tech.*, vol. 54, no.4, pp. 1589–1610, Apr. 2006.

Y. Song, Ying Li, N. K. Nikolova, and M. H. Bakr, "Self-adjoint sensitivity analysis of lossy dielectric structures with electromagnetic time-domain simulators," *Int. J. of Numerical Modeling: Electronic Networks, Devices and Fields*, vol. 21, no. 1–2, pp. 117–132, Jan.–Apr. 2008.

N. K. Nikolova, J. Zhu, D. Li, M. H. Bakr, and J. W. Bandler, "Sensitivity analysis of network parameters with electromagnetic frequency-domain simulators," *IEEE Trans. Microwave Theory Tech.*, vol. 54, no. 2, pp. 670–681, Feb. 2006.

T. Rubaek, P. M. Meaney, P. Meincke, and K. D. Paulsen, "Nonlinear microwave imaging for breast-cancer screening using Gauss-Newton's method and the CGLS inversion algorithm," *IEEE Trans. Antennas Propagat.*, vol. 55, no.8, pp. 2320–2331, Aug. 2007.

XFDTD v. 6.2, *Reference Manual*, Remcom, 2004, http://www.recom.com/xfdtd6/.

MEFiSTo-3D® Pro v. 4, *User Guide and Operating Manual*, 6th ed., Faustus Scientific, Jan. 2003, http://www.faustcorp.com/products/mefisto3dpro/.

QuickWave-3D v. 6.0, *Reference Manual*, QWED, 2006, http://www.qwed.com.pl/.

E. J. Haug, K. K. Choi, and V. Komkov, *Design Sensitivity Analysis of Structural Systems*. Orlando, FL: Academic, 1986.

J. C. Strikwerda, *Finite Difference Schemes and Partial Differential Equations*. Pacific Grove, CA: Wadsworth & Brooks, 1989.

M. H. Bakr and N. K. Nikolova, "An adjoint variable method for frequency domain TLM problems with conducting boundaries," *IEEE Microwave Wireless Comp. Lett.*, vol. 13, no. 9, pp. 408–410, Sept. 2003.

N. K. Nikolova, Ying Li, Yan Li, and M.H. Bakr, "Self-adjoint Sensitivity Analysis of Linear Electromagnetic Problems in the Time Domain," *The 22nd Int. Review of Progress in Applied Computational Electromagnetics (ACES 2006)*, Mar. 2006, pp. 685–690.

N. Marcuvitz, *Waveguide Handbook.* London, UK: Peter Peregrinus Ltd., 1993 reprint, Chapter 2.

Z. P. Liao, H. L. Wong, Y. Baipo, and Y. Yifan, "A transmitting boundary for transient wave analyses," *Sci. Sinica*, ser. A, vol. XXVII, no. 10, pp. 1063–1076, Oct. 1984.

G. Matthaei, L. Young, and E. M. T. Jones, *Microwave Filters, Impedance-Matching Networks, and Coupling Structures*. Norwood, MA: Artech House, 1980, p. 545.

Y. Song, N. K. Nikolova, and M. H. Bakr, "Efficient time-domain sensitivity analysis using coarse grids," *Applied Computational Electromagnetics Society Journal*, vol. 23, No. 1, pp. 5–15, Mar. 2008.

A. Taflove and S. C. Hagness, *Computational Electromagnetics The Finite-Difference Time-Domain Method.* Artech House, INC, 2000.

Y. Song, N. K. Nikolova, and M. H. Bakr, "Efficient time-domain sensitivity analysis using coarse grids," *Applied Computational Electromagnetics Society Journal*, vol. 23, No. 1, pp. 5–15, Mar. 2008.

Y. Song and N. K. Nikolova, "Central-node approach for accurate self-adjoint sensitivity analysis of dielectric structures," *IEEE MTT-S Int. Microwave Symposium*, June 2007, pp. 895–898.

Y. Song and N. K. Nikolova, "Memory efficient method for wideband self-adjoint sensitivity analysis," *IEEE Trans. Microwave Theory Tech.*, vol. 56, No. 8, pp. 1917–1927, Aug. 2008.

W. C. Chew and J. H. Lin, "A frequency-hopping approach for microwave imaging of large inhomogeneous bodies," *IEEE Microwave Guided Wave Lett.*, vol. 5, pp. 439–441, Dec. 1995.

P. M. Meaney, M. W. Fanning, D. Li, S. P. Poplack, K. D. Paulsen, "A clinical prototype for active microwave imaging of the breast," *IEEE Trans. Microwave Theory Tech.*, vol. 48, pp. 1841–1853, Nov. 2000.

Z. Q. Zhang and Q. H. Liu, "Three-dimensional nonlinear image reconstruction for microwave biomedical imaging," *IEEE Trans. Biomed. Eng.*, vol. 51, pp. 544–548, March 2004.

R. E. Kleinman and P. M. van den Berg, "A modified gradient method for two-dimensional problems in tomography," *J. Comput. Appl. Math.*, vol. 42, pp. 17–35, 1992.

S. Barkeshli and R. G. Lautzenheiser, "An iterative method for inverse scattering problems based on an exact gradient search," *Radio Sci.*, vol. 29, pp. 1119–1130, July–Aug. 1994.

H. Harada, D. J. N. Wall, T. Takenaka, and M. Tanaka, "Conjugate gradient method applied to inverse scattering problems," *IEEE Trans. Antennas Propagat.*, vol. 43, pp. 784–792, Aug. 1995.

T. K. Chan, Y. Kuga, and A. Ishimaru, "Subsurface detection of a buried object using angular correlation function measurement," in *Proc. PIERS'97*, Cambridge, MA, pp. 158, July 1997.